university of groningen / faculty of mathematics and natural sciences / kapteyn astronomical institute

OPTICAL AND NEAR-INFRARED SURFACE PHOTOMETRY OF QUIESCENT DWARF GALAXIES

By

Umut Yıldız

THESIS

Supervisor: Prof. Dr. Reynier F. Peletier

Kapteyn Astronomical Institute
Rijksuniversiteit Groningen
Faculty of Mathematics and Natural Sciences
The Netherlands

April 2008

COLLABORATION

ABSTRACT

OPTICAL AND NEAR-INFRARED SURFACE PHOTOMETRY OF QUIESCENT DWARF GALAXIES

We have presented optical and near-IR surface photometry for quiescent dwarf galaxies (dEs). For this purpose, we have obtained optical images from SDSS (*Sloan Digital Sky Survey*) and near-IR images (H & K bands) from Magpop-ITP *(Multi-wavelength Analysis of Galaxy Populations- International Time Programme)* training network. The Magpop-ITP research has an importance that is the first study of quiescent dwarf galaxies which includes a detailed investigation of field systems. The near-IR sample contains the high resolution images of 33 quiescent and 22 star-forming dwarf galaxies which are in the Virgo Cluster and in the field. However, we mostly focus on quiescent dwarf galaxies. By doing surface photometry we obtain optical and optical - near-IR colours and colour gradients. By analyzing these colours and colour gradients together with comparing the LICK/IDS spectroscopic line strength indices, we have extracted physical information about their metallicity and star formation history.

The major results from this research are;

- Star-forming and quiescent dwarf galaxies can be well seperated in optical vs. UV colour-magnitude diagrams and as well as colour-colour diagrams.
- We do not find any differences between field and cluster dwarf galaxies as a function of environment.
- By making a comparison to stellar populations models we find that the quiescent dwarfs have Sub-Solar or Solar metallicities. Their ages range between 4-10 Gyrs and therefore they are not expected to be primordial.
- Quiescent dwarfs (dEs) have similar colour gradients as giant ellipticals (Es) but less metal rich.

Keywords: galaxies: dwarf quiescent – optical near-infrared surface photometry: galaxies

TABLE OF CONTENTS

LIST OF TABLES

LIST OF FIGURES

ACKNOWLEDGMENTS

First of all I would like to thank to Reynier F. Peletier for inviting me to this project and his extensive help. Also I would like to thank to Isabel Perez-Martin for acting as interim-supervisor.

I wish to thank to Alaxandre Vazruglogobw.epsdekis, Javier Cenarro and Johann Knapen from IAC, Filippo Mannucci from IRA, Mischa Schirmer from ING, Alfonso Aragon-Salamanca from Nottingham, Michael Pohlen from Cardiff, Gert Sikkema from Kapteyn.

And Seyit Hocuk for encouraging me in every possible way, computer man Derek Land, fellow students Aycin Aykutalp, Michela Romanini, Peter Polko, Keimpe Nevenzeel, Tessel van der Laan for the nice days in the old ZG177.

Furthermore thanks to Kapteyn Institute and Instituto de Astrofisica de Canarias for providing me a very nice workplace, MAGPOP ITP collaboration for the data and my family for their moral and financial support.

This research has made use of the NASA's Astrophysics Data System Bibliographic Sercices (ADS) and the NASA/IPAC Extragalactic Database (NED) which is opearated by the Jet Propulsion Laboratory, California Institute of Technology, under contract with the NASA.

CHAPTER 1

Introduction

1.1 Preface

This Master's Thesis of Umut Yildiz is presented to the Kapteyn Astronomical Institute, Rijksuniversiteit Groningen as partial fulfillment of the requirements for obtaining a Master's Degree in Astronomy. The research has been done under the supervision of Prof. Dr. Reynier F. Peletier and made use of data acquired within the Magpop-ITP programme which is under the MAGPOP EU Research and Training Network for the study of dwarf galaxies.

1.2 Introduction

Until recently, not longer than 20 years ago, the research on the formation of galaxies and galaxy clusters has mainly been limited to the most luminous galaxies. Their great size and brightness was the main factor to observe and study them in detail. Along with the new generation of large telescopes and improvement in detectors, their smaller counterparts called "Dwarf Galaxies" have been paid more attention in order to explain the formation and evolution of the galaxies. The key issue in astronomy is still to understand galaxy formation and evolution of the stellar population of the galaxies.

According to current cosmological paradigm, what we presumed know about the Universe is, that it is filled with 72% of Dark Energy ($\Omega_\Lambda \simeq 0.721 \pm 0.015$), 23% of Dark Matter ($\Omega_{\rm DM} \simeq 0.233 \pm 0.013$) and with only 4.6% of Baryonic Matter ($\Omega_{\rm b} \simeq 0.0462 \pm 0.0015$) [Hinshaw et al., 2008]. This 4.6% is believed to be what we see in the Universe, e.g. stars, gas, dust, etc. It is still an important question what the other 96% made of. However, only Dark Matter which is detectable through observations such as its gravitational interaction with luminous matter, helps to explain the rotation curves of spiral galaxies and gravitational lensing.

In the theory of hierarchical structure formation (illustrated in Fig. 1.1, [Lacey and Cole, 1993]), based on ΛCDM - (Cold Dark Matter) model, after the Big Bang the smallest gravitationally bound structures such as quasars and galaxies formed first. They are followed by groups; clusters and superclusters of galaxies. The ΛCDM model is actually a fine tuning of the Big Bang theory which also adds an assumption that most of the matter in the Universe consists of material which cannot be observed by its electromagnetic radiation and therefore it is dark. While at the same time the particles making up this so-called dark matter are slowly

moving and hence they are cold.

Since this theory explains the structure formation in a so-called hierarchical way, it also implies that small galaxies are the basic building blocks for larger galaxies [White and Rees, 1978, White and Frenk, 1991, Navarro et al., 1995]. The theory has been quite successful at large scales such as modeling large scale structures, clusters of galaxies, etc., however for the small scales, there appears a problem by overpredicting the number and mass spectra of the satellites of galaxies. The so-called "missing mass problem" is that ΛCDM predicts large numbers of small dwarf galaxies about $1/1000^{th}$ the mass of the Milky Way, which are never observed [Moore et al., 1999]. Another problem is the inconsistencies of the timescale of the building up of larger galaxies and the differences in the stellar populations of large and small galaxies. Therefore studying dwarf galaxies is very important for the understanding of the evolution of galaxies in the Universe and we can reveal much about galaxy formation and use these results as a test for cosmological models.

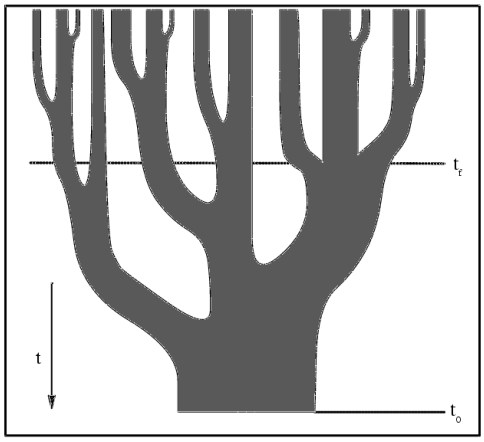

Figure 1.1. This is a schematic representation of a "merger tree" [Lacey and Cole, 1993] depicting the growth of a halo as a result of a series of mergers. Time increases from top to bottom and the widths of the branches of the tree represent the masses of the individual parent halos. The present time t_0 and the formation time t_f are indicated by horizontal lines, where the formation is defined as the time at which a parent halo containing in excess of half of the mass of the final halo was first created.

Besides hierarchical formation theory, another theory for the formation of dwarf galaxies is that they were formed like a by-product at the collision courses between galaxies. These dwarfs made up from some giant ones, therefore they contain high metallicities. These type of galaxies which are not formed by primordial material are called "Tidal Dwarf Galaxies". They are not only different in respect to other dwarfs as the way they formed, they also have different characteristics like their irregular shapes and contain a lot of gas which is a sign of current star formation.

1.3 Dwarf Galaxies in the Universe

There are interesting differences between "Dwarf Galaxies" and "Giant Galaxies". With a mass range of $10^5 - 10^7\ M_\odot$, they are significantly smaller than giants which have a mass range of around $10^9 - 10^{12}\ M_\odot$. Another difference is that most dwarf galaxies have very low metallicities in comparison with the giant

galaxies. This is very important, because it indicates that they are composed of primordial material from the early ages of the Universe. Because, except for the primordial ones created during the Big Bang such as (^{2}D, ^{3}He, ^{4}He, ^{7}Li), all the metals in the Universe are produced by different mechanisms like stellar nucleosynthesis, supernova explosions and stellar winds.

The galaxies which are formed by this way are quiescent dwarf galaxies. Since there is no ongoing star formation activity observed, they are good indicators of primordial material. Dwarf elliptical galaxies, a subtype of quiescent dwarfs are quite common, and are usually companions to other galaxies. Many evidence indicates that most of the dwarf ellipticals do not have properties similar to those of large ellipticals. Instead, they are probably related to irregular galaxies (Fig. 1.2). A detailed study of dwarf galaxies in the Local Group, shows that most of the dwarf ellipticals have a broad star formation history. Many of them appear to have a star formation burst or event in the past few Gyr [Mateo, 1998, Grebel et al., 2003]. Almost all these local group dwarfs also have old populations that date back to nearly the time of reionization.

Figure 1.2. Right: Dwarf Elliptical Galaxy M32 which is a companion to M31; Image Courtesy: 1.1 Meter Hall Telescope, Lowell Observatory, Bill Keel (U. Alabama), Left: Dwarf Irregular Galaxy Leo A; Image Courtesy: Subaru Telescope, NAOJ.

Since some information is given above, it is better to mention about the proper classification of dwarf galaxies. They are divided into two groups; "Quiescent Dwarfs" and "Star Forming Dwarfs" [Grebel et al., 2001].

Quiescent Dwarfs are subdivided into;

- Dwarf Elliptical Galaxies (dE)
- Dwarf Spheroidal Galaxies (dSph)

Star forming Dwarfs are subdivided into;

- Dwarf Irregular Galaxies (dIrr)
- Dwarf Spiral Galaxies (dS)
- Gas rich Irregular Galaxies
- Blue Compact Dwarf (BCD) or HII Galaxies

The classification of dwarf galaxies is given by Sandage and Binggeli [1984] in Fig. 1.3. They classified 138 galaxies in the Virgo Cluster by their morphological type. They selected Virgo Cluster because it is so big and rich that it contains every known morphological type of galaxies. In addition to the giants the position of the dwarfs is also shown. In the figure, on the right side, the late-type giant sequence was extended towards fainter luminosities with Sd, Sm and Im classes. In this region Sm and Im are also catagorized as "Dwarf Irregulars" (dIrrs). Since this region is the place of star formation, at the very right "Blue Compact Dwarfs" (BCD) are placed with their quite strong star formation activity. According to [Marlowe et al., 1999], the surface brightnesses of the stellar envelopes of these galaxies show that they would be similar to today's dE's once their star formation has ended. If we move through the left part of the diagram, there supposed to be "Dwarf Spirals" (dSa) for the faint luminosities, however there are no dSa found so far. To form and sustain spiral arms, a galaxy should be more massive than $\sim 5 \times 10^9 M_\odot$. Only then the circular velocity is high enough so that regular arms can form [Michielsen, 2005].

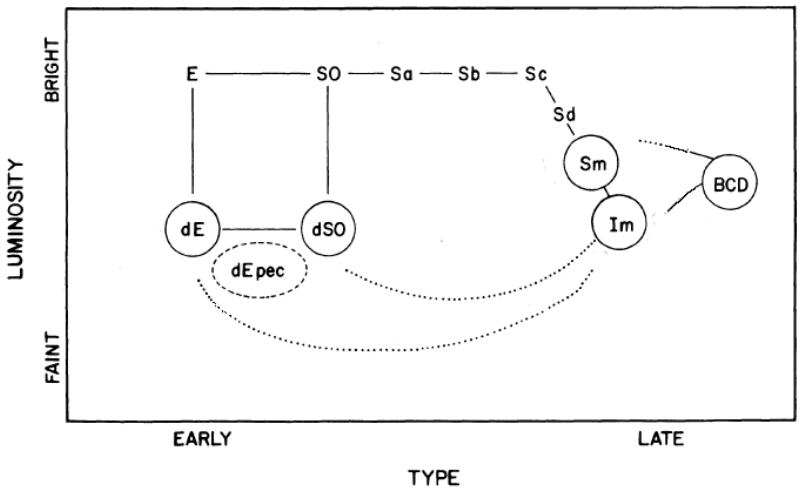

Figure 1.3. The classification of dwarf galaxies [Sandage and Binggeli, 1984]

The main interest of this thesis is placed on the left part of the diagram. According to the definition published by Sandage and Binggeli [1984], the B band absolute magnitudes fainter than $M_B < -18$ are known to be the most abundant and the most common type of galaxies in the Universe with their very low masses. They are called "Dwarf Elliptical Galaxies" (dEs). Their surface brightness profiles have nearly flat profiles and follows an exponential law while their giant counterparts follows a $r^{1/4}$ or de Vaucouleurs law. Brighter than $M_B = -18$, it become clear that the surface brightness profiles of early-type galaxies can be fitted by a Sersic $r^{1/n}$ law, with n varying continuously from $n \geqslant 4$ for normal Es to $n \leqslant 1$ for dEs. A further distinction between bright and faint dEs is usually made at $M_B = -16$.

The other subtype of quiescent dwarfs is called "Dwarf Spheroidal Galaxies" (dSphs). It is now thought that these are basically the same type as dEs but are just viewed from a different angle. Their magnitude range is $(-10 \geqslant M_B \geqslant -16)$, and they are mainly observed in the Local Group.

In this research we conducted near-IR observations. Because near-IR radiation

(Fig. 1.4) is very close to optical side of the electromagnetic spectrum so that it behaves similarly to visible light and can be detected using similar electronic devices. It is characterized by water absorption and defined by 0.7-1 to 5 μm range. This range is not precise, we encountered that depending on publication it may vary to different scales. Since we go through the longer wavelengths in the infrared we can make observations of different temperature ranges and hence different environments in space. Interstellar dust is the most transparent in the near-IR region so it is very important characteristic benefited most for such research. Also many of the hotter stars in optical range get faded in the near-IR images. Therefore by having near-IR photometry it makes it possible to measure the amount of old stellar populations, unaffected by the blue light of young stars.

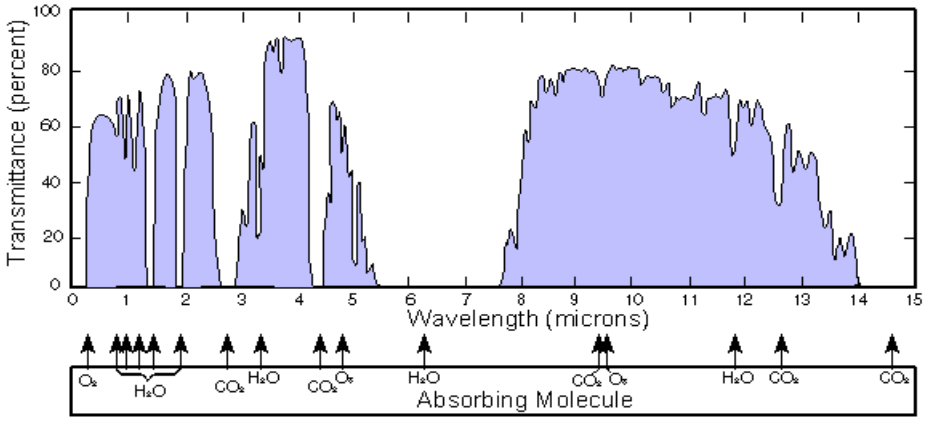

Figure 1.4. Plot of atmospheric transmittance in part of the infrared region.

1.4 MAGPOP & Magpop-ITP

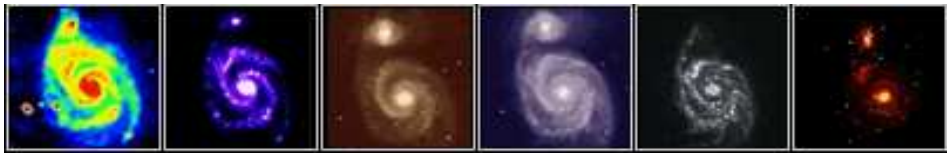

MAGPOP "Multi-wavelength Analysis of Galaxy Populations" project is a Marie Curie Research Training Network funded under the Sixth Framework Programme of the EU. The project is led by Guinevere Kauffmann (MPIA - Garching) with 8 nodes and 2 associated nodes in Europe and the USA. Its objectives are to extract key physical information - stellar masses, star formation rates, star formation histories, metallicities and dust content from the spectral energy distributions (SEDs) of galaxies in the local Universe and at high redshifts.

The Magpop-ITP (International Time Programme) is a large observational project of the MAGPOP EU Research and Training Network to investigate the star formation history of Dwarf Galaxies. It is led by Reynier F. Peletier (Rijksuniversiteit Groningen), and Javier Gorgas (Universidad Complutense de Madrid) & Alessandro Boselli (Laboratoire d'Astrophysique de Marseille). In the framework of this International Time Programme, a total of 60 nights were

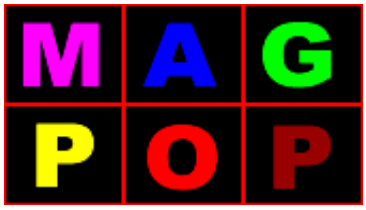

Figure 1.5. MAGPOP Network Logo

allocated on the 4 large telescopes (WHT, INT, TNG and NOT) at the Roque de los Muchachos Observatory in La Palma, Spain. The programme comprises optical & near-IR imaging and spectroscopy of quiescent and star-forming dwarf galaxies in the field and in the Virgo Cluster. All galaxies in the sample have images in GALEX and SDSS (Sloan Digital Sky Survey) in the UV and optical, and have many additional data available in the GOLDMine database.

The aim of the programme is to get multi-wavelength data for a sample of Virgo Cluster and field dwarfs to study the star formation histories, chemical evolution as a function of their environment and dwarf type. For "Star-forming Dwarfs", the aim is to understand the triggering of star formation properties and evolution of gas and dust. For "Quiescent Dwarfs", the aim is to understand structural properties, scaling relations, internal kinematics and presence of interstellar medium.

Other questions posed are; what is the relation between star forming and quiescent dwarfs; what are the evolutionary stages of field and cluster dwarf galaxies; since they are the most abundant galaxy type what are the role of dwarf galaxies in the galaxy evolution?

1.5 Research Goal

The goal of my research is to study the optical - near-IR properties of quiescent dwarf galaxies. For this purpose, together with SDSS (Sloan Digital Sky Survey) optical images, I used near-IR images which were acquired by the Magpop-ITP collaboration. The dwarf sample were observed in the near-IR bands (H & K) at the William Herschel Telescope (WHT), Telescopio Nazionale Galileo (TNG) and Nordic Optical Telescope (NOT) in 2006 and 2007.

The near-IR data are divided in two types, star-forming and quiescent dwarf galaxies. My research consists of; firstly reducing all these high resolution near-IR data, then determining the magnitudes of these dwarf galaxies using aperture photometry techniques. However, the main focus is on quiescent dwarfs, so also using SDSS's u, g, r, i, & z band images, determining the surface photometry profiles and obtain optical and near-IR colours and colour gradients. Though, analyzing these colours and colour gradients together with comparing the spectroscopic indices we extract physical information about their metallicity and star formation history. We also investigate the differences between objects by their location, if there is any difference in cluster environment or in field.

The thesis is organised as follows: The current chapter (Chapter 1) gives a general introduction to the Universe of Dwarf Galaxies. Chapter 2 mentions the sample and its selection done by Magpop-ITP collaborators. Chapter 3 describes the observations and data reduction technique in detail. Chapter 4 gives the main target

of this thesis, photometry. It describes how the calibration was done, magnitudes are determined, and how the surface photometry is done through ellipse fitting with GALPHOT program. Chapter 5 gives some information about Stellar Populations and the techniques to study them. With Chapter 6, we present the results from surface photometry and start the analysis by colour and line strengths relations. Chapter 7 is the analysis of colour gradients and Chapter 8 is the conclusion of this thesis.

CHAPTER 2

Sample

2.1 Sample Selection

The sample selection for the MAGPOP-ITP programme will be presented in Peletier et al. [2008] (in preparation) in detail. Briefly, the dwarfs consist of magnitude-limited sample in the Virgo Cluster and also some field sample of random directions in the sky. One of the criteria was to have complementary observations to be available in UV and visual through GALEX and SDSS catalogues. UV data of GALEX has also an additional importance because the UV is a very sensitive indicator of recent star formation. The sample was selected in 3 different environments which are;

- in a relatively high density environment (in our case Virgo Cluster)
- for quiescent dwarfs in groups
- in the field

Virgo Cluster which has more than 50% of the galaxies are dwarf ellipticals [Sandage et al., 1985] is a good region to study cluster environment. In this region, dwarf galaxies are selected from the VCC (Virgo Cluster Catalogue) catalogue of Binggeli et al. [1985]. The initial selection criteria for star-forming dwarfs was $m_{\rm B} < 15.5$ and for quiescent dwarfs was $m_{\rm B} > 15$. Then the priority was given to the galaxies which have GALEX data available and have information from previous spectroscopic observations.

For the field sample SDSS is queried for nearby dwarf galaxies with the selection criteria of $0.00125 < z < 0.00625$ and -18.5 $< M_{r'} <$ -15 mag.[1] In order to select quiescent dwarfs a colour-cut is applied by UV colours of GALEX, FUV-NUV > 0.9 for the quiescent dwarfs and FUV-NUV < 0.9 for the star-forming dwarfs, or in optical colours of SDSS, $u - g > 1.2$. These colour-cuts increase the separeation of starforming and quiescent galaxies in Virgo Cluster [Peletier et al., 2008], [Michielsen et al., 2008]. The full list of the sample given in Tables 2.2 and 2.3.

Finally, 22 field and 33 Virgo Cluster dwarfs were observed by near-IR imaging cameras. From these 55 dwarfs 22 of them are star-forming and 33 of them are quiescent.

[1]The absolute magnitudes were computed using SDSS radial velocities and assuming the Hubble constant H_0=70km s^{-1} Mpc^{-1}.

2.1.1 SDSS

SDSS [2], "the Sloan Digital Sky Survey", is the largest optical sky survey ever conducted. Since surveying is still in operation, when completed, it will provide detailed optical images covering more than a quarter of the sky, and a 3D map of $\sim 10^6$ galaxies and quasars [Stoughton et al., 2002]. The survey uses a 2.5 metre telescope on Apache Point, New Mexico with two instruments to perform photometry and spectroscopy. Its 120-megapixel camera has a the field-of-view of 1.5 deg^2 and the spectrographs can measure spectra of over 600 galaxies and quasars in a single observation.

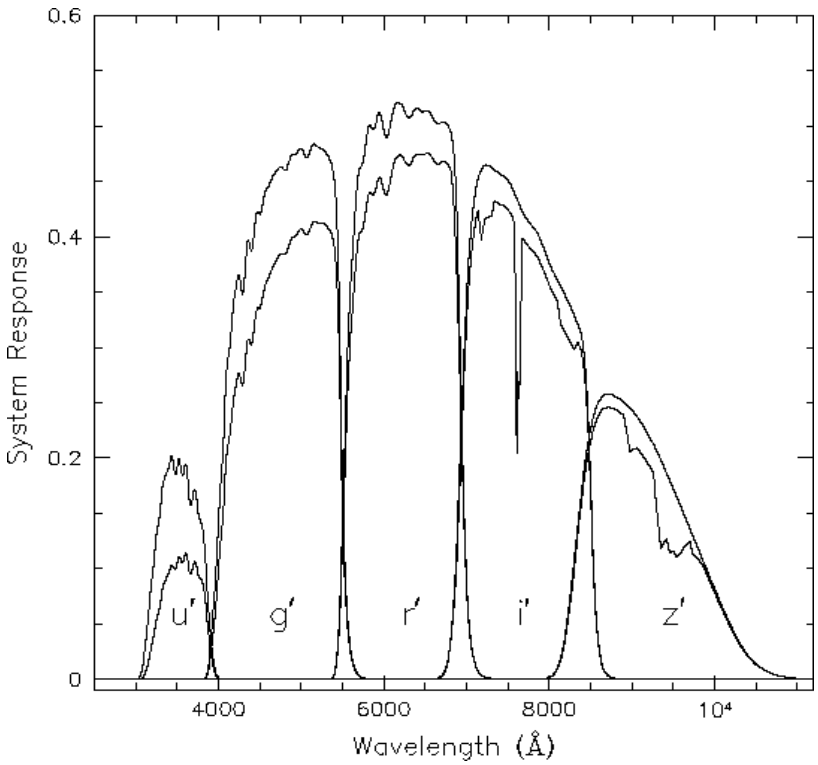

Figure 2.1. The SDSS system response curves for photometric system. The responses are shown without atmospheric extinction (upper curves) and as modified by the extinction at 1.2 airmasses (lower curves). The curves represent expected total quantum efficiencies of the camera plus telescope on the sky [Fukugita et al., 1996]

SDSS photometry is performed on five band u', g', r', i' and z', the response function of all the bands can be seen in Fig 2.1 [Fukugita et al., 1996, Gunn et al., 1998] (Also see Table 2.1 for the exact wavelengths). It should briefly be mentioned that SDSS observing software pipeline produces several types of magnitudes for the galaxies;

- "The Fiber Magnitude", a magnitude taken from the flux from a 3" spectroscopic fiber

[2]Funding for the SDSS has been provided by the Alfred P. Sloan Foundation, the Participating Institutions, the National Science Foundation, the US Department of Energy, NASA, the Japanese Monbukagakusho, the Max Planck Society, and the Higher Education Funding Council for England. The SDSS website is http://www.sdss.org/. SDSS is managed by the Astrophysical Consortium for the participating institutions.

Filter	Wavelength $\AA$
Ultraviolet (u)	3543
Green (g)	4770
Red (r)	6231
Near Infrared (i)	7625
Infrared (z)	9134

Table 2.1. SDSS Filters' wavelength limits

- "The Petrosian Magnitude", which measures the galaxy fluxes within a circular aperture whose radius is defined by the shape of the azimuthally averaged light profile
- and magnitudes matched to a galaxy model, like de Voucouleurs profile or exponential profile.

SDSS imaging is obtained using a drift scanning mosaic CCD camera with a pixel size of 24μm (0.396" on the sky). The effective integration time per filter is 53.907456 seconds, and the time for passage over the entire photometric array is about 5.7 minutes. Its technical details are explained by York et al. [2000]. We obtained the "corrected frames" of all the five bands' images from the SDSS DR6 Data Archive Server. The u', i' and z' bands' images are less sensitive and less useful to study the profiles near the center of the galaxies, however, we tried to make use of all the bands as good as possible.

The SDSS corrected frames are bias subtracted, flat-fielded and purged of bright stars and stored at SDSS in integer format to save disk space. The SDSS webserver indicates that the pixel values get randomized appropriately before being rounded to make sure that the statistics of the background counts are reasonable. An additional offset which is called "Softbias" of 1000 counts is added to each pixel to avoid negative pixel values and this should be subtracted together with the sky value which will be described in the following chapter.

Galaxy	Other Name	RA	Dec	Type	Type	V(km/s)	z	Distance Goldmine*
CGCG119069	-	125,359875	21,130611	dQ	E-E/S0		0,016000	65,573770
ID0028	-	40,793995	-0,262867	dQ	dE		0,003219	13,192623
ID0118	UGC08127	195,265289	-1,953390	dSF		1466	0,004890	20,040984
ID0149		219,913818	2,581790	dSF		1649	0,005500	22,540984
ID0154		220,452927	3,089783	dSF			0,005309	21,758197
ID0158	UGC05776	159,506729	64,266357	dQ	sph-comp		0,005662	23,204918
ID0207	-	228,789322	2,751789	dQ	dE		0,005242	21,483607
ID0365	CGCG265055	150,309692	55,718262	dSF	dIrr	1286	0,004360	17,868852
ID0615	NGC3073	150,216995	55,618820	dQ	dE		0,003810	15,614754
ID0650	UGC08986	211,066010	4,112194	dQ	dE		0,004164	17,065574
ID0734	-	40,396095	-8,173479	dQ	dE		0,005130	21,024590
ID0872	-	40,501507	0,014547	dQ	dE		0,003743	15,340164
ID0918	PGC53521	224,702988	2,023521	dQ	dE		0,006045	24,774590
ID0943	-	156,988464	60,634125	dQ	dE		0,004328	17,737705
ID0957	PGC32664	163,202652	0,034450	dSF	dIrr		0,006113	25,053279
ID1029	-	220,871658	4,531631	dSF	dIrr		0,005843	23,946721
ID1109	-	217,331574	2,710549	dQ	dE		0,005981	24,512295
ID1186	-	215,181442	4,143630	dQ	dE		0,006052	24,803279
ID1225	UGC09432	219,766480	2,947061	dSF	dIrr		0,005177	21,217213
ID1330	NGC5727A	220,014496	34,099888	dSF	dIrr		0,004978	20,401639
ID1524	NGC5826	226,640991	55,479111	dQ	dE		0,002746	11,254098
ID12131		220,390488	3,496675	dSF		1675	0,005587	22,897541

Table 2.2. Field Sample observed by Magpop-ITP

Galaxy	Other Name	RA	Dec	Type	Type	V(km/s)	z	Distance Goldmine*
VCC0024	IC 3028	182,648607	11,760707	dSF	BCD	1292	0,004296	32,000000
VCC0165	-	183,971965	13,215793	dQ	S0	255	0,000851	17,000000
VCC0200	-	184,140458	13,031583	dQ	dE	65	0,000055	17,000000
VCC0397	-	185,050698	6,623073	dQ	dE	2411	0,008242	23,000000
VCC0407	IC 3167	185,078250	9,545361	dQ	dE/dS0	2078	0,006751	17,000000
VCC0482	UGC 07411	185,392032	4,779470	dQ	S0a-S0/Sa	1802	0,007195	17,000000
VCC0509	UGC 7423	185,481500	6,450611	dSF	Sdm-Sd/Sm	1258	0,004190	23,000000
VCC0523	NGC 4306	185,517125	12,787472	dQ	dS0	1508	0,006608	17,000000
VCC0568	CGCG42057	185,665474	6,226135	dSF	dS	2823	0,009417	23,000000
VCC0693	-	186,013463	5,180757	dSF	Sm	2048	0,006831	17,000000
VCC0739		186,166792	3,302833	dSF	Sd	926	0,003090	17,000000
VCC0741		186,172125	3,721500	dSF	BCD	1861	0,006208	17,000000
VCC0794	UGC 07504	186,340000	16,429444	dQ	dS0	918	0,003062	17,000000
VCC0816		186,399910	15,847800	dQ	dE		0,004000	17,000000
VCC0817	IC 3313	186,401833	15,829833	dQ	dE	1168	0,003579	17,000000
VCC0940	IC 3349	186,696125	12,453972	dQ	dE	1563	0,004707	17,000000
VCC0980	IC 3365	186,796583	15,896667	dSF	Scd	2342	0,007839	17,000000
VCC0990	IC 3369	186,820583	16,024472	dQ	dE	1727	0,005761	17,000000
VCC1087	IC 3381	187,062000	11,789833	dQ	dE	645	0,002252	17,000000
VCC1107	-	187,127000	7,324750	dQ	dE	1500	0,005071	17,000000
VCC1183	IC 3413	187,343708	11,433833	dQ	dS0	1387	0,004453	17,000000
VCC1261	NGC 4482	187,543042	10,779472	dQ	dE	1850	0,006241	17,000000
VCC1266	UGC 7642	187,557307	2,624708	dSF	Sdm-Sd/Sm	1637	0,005451	17,000000
VCC1431	IC 3470	188,097397	11,262829	dQ	dE	2025	0,005019	17,000000
VCC1435	UGC 07688	188,134965	8,045261	dSF	Im	609	0,002031	17,000000
VCC1486	IC 3483	188,291917	11,347389	dSF	S (dS)	129	0,000430	17,000000
VCC1567	IC 3518	188,630375	9,623444	dQ	dE/dS0	1440	0,004803	17,000000
VCC1778	IC3611	189,767236	13,363524	dSF		2750	0,009123	17,000000
VCC1861	IC 3652	190,244000	11,184500	dQ	dE	683	0,002099	17,000000
VCC1871	IC 3653	190,315516	11,387090	dQ	E-E/S0	603	0,001891	17,000000
VCC1910	IC 0809	190,536083	11,754389	dQ	dE	206	0,001000	17,000000
VCC1912	IC 0810	190,537917	12,596833	dQ	dS0	-169	-0,000564	17,000000
VCC1947	-	190.734671	3,676462	dQ	dE	1083	0,003249	17,000000

Table 2.3. Virgo Group Sample observed by Magpop-ITP, * Cluster distance is taken for Virgo Cluster dwarfs

CHAPTER 3

Observations and Data Reduction

3.1 Telescopes and Instruments

The data was collected at the Roque de los Muchachos Observatory from 3.58 m Telescopio Nazionale Galileo (TNG) using NICS instrument, 4.2 m William Herschel Telescope (WHT) using Liris instrument and Nordic Optical Telescope (NOT) using NOTCam instrument at 13 different nights (Table 3.1) by Magpop-ITP colloborators. A brief summary of instruments used is given below.

NICS instrument, "the Near Infrared Camera and Spectrometer" which is expressly designed & built and permanently mounted on 3.6 m TNG telescope. This instrument is a FOSC-type cryogenic focal reducer equipped with two interchangeable cameras feeding a Rockwell Hawaii 1024×1024 array. It has a $4.2' \times 4.2'$ field of view and 0.25"/pixel resolution [Baffa et al., 2001, Oliva, 2003].

Liris instrument, "Long-slit Intermediate Resolution Infrared Spectrograph" is a near-IR imager/spectrograph for use at the Cassegrain focus of the 4.2 m WHT telescope. It was built and developed at IAC. Liris uses a 1024×1024 HAWAII detector for the 0.8 to 2.5 μm range. The pixel scale is 0.25"/pixel, yielding a field of view of $4.27' \times 4.27'$ [Manchado et al., 1998].

NOTCam instrument, the near-IR Camera/spectrograph is a Rockwell Hawaii grade array with $1024 \times 1024 \times 18\mu$m pixels in HgCdTe. We used its wide field imaging detector with a field of view of $4.0' \times 4.0'$ and a pixel size of 0.23"/pixel [Abbott et al., 2000].

Figure 3.1. 3.6 m TNG, 4.2 WHT & 2.5 m NOT telescopes in La Palma, The Observatorio del Roque de los Muchachos

Observers Log

Night	Telescope	Observers
20-21 Mar 2006	NICS@TNG	C. Carretero - J. Gorgas
02-03-04 Mar 2007	NICS@TNG	G. Sikkema - M. Balcells - A. Boselli
07 Mar 2007	LIRIS@WHT	R. Peletier
29-31 Mar 2007	Notcam@NOT	D. Michielsen - M. Pietka
06-07 May 2007	LIRIS@WHT	I. Perez-Martin - A. Boselli
09-10 Aug 2006	LIRIS@WHT	R. Peletier

Table 3.1. There were 6 runs of observations. Here, the observers of the Near-IR imaging at the Magpop-ITP team

3.1.1 Conducting Near-Infrared Observations

We used H (1.65μm) and K_s (2.16μm) filters in our observations. Comparing with the visual observations, conducting infrared observations are difficult as a result of the airglow in H and K. Additionally, the IR background in H is dominated by emission from vibrational transition of the OH radical, which originates at $\sim$ 90 km above Earth's surface. The telescope and its surroundings emit radiation strongly (T $\sim$ 300K) in the near-IR region therefore e.g. in NICS all the optical components reside in a vacuum at a temperature of $\sim$ 80 K, inside a suitable cryostat. This airglow varies rapidly both in space and time due to the changing conditions like air movements in the atmosphere or the movements of the telescope. Near-IR observations therefore requires an accurate subtraction of this constantly changing background.

The observations are conducted with the telescopes' wide-field camera (0.25"/pixel) and they have the advantage of dithering (all the images are on source) between four lenses (quadrants). Dithering technique is applied over 4, 8 or 9 positions on the square grid of the CCD in order to construct the sky frames. (See Fig. 3.2 for four lenses, and Fig. 3.6 for dithering observation of 4 positions). Since the instruments have $4.2' \times 4.2'$ field of view and most of the dwarf galaxies in the sample have no more than $\sim$ 30" in size, every frame of observation have sufficient space in order to extract sky information.

Since there were many observers conducting these observations, number of dithering exposures and exposure timing varies from 10 seconds to 30 seconds over some nights. Most images were acquired by several short exposures at each position in order to prevent saturation. Total integration times vary, from 10 minutes up to over an hour depending on how faint the dwarfs are. Table 3.2 presents the observing log with exposure times. Out of 13 nights of observation, 6 nights were not photometric. We calibrated all the images with differential photometry techniques and compared with the Goldmine values.

Galaxy	Inst.	Date Obs.	Phot	Exp H	Exp K
CGCG119069	NICS	04 Mar 07	No	640	1980
ID0028	Liris	10 Aug 06	No	1200	2440
ID0118	Notcam	31 Mar 07	Yes	3420	-
ID0149	Notcam	31 Mar 07	Yes	5070	-
ID0154	Notcam	29 Mar 07	No	3600	-
ID0158	NICS	03 Mar 07	Yes	640	-
ID0207	NICS	02 Mar 07	Yes	1980	-
ID0365	NICS	02 Mar 07	Yes	900	-
ID0615	NICS	02 Mar 07	Yes	620	-
ID0650	NICS	02 Mar 07	Yes	640	-
ID0734	Liris	09 Aug 06	No	1200	1040
ID0872	Liris	09 Aug 06	No	960	800
ID0918	NICS	02 Mar 07	Yes	860	-
ID0943	NICS	03 Mar 07	Yes	1280	-
ID0957	NICS	04 Mar 07	No	720	-
ID1029	Liris	07 May 07	Yes	1800	1920
ID1109	Liris	07 Mar 07	No	1800	360
ID1186	NICS	02 Mar 07	Yes	1320	-
ID1225	Liris	06 May 07	Yes	1800	-
ID1330	Liris	06 May 07	Yes	1800	1920
ID1524	NICS	02 Mar 07	Yes	1280	-
ID12131	Notcam	31 Mar 07	Yes	3600	
VCC0024	NICS	20 Mar 06	No	1240	-
VCC0165	NICS	21 Mar 06	No	440	440
VCC0200	Liris	06 May 07	Yes	1800	1920
VCC0397	NICS	03 Mar 07	Yes	1340	-
VCC0407	Liris	06 May 07	Yes	1800	1920
VCC0482	NICS	20 Mar 06	No	440	473
VCC0509	Notcam	29 Mar 07	No	3240	-
VCC0523	NICS	04 Mar 07	No	-	680
VCC0568	Notcam	30 Mar 07	Yes	3570	-
VCC0693	Liris	06 May 07	Yes	1800	1920
VCC0739	Notcam	30 Mar 07	Yes	3600	-
VCC0741	Notcam	29 Mar 07	No	2880	-
VCC0794	NICS	21 Mar 06	No	495	451
VCC0816	Liris	07 May 07	Yes	1920	1920
VCC0817	Liris	07 May 07	Yes	1920	1920
VCC0940	NICS	20 Mar 06	No	506	440
VCC0980	NICS	20 Mar 06	No	495	462
VCC0990	NICS	03 Mar 07	Yes	1320	-
VCC1087	NICS	04 Mar 07	No	-	420
VCC1107	NICS	21 Mar 06	No	506	451
VCC1183	NICS	04 Mar 07	No	-	680
VCC1261	NICS	04 Mar 07	No	660	640
VCC1266	Liris	07 May 07	Yes	1800	1920
VCC1431	NICS	04 Mar 07	No	-	680
VCC1435	NICS	21 Mar 06	No	440	451
VCC1486	Liris	07 May 07	Yes	1800	-
VCC1567	Liris	07 May 07	Yes	1800	1920
VCC1778	Notcam	30 Mar 07	Yes	3600	-
VCC1861	NICS	03 Mar 07	Yes	720	680
VCC1871	NICS	21 Mar 06	No	451	308
VCC1910	NICS	20 Mar 06	No	506	440
VCC1912	NICS	03 Mar 07	Yes	1300	700
VCC1947	NICS	04 Mar 07	No	-	660

Table 3.2. Journal of the Observations of Field and Virgo Group Samples; Phot: if the night is photometric or not, Exp: Exposure times are given in seconds

3.2 Data Reduction by SNAP

All of the images are reduced by SNAP *Speedy Near-Infrared data Automatic Pipeline* software which is written by Mannucci [2002] explicitly for the TNG telescope's NICS instrument. Since many important characteristics of the *NICS*, *Liris* and *NotCam* instruments are similar, we modified SNAP with certain scripts in order to succesfully reduce *Liris* and *NotCam* data. It makes use of several existing softwares like IRDR, IRAF, SExtractor and Drizzle to allow for a full reduction of near-IR data.

SNAP

Speedy Near-IR data Automatic reduction Pipeline

3.2.1 Step-by-step Reduction Procedures

Obtaining Raw Frame

Near-IR raw images suffer strong infrared background. As it can be seen in Fig. 3.2, we cannot infer meaningful estimate in the frame without applying certain reduction processes.

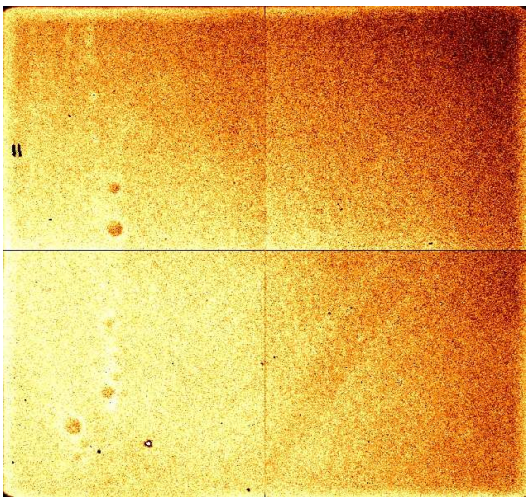

Figure 3.2. Raw NIR image obtained by LIRIS at WHT telescope. (VCC0200 K-band)

Correction for the Cross-Talk

NICS images requires particular treatment, because it suffers severe cross-talking effect (i.e. a signal which was detected in one quadrant produced ghost images in the other three quadrants) among the signal in various quadrants and for the distortion of the NICS optics. If the image contains especially saturated bright objects (stars etc.), the final image leave positive ghosts in the other three quadrants. Under normal circumstances, the unsaturated objects even if they are very bright also cause this effect, however, it is easily recognised because they appear on all

quadrants at the same position. This effect can be corrected by software at the beginning of the process. From all our galaxies, only one galaxy's image (ID1524) could not be corrected because of the very bright nearby star and remained to have this error after reduction which can be seen in Fig. 3.3.

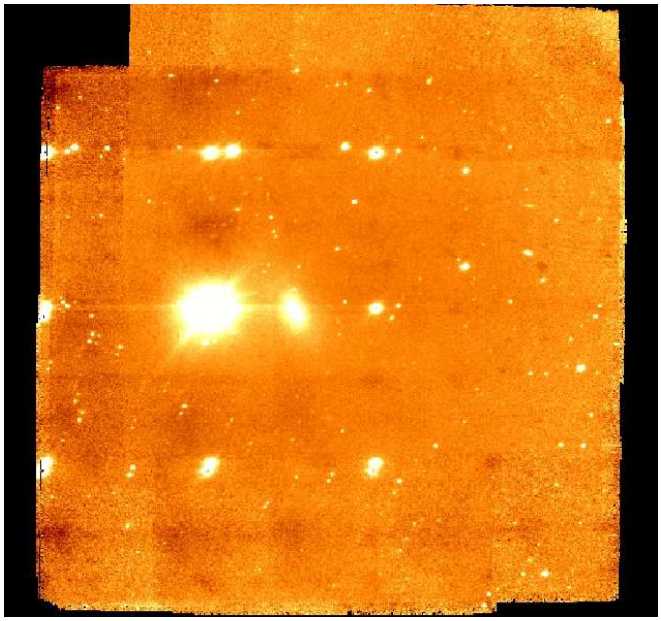

Figure 3.3. Cross-talk example that NICS suffers

Creating Masterflat

Instead of having a flat frame observation, all the science images are combined by IRAF task `imcombine`. The input images are scaled to have the same `median` and the pixels containing objects are rejected by `sigclip` based on the measured noise. Fig. 3.4, masterflat shows to have similar features as the raw image.

Computing Bad Pixel Mask

After creating the masterflat, it is searched for bad pixels with deviant values. They are searched by two methods; they either have values of `nsig`$\pm 5\sigma$ from the surrounding box of 16 $\times$16 pixels, or they have the value below `mingain`=0.7 or above `maxgain`=1.4 times the average gain. The flat field is then normalized in order to obtain the "gain map" and here bad pixels are set to 0.

First Pass Sky Subtraction

Since the atmosphere varies quite rapidly in the near-IR, in order to do the sky subtraction to an image, only a few closest frames (in time) have to be selected before and after this image. Fig. 3.5 shows that in order to get a sky subtracted image of "image 0", the subsequent images from left and right is selected and they are combined by a `median` to obtain a first approximation of the sky. Depending on the weather conditions, to get high signal-to-noise ratio, we mostly used 7 previous + 7 next = 14 frames to determine the sky. In severe observing conditions of the sky we used only 3 previous + 3 next = 6 frames. This technique is called "running-sky technique".

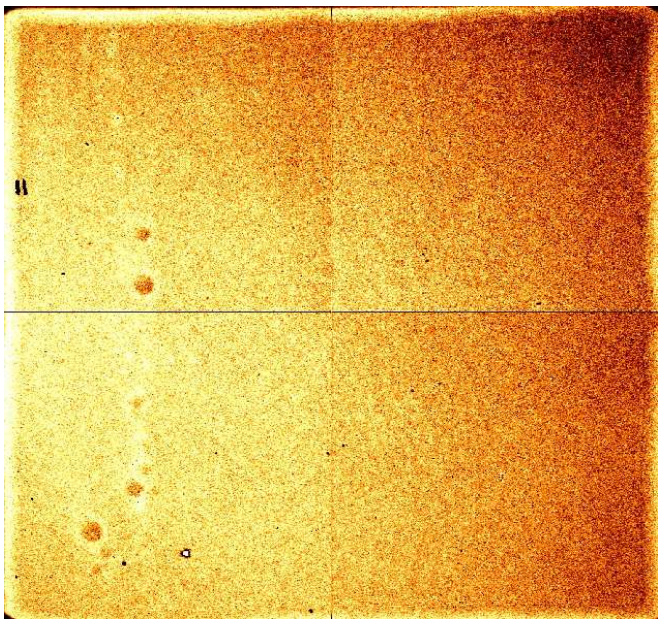

Figure 3.4. Masterflat obtained by combining all the images.

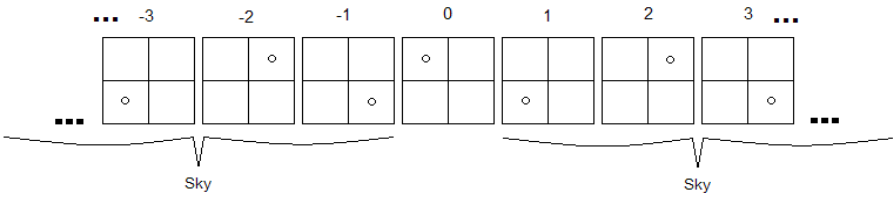

Figure 3.5. Number of images combined and subtracted from each frame

Then this sky frame is subtracted from the image and the result is divided by masterflat to correct for low spatial frequency distortion of the flat field or the sky image. Fig. 3.6 shows the sky-subtracted and flat-divided frames.

Detecting Objects

"SExtractor" [Bertin and Arnouts, 1996], probably the most popular software in its field is used to detect the objects in these cleaned frames. An object mask is created containing 0 in the pixels attributed to the sky and object minus background in the pixels attributed to the objects. This resulting mask is only used to compute the offsets between the images and since this procedure is going to used again, in general there is no need to detect faint objects. Fig. 3.7 shows the object mask for one frame.

Computing Offsets

This is most critical step which depends on the performances of the telescope. Offsets are computed to sub-pixel accuracy by fitting a parabola to the peak of the cross-correlation image.

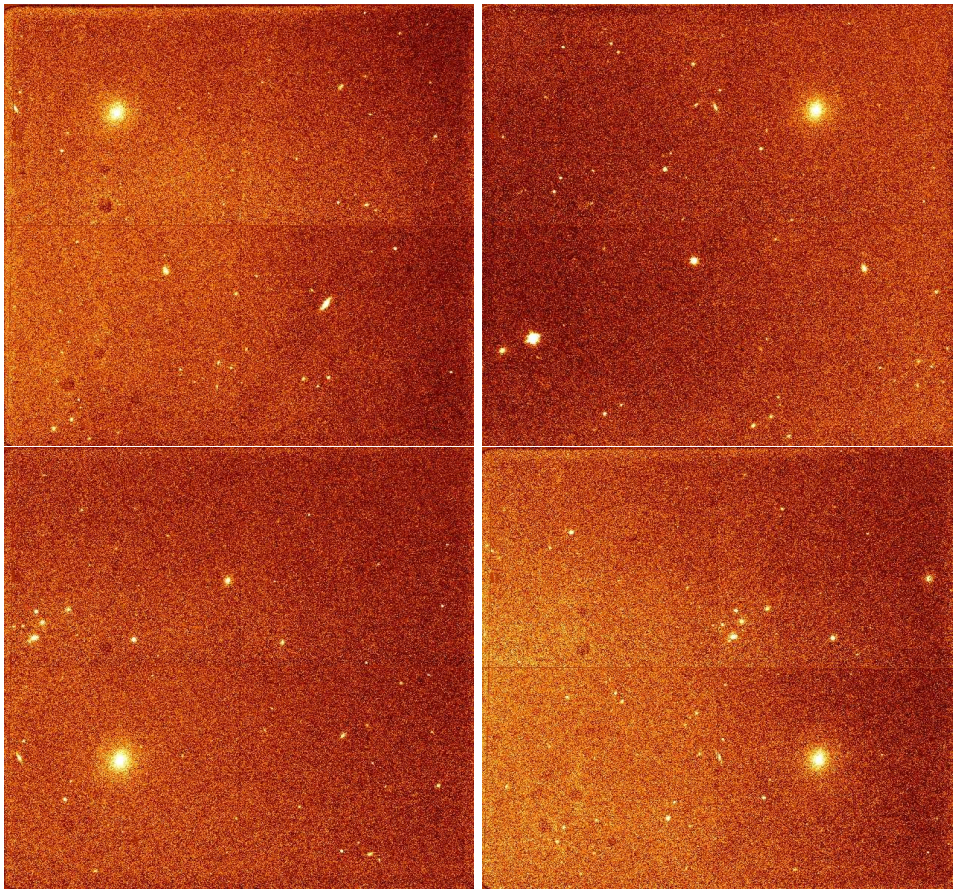

Figure 3.6. Sky subtracted & flat-divided frames

First Pass Coaddition

Once the offsets are computed, the sky-subtracted and flat-fielded images are combined into the first-step resulting image. This image is far from perfect since an object masking has not yet used and two other problems remained to be solved. Firstly, the presence of faint objects in the sky frames are not removed by the combination, and the presence of field distortion is not corrected.

Master Object List Mask

SExtractor is used again to find objects in previously created first-pass coadded image in order to mask during sky computation. This time the parameters controlling the detection threshold set to have deeper detections and mask faint objects. See Fig. 3.7.

Second Pass Sky Subtraction

As in the first pass sky subtraction, the running-sky technique is used again but this time by taking into account master object mask computed at the previous step. This technique is very efficient to remove the influence of the objects in the determination of the sky background influencing the image quality.

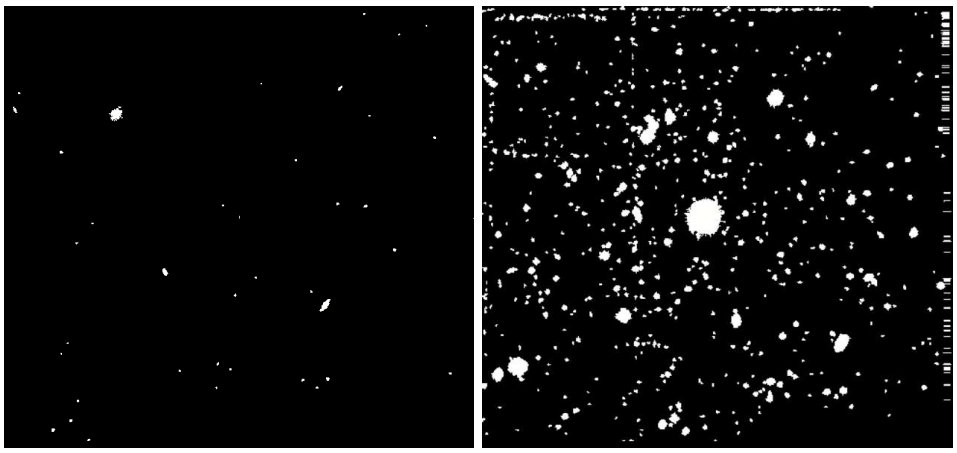

Figure 3.7. Left: Object mask for one image, Right: Master Object Mask,

Final Offsets Computation

Before running for offset computation, especially NICS's large field optics has large pin-cushion field distortion around 1% near the edges of the array and 3% near the corners. It severely degrade the image quality in the outer part of the image or introduce large distortion in large mosaics of images. Its correction is done by an external procedure called "Drizzle". After correcting the field distortions final values of the offsets computed again.

Final Coaddition

The resulting images are offseted to a common value, masked by using the gain map and combined by using final offsets. An external procedure from IRDR (Infrared Data Reduction) used for the combination producing an unclipped average of the input pixels weighted for their gain and for the fractional overlapping area. Also a weighting image is created (Fig. 3.8) which contains the image weight. Finally, a combination with IRAF task `imcombine` is used in order to obtain the final image (Fig. 3.9). When using these procedures, the noise in the final image is just a few percents. E.g. in a mosaic of 30 images, the measured noise is only about 2% above the theoretical limit.

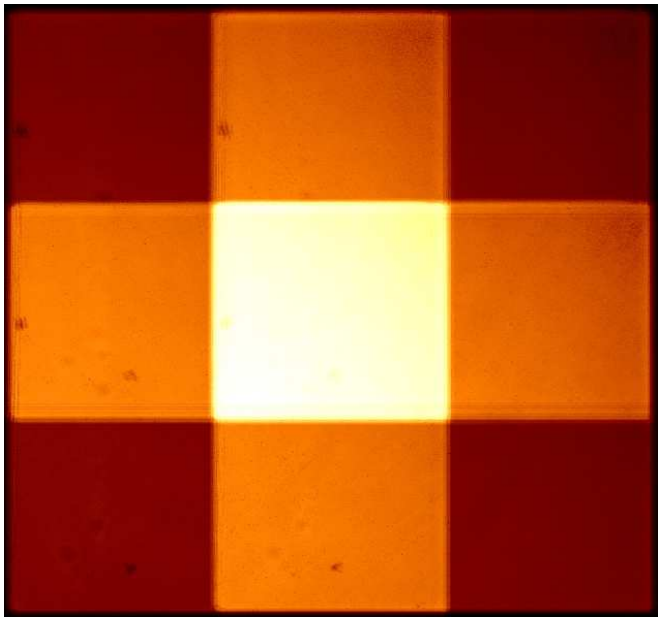

Figure 3.8. Weight image

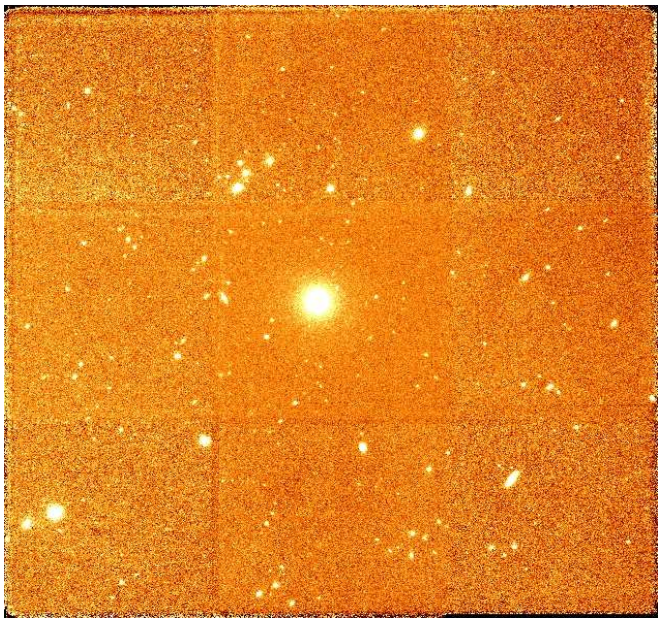

Figure 3.9. Final image of VCC 0200 in K-band

CHAPTER 4

Photometry

4.1 Introduction

Photometry is the direct measurement of the energy output of an astronomical source at several wavelenghts and therefore set constraints on the models of their structure.

The Greek astronomer Hipparchus divided the naked-eye-stars into six brightness classes. He catalogued over 1000 stars and rank them by "magnitude" one through six, from the brightest to the dimmest. However, the system was based on the nonlinear response of the human eye. Then it was suggested by Pogson [1856] that stars of the first magnitude were roughly 100 times brighter than the stars of the sixth magnitude. His suggestion was to make this as a standard, so each decrease in magnitude represented a decrease in brightness equal to the $100^{\frac{1}{5}}$ or about 2.512. This relation is often referred to as the *Pogson Scale*, that is

$$\frac{F_1}{F_2} = \left(10^{\frac{2}{5}}\right)^{m_1 - m_2} \tag{4.1}$$

or mostly known as

$$m_1 - m_2 = -2.5log(F_1/F_2) \tag{4.2}$$

where F_1 and F_2 are the intensities, and m_1 and m_2 are the magnitudes of two stars. As an additional information, the human eye can generally determine the brightness of one star relative to the nearby stars with an accuracy ~ 0.2 magnitudes.

4.2 Photometric Calibration and Aperture Photometry

The basic principle of aperture photometry is to sum up the observed flux within a given radius from the centre of an object, then subtract the total contribution of the sky background within the same region, and leave only the flux from the object to calculate an instrumental magnitude.

Depending on the CCD, or the conditions of weather; seeing, tracking, and focusing errors affect the amount of flux within the object's (e.g. star, galaxy, etc...) profile. Therefore the aperture size is quite important since the noise raises linearly with the radius, that increases the poisson shot noise of the background sky, and causes some flat-field errors. Also, when the aperture size incerases the stellar flux, relative to background, declines in the wings of the profile. The signal-to-noise

ratio of the flux measurement reaches a maximum at an intermediate aperture radius shown by [Howell, 1989]. However, the use of smaller radius introduces the problem that the fraction of the measured total flux will vary for objects of different flux from image to image which makes the aperture corrections very important. Therefore while some astronomers use large apertures for their mesurements in order to account for seeing, tracking, and focusing variations, the others use small apertures and apply aperture corrections. This cause the resultant magnitude slightly vary from one astronomer to another depending on their selection criteria [Wells, 1994].

4.2.1 Instrumental Magnitudes

The observed intensity is related to the astronomical object's intensity in a very complicated way. There are two groups of problems;

- Extinction because of absorbtion or scattering of the object's radiation on its way to the detector
- The departure of the detecting instrument from an ideal detector

E.g., for stars, the observed intensity, F_λ, is related to the actual stellar intensity, F^*_λ, outside the Earth's atmosphere by

$$F_\lambda = \int \phi_A(\lambda)\phi_T(\lambda)\phi_F(\lambda)\phi_D(\lambda)F^*_\lambda d\lambda \tag{4.3}$$

where $\phi_A(\lambda)$, fractional transmission of the Earth's atmosphere, this is because the atmosphere does not transmit all wavelengths freely;
$\phi_T(\lambda)$, fractional transmission of the telescope, this is because not all telescopes transmit light in the same manner and this can be a function of wavelength;
$\phi_F(\lambda)$, fractional transmission of the filter, this is because it is impossible to measure the intensity of the light from a star at one wavelength. Any filter transmits light over an interval of wavelenghs. No two filters can be made with exactly the same characteristics;
$\phi_D(\lambda)$, fractional efficiency of the detector, this is because apart from the similar problems with filters, also the noise characteristics of any electronic detector is a function of temperature.

As a result of including all these effects, no two observers measure exactly the same intensity for a given object. Fortunately, in order to determine the magnitudes, it does not need to add all these factors because the magnitude scheme requires only that certain stars be defined to have certain magnitudes, so that the magnitudes of other stars can be determined from the ratio of observed intensities that are corrected only for atmosperic effects. In order to correct problems caused by the individual differences among telescope, filter, and detector, a set of standard stars should be observed. By observing a set of known stars, it is possible for each observer to determine the necessary transformation coefficients to transform their instrumental magnitudes to the standard system. Another method to correct these factors is the "Differential Photometry", that compares the new magnitudes with previously calibrated magnitudes. In this research rather using standard stars, Differential Photometry with 2MASS (2μ - 2 Micron All Sky Survey) is used for calibration and to determine the instrumental magnitudes IRAF "Apphot" package is used. The intend of calibration is to recover the zero points of the images and getting the accurate magnitudes of the target galaxies.

4.2.2 2MASS

2MASS [1], 2 Micron All Sky Survey is a survey aimed to obtain deeper view of the sky in the near-IR with a sensitivity 50,000 times greater than the previous survey TMASS. It began in 1997 and completed in 2001 by using two telescopes located one in the northern and one in the southern hemispheres (Mt. Hopkins Arizona and Cerro Tololo/CTIO Chile, respectively) to cover the entire sky.

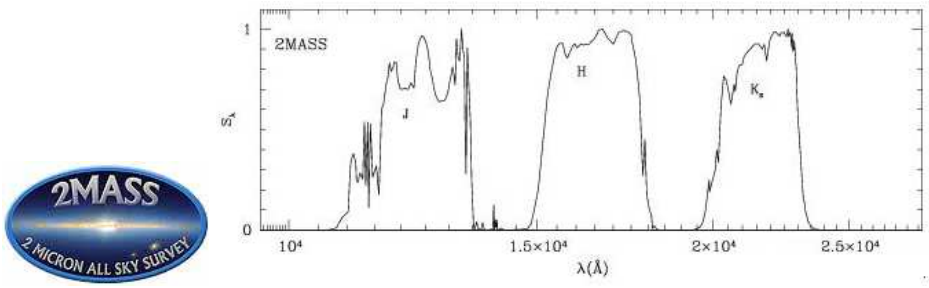

Figure 4.1. 2MASS system response curves for photometric system.

They used the photometric system of three infrared bandpasses of J, H & K_s (Fig. 4.2.2, Table 4.1) and observed up to the limiting magnitudes of 15.8, 15.1, and 14.3, respectively. According to the 2003 Data Release, 470,992,970 point sources and 1,647,599 extended sources are detected and the survey covered 99.998% of all the sky [Skrutskie et al., 2006]. In this research, we used the benefit of these images in order to calibrate our near-IR images. However, our images were quite higher resolution than 2MASS images therefore it increased the errors determining the magnitudes during calibration around 0.2 magnitudes.

Filter	**Wavelength (μm)**
J	1.25
H	1.65
K_s	2.17

Table 4.1. The definition of 2MASS Filters' wavelength limits

4.2.3 Calibration of Near-IR Images

Here, the steps of calibration and aperture photometry done by IRAF Apphot package is given.

Apphot Tasks and Determining the Aperture Size

For 2D detectors like the CCD's which our images were obtained, the standard method for sky or background determination is to take an annulus around the source, look at the pixel values within this area, and use the same algorithm to determine the value that is to be assigned to the background. This value is than subtracted on a per-pixel basis, from the total counts within the source, to obtain

[1]Two Micron All Sky Survey, is a joint project of the University of Massachusetts and the Infrared Processing and Analysis Center/California Institute of Technology, funded by the National Aeronautics and Space Administration and the National Science Foundation.

a measure of the collected flux. For this purpose, we used the "Apphot" package [Davis, 1989] which has set of tasks for performing aperture photometry to the uncrowded fields in interactive mode. The principle task `phot` computes accurate centres, sky values, and magnitudes of the objects in the image. Before that, some of the parameters also have to be set by the following algorithms.

Centering Parameters

The "centering algorithm" parameters are set by `centerpars` command. Apphot offers three sort of centering algorithms, which are *centroid*, *gauss*, and *ofilter*; we applied *centroid* algorithm because it is recommended for the images which are not crowded and noisy. The rest of the parameters kept with the default in the process.

Sky Fitting Parameters

The sky fitting algorithm parameters are set by `fitskypars` command. Apphot offers ten sky fitting algorithms, but *median* is applied in our images for the sky pixel distribution. This parameter set once and not changed for different images.

Here, the important parameters that have to be checked for every images are *annulus* and *dannulus* which are the "inner radius" and "width of the sky annulus" respectively. To make the comparison bright and unsaturated stars are matched in both 2MASS image and our image.

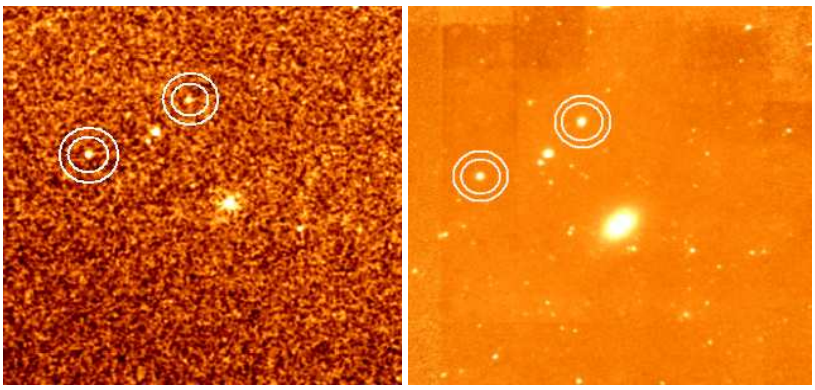

Figure 4.2. Annulus and dannulus Left: 2MASS image; Right: NICS image

As explained in the beginning of this section choosing the aperture size is quite important, and unfortunately IRAF does not do it automatically. As seen in the Fig 4.2, the *annulus* is selected bigger than the size of the star as seen by eye. This is because we want to contain all the light from the star. In fact, this is not quite possible because we cannot predict where the star ends in the image, since the wings of the star's profile extend much further. King [1971] discusses that a star's profile is affected by various phenomena of atmospheric refraction, instrumental diffraction and scattering. So its telescopic image could be much larger than the theoretical pattern. Under these unclarity, a aperture growth curve of a radius-magnitude diagram like in Fig 4.3 is plotted for every star and galaxy in order to include all the flux emitted by the star.

Photometry Parameters

The photometry algorithm parameters are set by `photpars` command. The default value "constant" is applied for photometric weighting scheme. For the "apertur",

a list should be given for radius in order to obtain different intensity values from the center to some certain FWHM multiples. As seen in the Fig 4.3, the flux of a

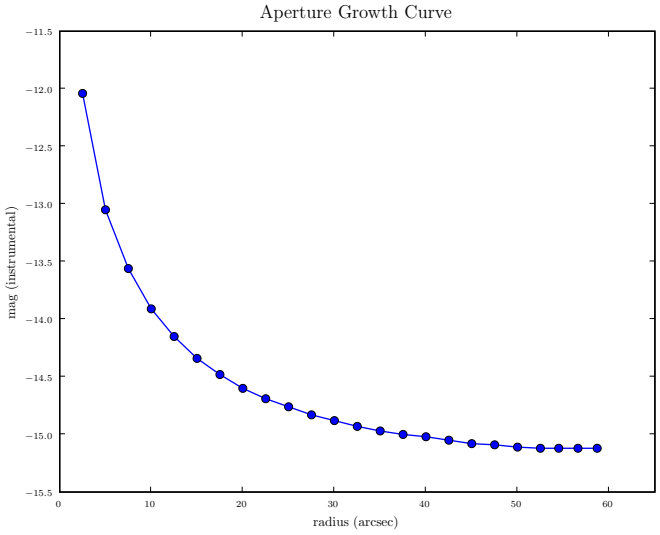

Figure 4.3. Aperture growth curve of a galaxy is used to determine instrumental magnitudes.

galaxy becomes constant as we move away from the center. The value of where the plot becomes constant is taken as the instrumental magnitude.

"Zero Point" (ZP) is defined as the difference between standard magnitude and instrumental magnitude.

$$\mathrm{ZP} = m_{\mathrm{std}} - m_{\mathrm{inst}} \tag{4.4}$$

After we obtain the instrumental magnitudes from the stars of 2MASS image and our image, we then calculate the Zero Points of our images by the sum of 2MASS image's Zero Point and the difference of the same star's 2MASS instrumental magnitude and our image's intrumental magnitude

$$\mathrm{diff} = m_{\mathrm{2MASS,instr.}} - m_{\mathrm{our,instr.}} \tag{4.5}$$

$$\mathrm{ZP}_{\mathrm{our}} = \mathrm{ZP}_{\mathrm{2MASS}} + \mathrm{diff} \tag{4.6}$$

After having the Zero Point of our image, then it is easy to calculate any magnitude from our images. Galaxy magnitudes are determined by

$$m_{\mathrm{galaxy}} = \mathrm{ZP}_{\mathrm{2MASS}} + \mathrm{diff} + m_{\mathrm{our,instr.}} \tag{4.7}$$

this is actually equivalent to

$$m_{\mathrm{galaxy}} \equiv (m_{\mathrm{galaxy}} - m_{\mathrm{2MASS,instr.}}) + (m_{\mathrm{2MASS,instr.}} - m_{\mathrm{our,instr.}}) + m_{\mathrm{our,instr.}} \tag{4.8}$$

and canceling out the same parameters leave us the magnitude of the galaxy.

4.2.4 SDSS Photometric Calibration and Sky Subtraction

The SDSS calibrates its photometry using observations of a network of standard stars established by the United States Naval Observatory (USNO) 1 m telescope,

and its astrometry using observations by an array of astrometric CCDs in the imaging camera. The surface brightness zero points are calculated through the formula (Eq. 4.9) given by Pohlen and Trujillo [2006]. It is done by using the *aa* (photometric zeropoint), *kk* (extinction term), and *airmass* coefficients out of the "TsField" table for each image. From these values, the surface brightness zero points are calculated as

$$\mathrm{ZP_{SDSS}} = -2.5\times(0.4\times[aa+kk\times\mathrm{airmass}])+2.5\times log\left(53.907456\times 0.396^2\right) \quad (4.9)$$

where 0.396"/pixel is the pixel scale and 53.907456 second is the exposure time for each SDSS image.

In the next chapter we will define Bruzual and Charlot [2003] Model for Stellar Population Synthesis. In this model, the colours are given as $UBVRI$ broadband colours, therefore we transformed these colours to SDSS colours using the synthetic transformation equations given by Smith et al. [2002].

$$g = V + 0.56(B-V) - 0.12 \quad (4.10)$$

$$r = V - 0.49(B-V) + 0.11 \quad (4.11)$$

$$u - g = 1.38(U-B) + 1.14 \quad (4.12)$$

$$g - r = 1.05(B-V) - 0.23 \quad (4.13)$$

The sky subtraction is one of the most important step for the study of surface brightness profiles at very faint levels. We again used Apphot in order to get the approximate value of sky near the galaxy. Then we subtracted this value from the image. However, this value is not the exact sky value to be taken into account. We used two additional methods to determine the most correct sky value.

Firstly, we selected 4-5 rectangular boxes of around 100x100 pixels as close as possible to the galaxy. These boxes are also clear of foreground stars or other structures in the image. Within each box we determined the mean sky after 5σ clipping iterations to remove unavoidable contamination by faint foreground stars. The standard deviation of these mean values gave the finer determination of the sky.

Secondly, we ran the "Galphot" ellipse fitting tool which will be explained in detail later. The ellipses extend the fit beyond the galaxy through background. Therefore we could easily derive the value of sky background from the end of the table. Then this value also subtracted as the final sky subtraction step.

4.2.5 Seeing Effects on Surface Photometry

It was first introduced by [Schweizer, 1979, 1981] that the importance of seeing on observed parameters like the core radius and central surface brightness of the galaxies. He showed that these effects can be significant even if the observed core radius is much larger than the seeing, and that they depend not only on the FWHM of the stellar PSF (Point-Spread Function), but also the wings of the PSF. Further work by Bailey and Sparks [1983] & Kormendy [1985], confirmed Schweizer's analysis. In order to take into account this effect, we first determined the seeing of all the images. Then we used the IRAF task `gauss` to convolve the data with Gaussian from the best seeing image to the worst seeing image by the following formula; (E.g., u band image has the worst seeing and we want to convolve z band image to u band image.)

$$\sigma = \frac{\sqrt{\sigma_u^2 - \sigma_z^2}}{2.3548} \quad (4.14)$$

where 2.3548 is the convertion factor of a FWHM to a σ for a gaussian.

4.3 Surface Photometry

Surface Photometry of galaxies is a technique in order to describe the light distribution of the galaxies quantitatively. From this technique in different bandpasses, it is possible to derive the colours and gradients of the galaxies which also provide the information about the ages and metallicity of the stellar populations in the galaxies. This is especially true for dwarf galaxies because they are still quite faint objects even for our advanced telescopes. Though, giant galaxies can be resolved so we can measure its surface brightness at each point of the image. With this technique, for unresolved extended objects it is also possible to determine more quantities like how the intensity and ellipticity vary with the radius, position angle, morphological type etc. Surface photometry technique can only be applied where the magnitudes of individual stars cannot be measured, therefore for crowded stellar fields like globular clusters, this technique is not useful.

4.3.1 Ellipse Fitting Routines

Surface photometry of galaxies is usually done by fitting ellipses to the isophotes. Ellipses are chosen because the isophotes of galaxies are not far from ellipses. There exist several software packages for deriving surface photometry. In this research we used "Galphot" program package for this purpose. The subroutines in Galphot use STSDAS fortran interface to IRAF. It is written by Franx et al. [1989] and later development by Inger Jorgensen.

4.3.2 GALPHOT

The surface photometry programs in Galphot are designed to determine profiles of intensity, ellipticity, position angle, centre position, boxiness, etc. of extended objects. The programs simply try to minimize the residuals between the model and the data. The main task `ellipfit` works to fit ellipses to the galaxy. It works over two processes. Firstly, determine the objects in the image and secondly full ellipse fitting to the galaxies.

Determining Objects in the Image

Since our galaxies are quite small, there is quite big unnecessary area in our images and for our aim it is better to crop these regions from the image. Therefore we put our target galaxy in a square box with a size of a few times the size of the galaxy. Then the positions of bad regions, stars, other galaxies were listed in a text file (See Fig. 4.4). And as a last step we determined the accurate centres of the galaxies. We first find the approximate center by imexam and then used IRAF task `imcntr` to go more accurate. Briefly, the algorithm in the `imcntr` computes the sum of all the rows and the sum of all the columns in the extraction box which is called "marginal distributions". The center in x (column value) is then the center of gravity of the row marginal, and the center in y is the center of gravity of the column marginal. If the resultant x or y center value deviates from the original input approximate starting points by more than 1 pixel, the process is repeated once more around the new center.

Ellipse Fitting

The full ellipse fitting to the galaxy images is a 3 step procedure [Franx et al., 1989, Milvang-Jensen, 1997]. Firstly, a harmonic expansion along concentric circles is performed. Secondly, the residuals from this expansion are used to flag additional

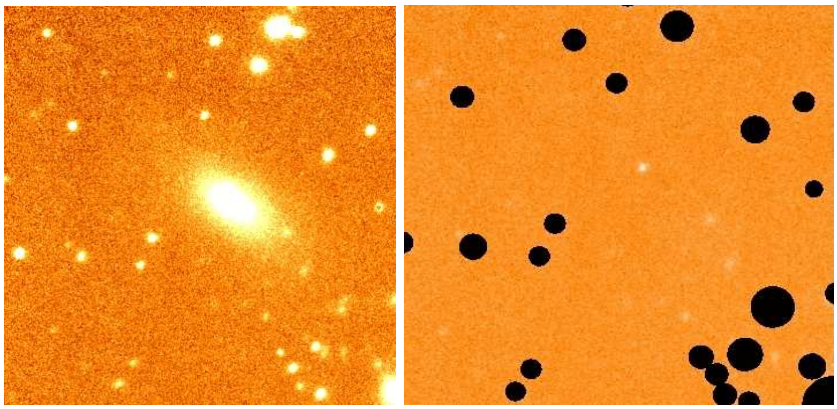

Figure 4.4. Before and After image, that is cropped to work on the galaxy in the image center

pixels. And thirdly, the actual pixel ellipse fit performed, using another harmonic expansion to calculate an initial guess.

As explained earlier, we determined the centre manually, and the harmonic expansion is done as along the concentric circles with this centre. Then a 6 term harmonic series is fitted to the intensities I. The series is defined as

$$I(r,\varphi) = I_0^{(c)}(r) + \sum_{n-1}^{6} \left[A_n^{(c)} \sin(n\varphi) + B_n^{(c)}(r) \cos(n\varphi) \right] \tag{4.15}$$

where r is the radius, φ is the position angle (measured from the CCD x-axis counterclockwise), and the superscript c denotes that we are fitting along circles. In the package, discrete radii r_i is used and they are calculated as

$$r_i = r_{\min} \cdot s^{i-1}, i = 1, 2, ..., N_{max}. \tag{4.16}$$

In this way, equally spaced radii in $\log r \cdot r_{\min}$ was set to 0.3 pixels, and the scaling factor s was usually set to 1.1, giving the radius sequence 0.3 pixels, 0.33 pixels, 0.363 pixels, ... Here, $r_{\min}$ has to be as small as 0.3 pixels in order to get a good fit of the central pixels of the galaxy. The max. radius number N_{max} is basically determined from the condition that 60% of the circle needs to be within the image. For pixels outside the max. radius only the intensity fitted. The pixels contaminated by other objects are rejected from the fit above.

A difference image is generated which shows the residuals from the ellipse fitting procedure. It is simply calculated by subtracting the fit from the original image. This image has a mean of zero, with stars, bad pixels superimposed, allowing a simple and straightforward detection algorithm to be used. All pixels deviating by more than 5-10 times the rms noise are also flagged. The harmonical fitting was repeated, and the residuals were inspected again to check that all bad pixels and interfering stars had been found and flagged. This method is more reliable than any method that tries to determine the bad regions from the original image, while it takes much less time than a full solution of the ellipse fitting program on an image.

At the next step, the ellipse fitting procedure was applied to the image, using the above harmonic expansion along the concentric circles. From the resulting Fourier coefficients, initial guesses on the centre of the ellipses x_c, y_c, the Intensity

profile I(r), the ellipticity $\epsilon(r)$, and the position angle PA(r) are calculated from the centre to the very edge of the galaxy. The structural parameters were determined about 100-160 pixels from the centre. We also determined another interesting coefficient Boxiness c_4, since it is an indicator of whether a galaxy is disky ($c_4 \rangle 0$) or boxy ($c_4 \langle 0$) [Carter, 1987, Bender et al., 1989, Peletier et al., 1990].

Details on Ellipse Fitting

While applying the ellipse fitting, we keep the centre ($x_c(r)$ and $y_c(r)$) and the shape $\epsilon(r)$ and PA(r) as free parameters since these parameters are not constant with radius in galaxies. Besides, at some point in the profile the signal-to-noise ratio becomes too low to keep the centre and the shape as free parameters. It is better to mention some specific terms that was used in GALPHOT. `ellipfit` task is the main task which does the ellipse fitting. We first started using the default values for the different parameters that control the fit at `ellipfit` task. However, depending on the image some of the parameters had to be tuned with some specific parameters in the task. Especially `errscap` and `errcen` which are the maximum error in shape and in position of ellipse respectively; and `cliplow` and `cliphig` which are the fraction of points to clip at low and high ends were tuned in order to obtain a good fit. `dposmax`, `dellmax` and `dangmax` are the parameters which control how much the centre position, the ellipticity and the position angle are allowed to change at a given radius per iteration step. The output residual image is still the same `.fits` format and output radial profiles are STSDAS table format. After running the `ellipfit` task, we examined the residual image and the corresponding output table in order to correct if there are any overlapping ellipses at some radii. If so, we continued to tune the parameters above to get a good fit.

As mentioned before, for SDSS images we aligned all the five bands' images and determined the centre of the galaxy from the r band image. Since we deal with the colours, we used the output fit table of r band as an input to the other bands. Then we got more accurate pixel-to-pixel aligned fit tables for each band. The same method but H band's centre was used as an imput for near-IR images.

GALPHOT also has a different definition for the Position Angle. The standard way of measuring the position angles are from north through east. However we needed to do the following transformation in order to obtain the standard PA.

$$\mathrm{PA}_{std} = \mathrm{PA}_{\mathrm{GALPHOT}} - 90^{\circ} \tag{4.17}$$

The resulting table of Galphot gave the surface brightness profiles, position angle, center position, ellipticity and colours.

4.3.3 Errors

After applying ellipse fitting to the images, we employed the `model` task in Galphot which creates a galaxy subtracted image by subtracting the output profile table from the image. We used the same method of sky determination as explained above over these images in order to calculate the errors. We selected 4-5 rectangular empty boxes of around 100x100 pixels as close as possible to the galaxy. Then we determined the mean value of these areas. The standard deviation of these mean values gave our final error.

4.3.4 GOLDMine

GOLDMine, (Galaxy On Line Database Milano Network) database is a multiwavelength database of optically selected sample of galaxies mainly from Virgo Cluster and Coma Supercluster [Gavazzi et al., 2003]. [2]. In the database there are optically selected sample of 3267 galaxies representative of all morphological types and luminosities which were observed through UV to cm radio. In this research, we used the H and K magnitude of some of the galaxies in order to cross-check with our sample. The total near-infrared (J, H, K) magnitudes comptuted at the radius (25^{th} magnitude/arcsec^2). The assumed photometrical uncertainties are 15% for H and 20% for J and K [Gavazzi and Boselli, 1996].

4.3.5 Comparison of Photometry

We compared our photometry with literature which were published by GOLDMINE database. Determining the aperture magnitudes were mentioned before in this chapter. Comparison of our H magnitudes agree around 10%, and our K magnitudes agree around 20% uncertainty (Fig 4.5).

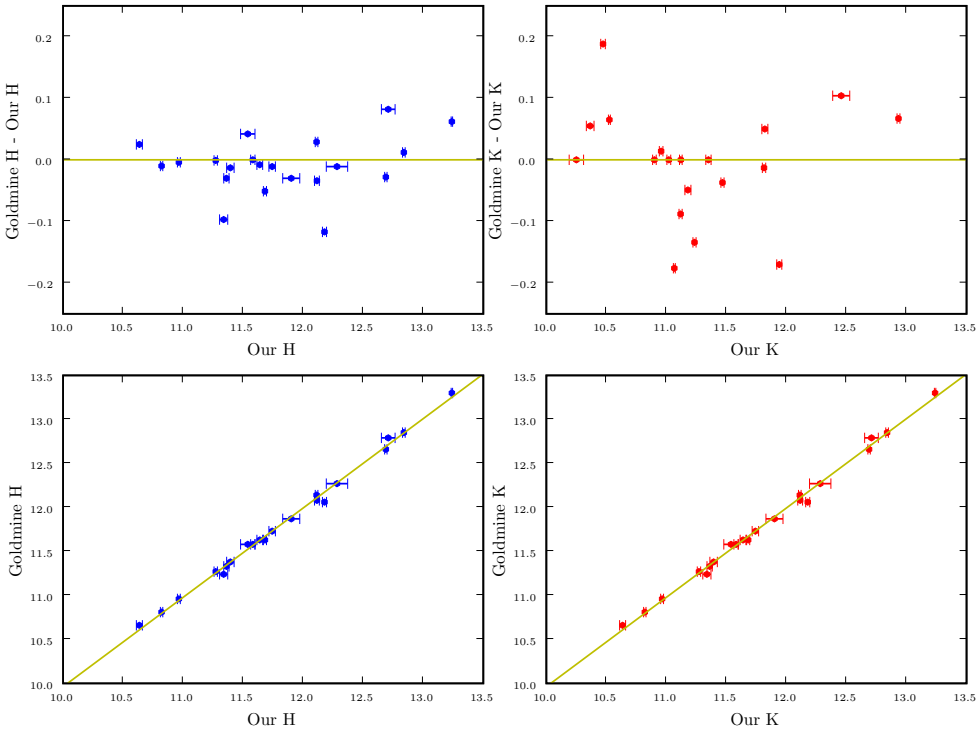

Figure 4.5. Comparison of Goldmine and our magnitudes determined by aperture photometry.

[2]This research has made use of he GOLDMine Database, operated by the Universita degli Studi di Milano-Bicocca.

CHAPTER 5

Stellar Populations Synthesis

5.1 Stellar Populations

Within a galaxy, stars in a group resemble each other with some properties like spatial distribution, chemical composition or age. These groups are called "Stellar Populations". The study of Stellar Populations gives insight into the different generations of stars which make up a galaxy and therefore is the principal way to determine the life and history of galaxies.

Their main properties can be described briefly. Stellar populations are

- fossils of past star formation epochs
- tracers of stellar properties and evolution at different metallicities and different environments
- tracers of galaxy evolution
- tracers of mass distribution in galaxies

Stellar Populations are most useful as tracers of events in a galaxy's past and during its formation. The key defining common properties are "Age" and "Metallicity". Like stars, they are categorized as Population I, II, or III, depending on their metallicity.

Population III

In the first moments after the Big Bang, the matter in the Universe consisted almost entirely of Hydrogen (H). Through primordial nucleosynthesis, a sizeable proportion of Helium (He) and only trace amounts of Lithium (Li) and Berillium (Be) were created. This continued until the Universe became too cool and the matter become too scattered. Therefore, the first stars, referred to as "*Population III*", had virtually no metals at all when they formed. With only these materials, the stars that we see today could not have been able to form. This is because the metals help the energy escape from the star and cool them down. Without that ability of cooling off, the stars get big, hot, and have very short lifetimes like a few million years. Their typical masses are expected to be up to several hundred solar masses. Currently no Population III stars have been found so far, however, their existence is predicted from the current cosmological models and gravitational lensing studies [Fosbury et al., 2003]. It is believed that these stars triggered the Epoch of Reionisation "EoR", because during their lives, they created the elements

up to Iron (Fe) via nucleosynthesis.

Population II

After the death of these first stars, with the materials left by them, the next generation of stars known as "Population II" were born. These are metal-poor stars, named in this way because of their low metal contents, and contain about 0.1% metals. Besides this, they are relatively old stars, with ages ranging from 2 - 14 Gyr, which makes them also the oldest observed stars. Population II stars make up the overwhelming bulk of the Stellar Populations in elliptical galaxies following highly elliptical orbits around the galactic center. They also tend to be found in globular clusters and near the nuclei of galaxies. They tend to be older, less luminous and cooler than Population I stars. They have fewer heavy elements, either by being older or being in regions where no heavy-element producing predecessors would be found.

Population I

As those Population II stars died, they returned metal-rich material to the interstellar medium by supernova explosions or by planetary nebulae which then become a womb for newer stars. These youngest stars therefore have the highest metal content; containing about 2-3% metals are known as the "Population I" stars. They have formed within the last few hundred million to a few billion years. The Sun, located in the disk of the Milky Way, is also considered a Population I star. Most of the Population I stars are concentrated in the disks of spiral galaxies in the same way. They travel in circular orbits about the center of the Galaxy and generally remain in the plane of the Galaxy as they orbit. You can see a representation of the orbits in figure 5.1.

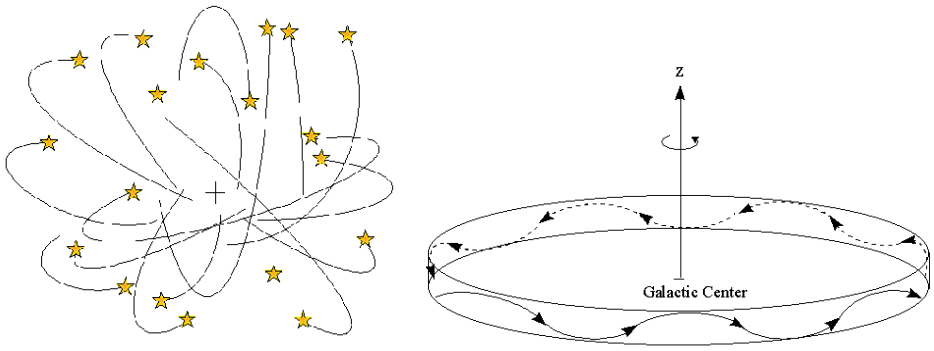

Figure 5.1. Right: Population II stars tend to lie around the center and in globular clusters. Stars have random orbits in the halo. Left: Population I stars lie in the disk of the galaxy. They have generally circular orbits in a spiral disk. Image taken from Websource2.

Stellar Populations in our Galaxy

The key to understand the formation our Galaxy is to determine the ages and chemical compositions of the various stellar populations within our galaxy. Our galaxy is comprised of three main parts; halo, disk and bulge. Observations show

that the oldest Population II stars are in the halo and the bulge. On the contrary, the most metal rich Population I stars are in the disk and the bulge. From this we can interpret that the halo formed first, whereafter the bulge and finally the disk. The halo contains individual old stars and large groupings known as globular clusters.

Extreme Population II stars (the most metal poor) are found in the halo and the globular clusters; these are the oldest stars. Intermediate Population II stars are located in the bulge. They are slightly more metal rich than the extreme Population II stars, but less metal rich than the intermediate Population I stars.

Population I stars include the Sun and tend to be luminous, hot and young, concentrated in the disks of spiral galaxies. They are particularly found in the spiral arms. With the model of heavy element formation in supernovae, this suggests that the gas from which they formed had been seeded with the heavy elements formed from previous giant stars. About 2% of the total belong to Population I. The location of these different populations in our galaxy is depicted in Fig. 5.2.

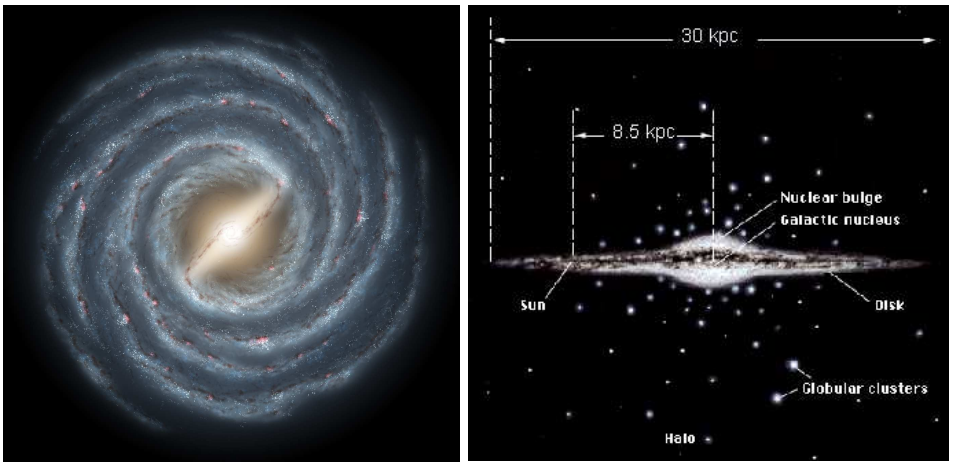

Figure 5.2. Distribution of Stellar Populations in the Milky Way. Image taken from Websource1

5.1.1 Metallicity

As explained earlier, "Metallicity" is a measure of the mass of elements in an object heavier than H and He. The metallicity of an object provide an indication of its age. Since only H and He with very small trace amounts of Li and Be were produced by the primordial nucleosynthesis at the very early Universe, all of the Fe and other metals in the Universe have been produced in stars. When a star reaches the end of its life, it recycles some or all of the elements which it had produced in its core over its lifetime back into the interstellar medium. This material becomes mixed into clouds where the next generation of stars are born. So each next generation of stars is enriched with the metals produced in previous generations. Then it is possible to infer that in a galaxy, stars with a lower metal content are older than stars with a higher metal content.

Most often measurements of absorption lines in a stellar spectrum are used to measure the amount of the present Fe. Absorption lines invoked by H are analyzed in a similar manner to obtain the amount of H. The ratio of the amount of Fe to that of H in the object is divided by the ratio of the amount of Fe to H in our Sun to obtain a metallicity relative to the Sun. The metallicity of the Sun is $\sim 1.6\%$ by mass. For other stars, the metallicity is expressed as "[Fe/H]", which represents the logarithm of the ratio of a star's Fe abundance compared to that of the Sun. The formula is expressed as

$$[Fe/H] = \log\left(\frac{N_{Fe}}{N_H}\right)_\star - \log\left(\frac{N_{Fe}}{N_H}\right)_\odot \tag{5.1}$$

Here N_{Fe} and N_H are the number of Fe and H atoms per unit volume respectively. Therefore, stars with a higher metallicity than the Sun have a positive logarithmic value, while those with a lower metallicity than the Sun have a negative value.

This is quite useful, because using the concept that stars with similar properties are grouped together in a galaxy and thus by determining the ratio [Fe/H] of a star, it helps to identify to which population that star belongs to. Therefore, it is easy to estimate its age. For example, in our galaxy [Fe/H] of the halo is -1.6, therefore with this small amount of metals it can be inferred that the halo consists the oldest stars and thus it could have been formed first. This kind of small metallicity is not found in the disk of our galaxy so we can infer that the disk is formed later than the halo. This way, by studying all the regions in a galaxy it is possible to determine star formation history of a galaxy.

5.2 Stellar Population Synthesis Models

Stellar Population Synthesis Models are tools for interpreting the integrated light, such as colours, line indices and M/L that is observed from galaxies. We used the Stellar Population Model from Bruzual and Charlot [2003] for our analysis. It is a model for computing the spectral evolution of stellar populations at ages between 1×10^5 and 2×10^{10} years at a resolution of 3 $\mathring{A}$ across the wavelength range from 3200 to 9500 $\mathring{A}$ for different metallicities. The model predictions are based on high resolution library of observed stellar spectra. Even if using the advanced high resolution technology there are still important limitations for the models such as stars being very bright and having strong influence on integrated-light properties when they are at the asymptotic giant-branch phase and supergiant phase [Yi, 2003]. These limitations affect the interpretation of galaxy spectra by arising uncertainties in age and metallicity.

5.3 Colour-Magnitude Diagrams

Looking for correlations between stellar or galactic properties give a lot of insight to better understand how stars and galaxies are constructed. A quite easy way to find a correlation is to make a plot of one intrinsic property vs. another intrinsic property. Intrinsic properties are the properties that do not depend on distance. Examples of intrinsic properties are temperature, mass, diameter, composition, luminosity, etc. When an object is observed at narrow bands with different wavelengths, it will appear brighter in some bands than others. The difference between two bands is referred to as colour. The first and the most famous of these correlations is the H-R diagram. In 1912, Hertzsprung & Russell independently found a correlation between temperature (colour) and luminosity

(absolute magnitude) for 90% of the stars. These stars lie along a narrow diagonal band in the diagram called the "main sequence", see figure 5.3. This diagram is called after their founders and this plot of colour vs. absolute magnitude became a very good indicator in order to extract some properties of stars and for galaxy populations.

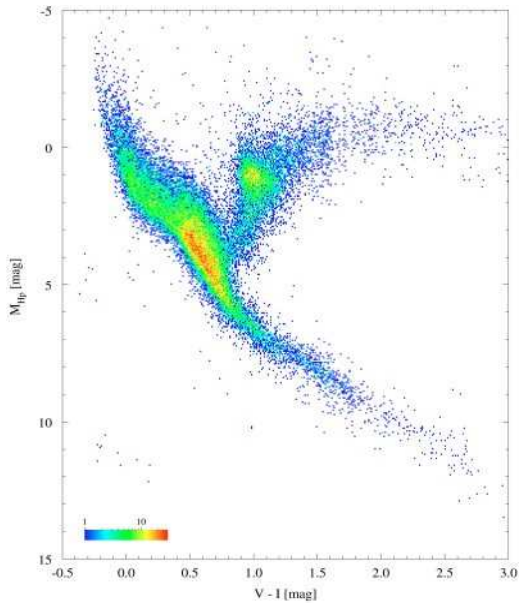

Figure 5.3. Actual HR Diagram Based on Hipparcos Data (ESA). The above image is a real HR diagram generated from data on 41453 stars in the Hipparcos catalogue.

Colour-Magnitude Diagrams are commonly used in resolved stellar population studies to derive star formation histories. If no information is available about the metallicity of individual stars, the only other accurate way of deriving star formation histories is by detecting main-sequence turn-offs. This is because the position of a star on the Colour-Magnitude diagram changes according to several factors, such as its age, metallicity and mass. Some specific features in Colour-Magnitude diagrams are indicators of the presence of young (<1 Gyr), intermediate age (2-8 Gyr) and ancient stars (>10 Gyr) stars. By counting the percentage of stars which are found in such features it is then possible to construct a simple star formation history of that population. However, for the unresolved stellar populations what we do in this research, the use of surface photometry allows us to detect if and how the star formation changed throughout the galaxy.

5.4 Colour-Colour Diagrams

Since galaxies are collections of stars, along with surrounding gas and dust, they will appear as the colour to which most of the luminous stars belong. When most of the luminous stars in a galaxy are blue, the galaxy will appear blue in its totality. Colour-colour diagrams are a means of comparing the apparent magnitudes at different wavelengths. To make a colour-colour diagram, the colour defined by two wavelength bands like "$(g - r)$" is plotted against the colour defined by another two wavelength bands like "$(u - g)$" (though usually there is one band involved in determining both colours, in this case "g").

CHAPTER 6

Results: Analysis of colours and line indices

In this research, we analyzed the past star formation activity in Virgo Cluster and field dwarf elliptical galaxies based on the combination of Stellar Population Synthesis and Spectral Synthesis models. For our research we obtained the colours and colour gradients of dwarf ellipticals (Tables B.1, B.2, B.3, B.4, B.5 and B.6). We looked for correlations by using the colour-colour, colour-magnitude, colour-gradients and colour-spectroscopic index diagrams and compared them with the literature.

All our results were deducted from the images of SDSS optical and Magpop-ITP near-IR data. The surface photometry results from individual galaxies are given in Appendix 1. The plots include the optical surface photometry of SDSS' u, g, r, i, and z bands, optical-NIR surface photometry of g, r and H, colour gradients of $g-r$, $r-z$, $u-r$, $g-H$, $r-H$, $H-K$, and also the parameters of ϵ, PA, B_4, and center position in X and Y. For some galaxies, observations in K band were not available or u band images were too faint or invisible, hence the plots for them are missing.

Finally, we derived the slopes of the colour profiles by using a least square fitting technique. We applied a fitting algorithm starting at a radius of twice the seeing FWHM from the center to the outer parts until the colour shows some scatter of around 0.1 magnitudes. The average number of data points used for the fitting is about 30. Even though this is a small number but we rejected the data points which have errors larger than 0.15 magnitudes.

6.1 Optical - Near-IR Colours

Our colours were determined in two ways, first through aperture photometry and second through surface photometry. For SDSS aperture magnitudes, we did not need to redo the determination of the integrated magnitudes since we could obtain them from SDSS database. For H & K magnitudes we used both techniques. The colour combinations which were determined using both ways in optical-optical and optical-near-IR colour diagrams are shown in the following figures. For comparison, the evolutionary tracks for three possible metallicities of Z=0.004, 0.008 and 0.02 are shown in the figure. The galaxy evolutionary tracks are obtained from the simple stellar population models of Bruzual and Charlot [2003]. This galaxy evolution model is an improved version of the composite stellar population models originally

described in Bruzual A. and Charlot [1993]. Here, this version of the galaxy evolution code includes options for sub- and super solar metallicity stellar populations which are essential for our analysis.

6.1.1 Quiescent and Star Formation Dwarfs; Colour Relations

Our near-IR sample also contain star-forming dwarfs from Virgo Cluster and field. Since studying star-forming dwarfs (dIrr) was not the main topic of this research, we at least determined their integrated magnitudes from aperture photometry in order to create colour-colour and colour-magnitude diagrams (Fig. 6.2) to see the correlations between quiescent and star forming dwarfs. Our H & K integrated magnitudes for all sample are shown in Table 6.1. In order to calculate the absolute magnitude M_H for field galaxies, the distance is calculated through their redshift. However for Virgo dwarfs, we used the cluster distance as a common practice rather than the redshift.

For comparison with van Zee et al. [2004], we plotted Fig. 6.1 with the optical colours. The integrated SDSS colours along with the reference are plotted in the left diagram, whereas the integrated colours of field and the colours of the quiescent dwarfs from surface photometry are plotted in the right diagram. The plots show that the location of quiescents quite agree with the reference and since our sample consists of more galaxies, it indicates that we have more redder ones than Van Zee. In Fig. 6.2, we also add NUV and FUV magnitudes from GALEX database. The Galaxy Evolution Explorer (GALEX) satellite observed galaxies in the far-ultraviolet (FUV, 1350-1750 $\mathring{A}$) at a resolution of 4".5. , and in the near-ultraviolet (NUV, 1750-2750 $\mathring{A}$) with a resolution of 6".0. The UV colours are obtained from Boselli et al. [2005]. They are very well separated and clearly show that the quiescents are placed in the redder region and star forming dwarfs are placed at the bluer region of the diagrams, so that a UV colour selection is quite good distinctor separating these two types..

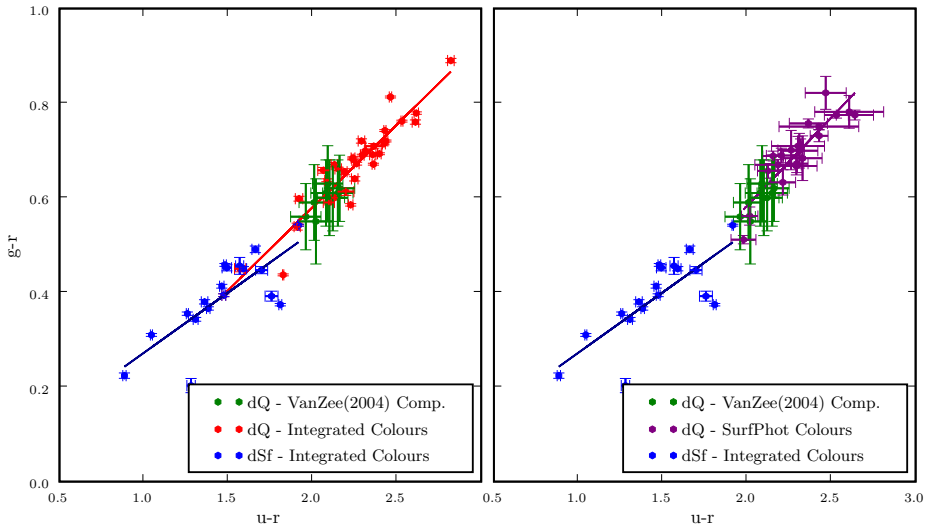

Figure 6.1. Comparison of our integrated colours and surface photometry colours with van Zee et al. [2004]

.

	Our Values				Zero Points		Goldmine		
Galaxy	**H**	err_H	**K**	err_K	ZP_H	ZP_K	**H**	**K**	M_H
CGCG119069	12.708	0.057	12.456	0.071	25.593	25.056	12.79	12.56	-21.375851
ID0028	14.037	0.021	13.842	0.027	27.300	25.481	-	-	-16.564456
ID0207	13.706	0.011	-	-	25.762	-	-	-	-17.955036
ID0615	11.000	0.015	-	-	24.550	-	-	-	-19.967676
ID0650	12.061	0.026	-	-	25.982	-	-	-	-19.099604
ID0734	12.920	0.013	12.705	0.024	26.749	25.321			-18.693938
ID0872	13.564	0.017	13.355	0.021	26.666	24.938			-17.365250
ID0918	11.015	0.012	-	-	25.432	-	-	-	-20.955532
ID1109	13.977	0.015	13.810	0.013	27.100	26.432	-	-	-17.969520
ID1186	14.203	0.014	-	-	25.583	-	-	-	-17.769745
ID1524	12.610	0.019	-	-	25.542	-	-	-	-17.646254
VCC0165	11.681	0.013	11.234	0.013	25.204	24.637	11.63	11.10	-19.471245
VCC0200	12.114	0.020	11.820	0.025	27.192	25.255	12.08	11.87	-19.038545
VCC0397	12.177	0.017			25.490	-	12.06	11.77	-19.632039
VCC0407	11.741	0.027	11.467	0.013	27.003	25.130	11.73	11.43	-19.411045
VCC0482	11.337	0.034	11.020	0.016	25.039	24.405	11.24	11.02	-19.815745
VCC0523	-	-	10.250	0.060	-	24.710	10.46	10.25	-
VCC0794	12.688	0.010	12.400	0.016	24.371	24.177	12.66	-	-18.464745
VCC0816	13.579	0.015	13.442	0.018	27.127	25.355	-	-	-17.573445
VCC0817	12.640	0.015	12.478	0.018	27.627	25.755	-	-	-18.512445
VCC0940	12.111	0.011	11.813	0.014	25.175	24.400	12.14	11.80	-19.041445
VCC0990	11.393	0.031	-	-	25.197	-	11.38	11.15	-19.759145
VCC1087	-	-	11.066	0.008	-	25.047	10.99	10.89	-
VCC1107	13.238	0.006	12.933	0.012	24.836	24.156	13.30	13.00	-17.914145
VCC1183	-	-	10.900	0.015	-	24.739	11.11	10.90	-
VCC1261	10.635	0.025	10.365	0.032	25.155	24.500	10.66	10.42	-20.517645
VCC1431	-	-	11.118	0.013	-	25.036	11.16	11.03	-
VCC1567	12.844	0.017	12.498	0.022	27.032	25.221	-	-	-18.307945
VCC1861	11.271	0.014	11.120	0.011	25.459	24.927	11.27	11.12	-19.880845
VCC1871	10.820	0.010	10.525	0.008	25.064	24.434	10.81	10.59	-20.332045
VCC1910	10.964	0.012	10.472	0.019	24.977	24.265	10.96	10.66	-20.187945
VCC1912	11.360	0.022	11.179	0.025	25.041	25.298	11.33	11.13	-19.792145
VCC1947	-	-	10.956	0.015	-	24.816	11.12	10.97	-
ID0118	13.575	0.022	-	-	26.250	-	-	-	-17.934595
ID0149	14.248	0.033	-	-	25.533	-	-	-	-17.516464
ID0154	13.727	0.034	-	-	25.881	-	-	-	-17.960914
ID0158	11.469	0.041	-	-	25.976	-	-	-	-20.359300
ID0365	12.488	0.038	-	-	25.780	-	-	-	-18.772183
ID0943	13.522	0.024	-	-	25.917	-	-	-	-17.722987
ID0957	13.118	0.015	-	-	25.619	-	-	-	-18.876023
ID12131	14.411	0.037	-	-	25.657	-	-	-	-17.387844
ID1225	13.825	0.011	-	-	27.016	-	-	-	-17.808542
ID1330	14.000	0.018	13.914	0.013	27.056	25.236			-17.548425
VCC0024	12.838	0.011	-	-	22.217	-	12.85	12.71	-19.687750
VCC0509	13.294	0.025	-	-	25.507	-	-	-	-18.514439
VCC0568	12.766	0.018	-	-	25.583	-	-	-	-19.042739
VCC0693	13.630	0.021	13.062	0.025	27.176	24.910			-17.522145
VCC0739	11.900	0.071	-	-	25.911	-	11.87	11.48	-19.252245
VCC0741	13.814	0.013	-	-	25.898	-	-	-	-17.338245
VCC0980	11.580	0.018	11.350	0.022	24.907	24.712	11.58	11.35	-19.572245
VCC1435	12.281	0.089	11.940	0.021	24.547	23.623	12.27	11.77	-18.871645
VCC1486	11.538	0.060	-	-	26.772	-	11.58	11.49	-19.614645
VCC1778	11.638	0.024	-	-	25.803	-	11.63	11.39	-19.514645

Table 6.1. Integrated Magnitudes determined by aperture photometry. Top table quiescent dwarfs, bottom table star forming dwarfs

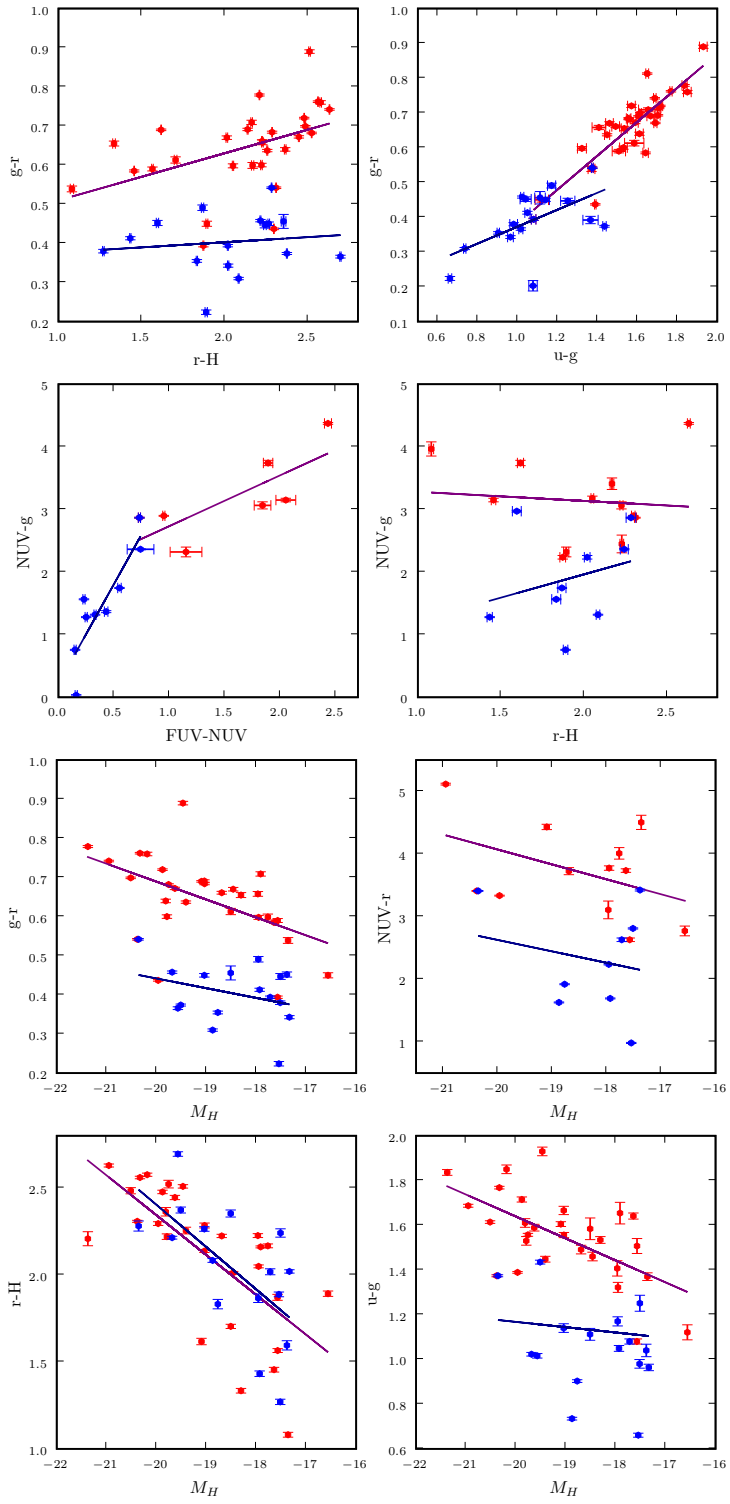

Figure 6.2. Colour-Colour and Colour-Magnitude Relations between Star Forming Dwarfs and Quiescent Dwarfs; Red: Quiescent Dwarfs, Blue: Star Forming Dwarfs

6.1.2 Quiescent Dwarfs; Colour - Colour Relations

From here on we focus the analysis of only quiescent (elliptical) dwarfs. As previously indicated we created colour-colour diagrams overlayed with Bruzual and Charlot [2003] Simple Stellar Population Model. In the next plots we use the colours determined from surface photometry. Tables B.1, B.2, B.3, B.4, B.5 and B.6 present the values of colours and gradients. In Fig 6.3, the observed colours of $g-r$ vs $r-H$, consistent with metallicities of $Z = 0.004$ to $Z = 0.02$ are presented. In the three different metallicities, the colours are indicative of an older stellar population with an age of approximately over 4-10 Gyrs. Much of the scatter in the observed colours can be attributed to the colour-magnitude relation for dwarf elliptical galaxies [Caldwell, 1983]. Generally, the dwarf ellipticals in our sample are redder than the sample of van Zee et al. [2004]. In contrast VCC0817, ID0650 and ID1524 are quite a bit redder in the diagram. They might have star formation in the centre and thus dominate the whole colour of the galaxy. Our $g-r$ vs $H-K$ diagram is quite scattered due to large uncertainties in our K band, which makes it impossible to infer such interpretation. Also our $u-g$ vs $g-H$ and $u-g$ vs $g-r$ diagrams confirm the known problem in the Bruzual and Charlot Model that their colours can easily be wrong by 0.1 mag. To conclude, these diagrams shows that the majority of dwarf ellipticals to have a solar or sub-solar metallicity which also agrees with the results in van Zee et al. [2004].

The average colours that we found from our sample are;
(g-r) $= 0.693 \pm 0.032$, (r-z) $= 0.582 \pm 0.058$, (u-r) $= 2.315 \pm 0.105$,
(g-H) $= 2.903 \pm 0.086$, (r-H) $= 2.221 \pm 0.086$, (H-K) $= 0.273 \pm 0.032$
which is also a similar range with low-luminosity elliptical galaxies presented by Prugniel et al. [1993] for optical colours.

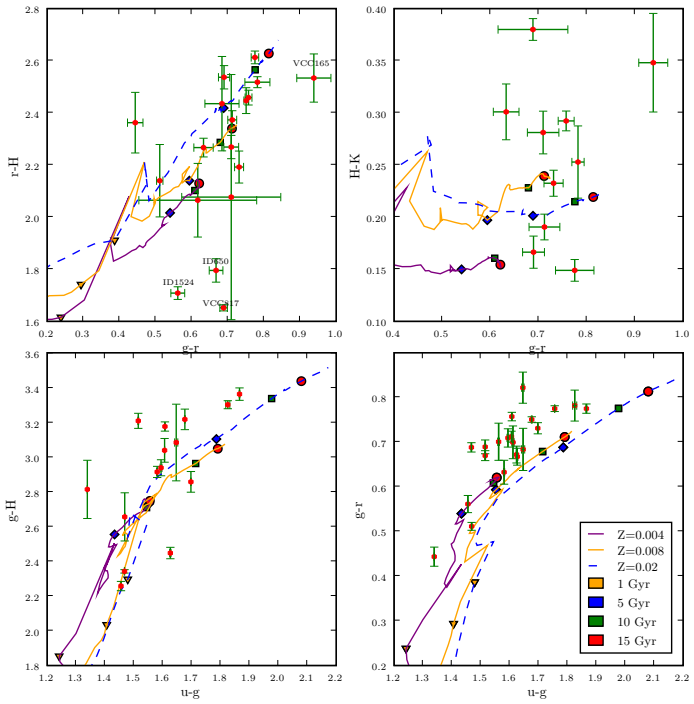

Figure 6.3. Optical - Near-IR colours of dwarf elliptical galaxies. Three evolutionary tracks for the metallicities of Z=0.004, 0.008 and 0.02 are shown from Bruzual and Charlot [2003]

6.1.3 Quiescent Dwarfs in Field and Virgo Cluster - Colour Relations

We separated the dwarf ellipticals and created colour-colour and colour-magnitude diagrams by their location. In Fig. 6.4, the black dots indicate the Virgo Cluster Dwarfs and green dots indicate the field dwarfs. As seen in these combinations of diagrams, there is no correlation by location could be seen whether they are in a group or standing alone in the Universe.

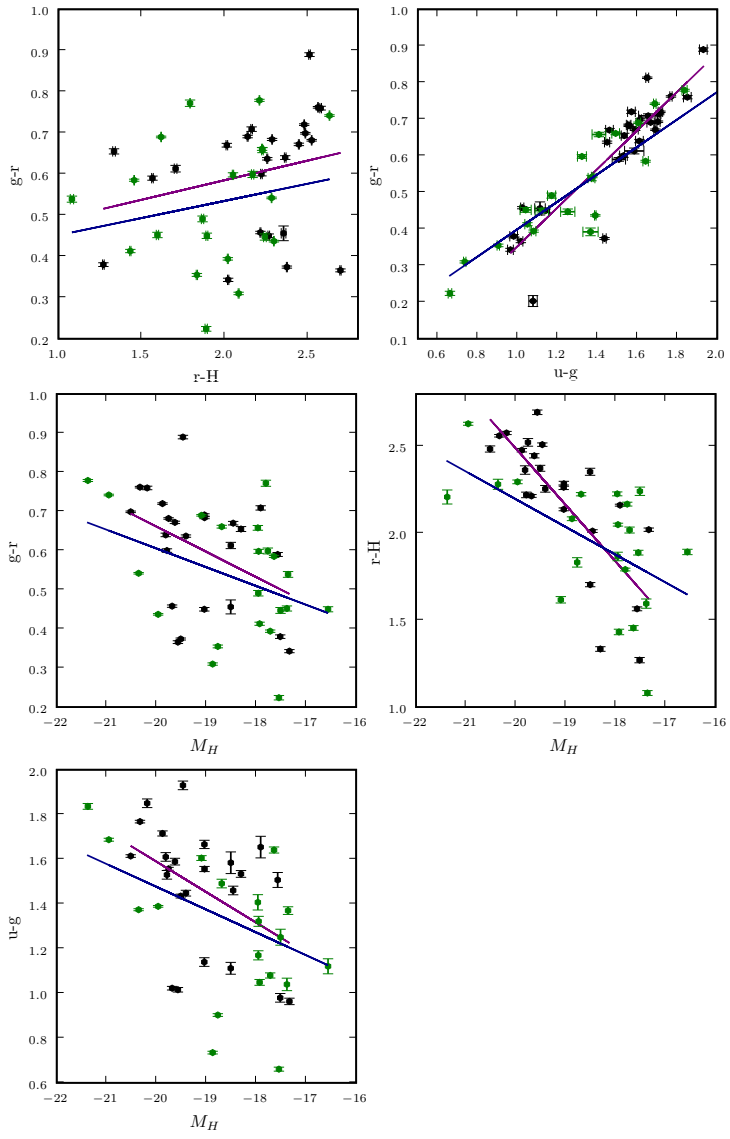

Figure 6.4. Colour-Colour and Colour-Magnitude Relations between Virgo Cluster Dwarfs and Field Dwarfs; Black: Virgo Cluster Dwarfs, Green: Field Dwarfs

6.2 Line Indices

In addition to the near-IR imaging programme, the Magpop-ITP collaboration also observed spectra of each of these dwarf galaxies. The results of spectroscopic lines indices vs colours are shown in Figures 6.5, 6.6 and 6.7. The spectroscopic results will be published by other Magpop-ITP collaborators. The first results, however, are already published by Michielsen et al. [2008] where we obtained the spectroscopic line index values (Table B.7).

6.2.1 Hydrogen Lines vs Colours

The most age-sensitive Lick/IDS indices are the Hydrogen Balmer series of Hβ, Hγ and Hδ. In Fig. 6.5, we plot the $u-g$, $g-r$ and $r-H$ colours vs Hβ, together with the Bruzual and Charlot 2003 Model for our dwarf elliptical sample. Our sample falls nearly into the same regions in three of the plots. Since there are some problems as explained before, the $g-r$ vs Hβ diagram would give the most reliable result and it indicates that the ages are mostly around 4-10 Gyrs with solar or sub-solar metallicity. In Fig. 6.6, we plot the $u-g$, $g-r$ and $r-H$ colours vs HγA, HγF, HδA and HδF as a check of the previous result. In the HγA, HγF and HδA diagrams our sample is seemingly not correlated with the model. This might indicate that this Stellar Population Models do not fit, so there could be an evidence for an additional young stellar population. However, HδF gives the same result as Hβ does. These samples again give around 4-10 Gyrs age with more or less solar metallicity.

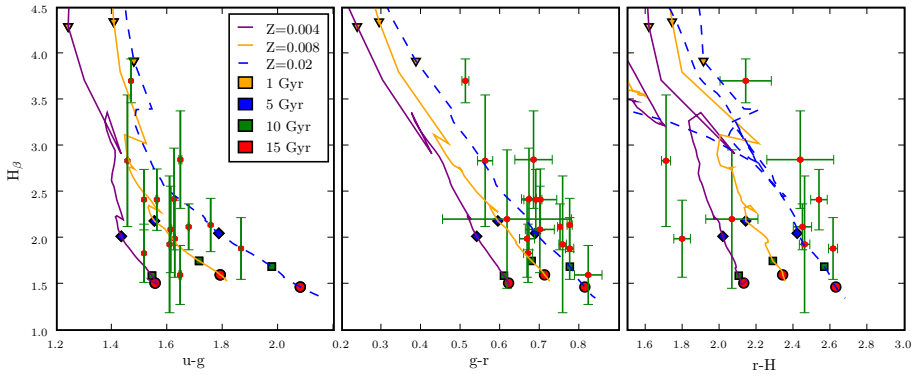

Figure 6.5. H$_\beta$ line vs colours diagram

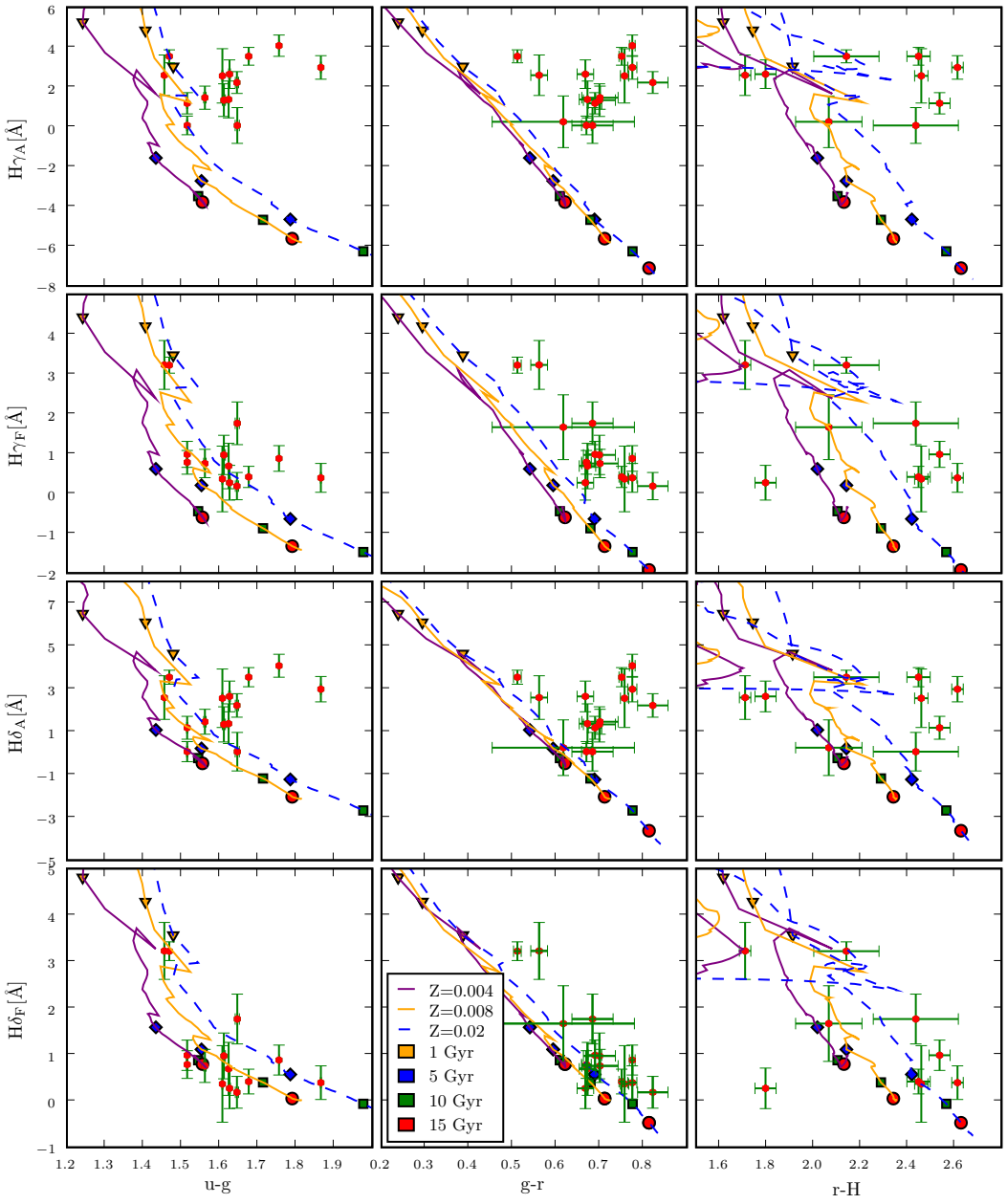

Figure 6.6. Hydrogen Lines vs colours diagram

6.2.2 <Fe>, [MgFe], Mgb vs Colours

Next to the Hydrogen series, the most metallicity-sensitive Lick/IDS indices are Mgb, Fe5270, Fe5335 and they are usually combined as:

$$< \text{Fe} >= (\text{Fe5270} + \text{Fe5335})/2 \tag{6.1}$$

$$[\text{MgFe}] = \sqrt{\text{Mg}b \times < \text{Fe} >} \tag{6.2}$$

The Mgb index traces the metallicity as given by the α elements, whereas $<$ Fe $>$ is most sensitive to Fe. The [MgFe] index tries to minimize the effect of the non-solar abundance ratios especially Mg-enhancement exhibited by normal Ellipticals [Thomas et al., 2003]. In Fig. 6.7 the errorbars from the indices are quite big and that makes it hard for interpretation. We can still confirm that the metallicities are around solar and sub-solar values. Giant ellipticals generally have above solar metallicities. As a result of having supersolar metallicity, in normal giant elliptical systems, measured Mgb values would fall outside these plotted regions.

The Mgb index traces the metallicity as given by the α elements, whereas $<$ Fe $>$ is most sensitive to Fe. The [MgFe] index tries to minimize the effect of the non-solar abundance ratios, especially the Mg-enhancement exhibited by normal Ellipticals [Thomas et al., 2003]. In Fig. 6.7 the errorbars from the indices are quite big and that makes it hard for interpretation. We can still confirm that the metallicities are around solar and sub-solar values. Giant ellipticals generally have above solar metallicities. As a result of having supersolar metallicity, in normal giant elliptical systems, measured Mgb values would fall outside these plotted regions.

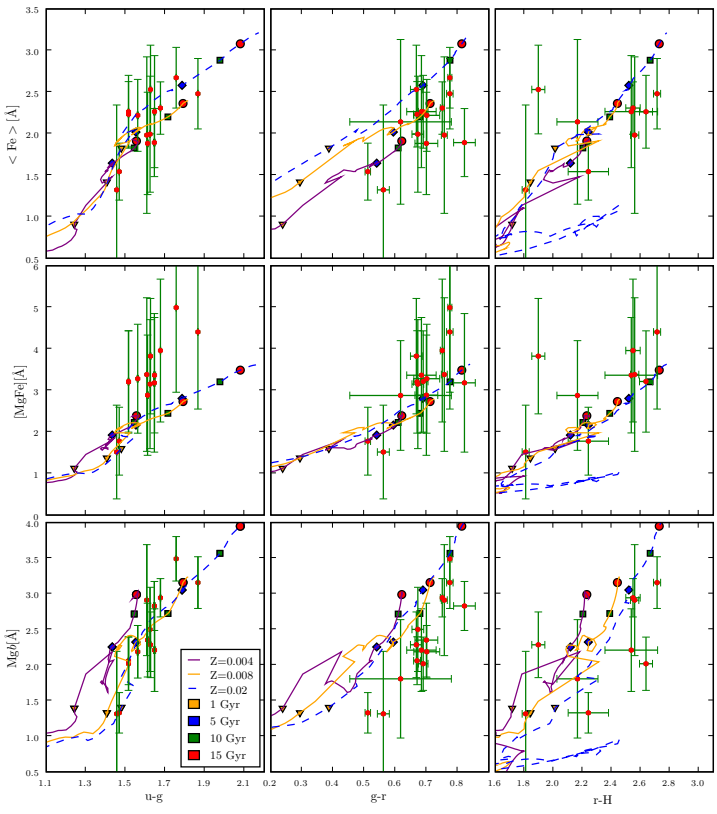

Figure 6.7. Iron and Magnesium lines vs colours diagram

CHAPTER 7

Results: Colour Gradients

7.1 Optical - Near-IR Colour Gradients

As shown in the individual surface brightness profiles of Appendix (A), many of the dwarf elliptical galaxies have slight colour gradients. Due to the seeing effects, we convolved our sample the frame in the passband with the best seeing with a Gaussian to match the seeing of the worst one. Therefore we cut the tables at 2 times the seeing from the center, so we do not have much information from the centre region. Positive colour gradients are seen in VCC1912, ID0615, ID0028, which shows that the outer regions are redder than the inner regions [Barazza et al., 2003]. However, the rest of the galaxies show negative gradients so that their inner regions are redder than the outer regions which agrees with the sample of van Zee et al. [2004].

When there is a colour gradient present it is harder to define the global colour of a galaxy. Colour gradients indirectly suggest a difference between the star formation history or the metallicity of the inner and outer regions of a galaxy. It is possible that both of these effects are relevant to the interpretation of observed colours and stellar populations of dwarf ellipticals. According to a theory suggested by van Zee et al. [2004], for cluster dwarfs, a galaxy may develop a colour gradient if the outer gas is stripped off as it falls into the Cluster. Then the inner region of the galaxy may continue to have star formation, while the outer regions have aging stellar populations and in effect becoming redder. Such a scenario explains the observed colour gradients in dwarf elliptical galaxies which are redder in the outer parts.

In our research we found the average gradients from our sample as;
$\nabla(g-r) = -0.011 \pm 0.016$, $\nabla(r-z) = -0.032 \pm 0.047$,
$\nabla(u-r) = -0.030 \pm 0.249$, $\nabla(g-H) = -0.031 \pm 0.066$,
$\nabla(r-H) = -0.050 \pm 0.079$, $\nabla(H-K) = -0.031 \pm 0.085$.

The averages clearly indicates that dwarf ellipticals have negative gradients in all colours. From that we can infer that most of the dwarf ellipticals are redder in the inner part and slightly bluer towards the edges. Such a situation may be possible if the inner region is more enriched than the outer parts; so if there is a metallicity gradient, the more metal-rich stars in the inner regions will be redder than the metal-poor stars at the outskirts. A more basic answer could be that there is more star formation happening at the outer parts compared to the inner. The relative importance of both of these effects will depend on the galaxy's detailed star formation history and the interference of the galaxy with the intracluster

medium. This last scenario is not very likely, since very little star formation is found in these dwarf ellipticals.

In the $\nabla(g-r)$ vs colour diagrams in Fig. 7.1, three galaxies have an interesting position in the $\nabla(g-r)$ vs $r-H$ and $g-H$ diagrams. ID0650 and ID1524 have positive gradients and VCC0817 has a negative gradient while having a quite blue colour. Almost all of the other galaxies show expected negative gradients in the other colours as well.

In the $\nabla(r-H)$ vs. colour diagrams, it appears that only three galaxies have positive gradients while in $\nabla(r-z)$ diagrams this number is five. The diagrams in Fig. 7.1, 7.2 and 7.3 also confirms that the majority of dwarf galaxies have a negative gradient.

Our sample is usually very faint in the u band and some galaxies are even invisible in the images. Therefore there is a lot of scatter in the u band gradients. In the $\nabla(u-r)$ vs colours diagrams in Fig 7.4, there appears a lot of positive gradients which does not appear in other gradient diagrams. Thus, this diagram could not be realistic for interpretation.

In the gradients vs gradient diagrams in Fig. 7.6, we seperated the Virgo Cluster and field dwarfs. It can be seen that there is a low number of positive gradients at the plots. Besides, we can see that the environment does not affect the gradients since field dwarfs (green dots) and Virgo Cluster dwarfs (red dots) scattered randomly through the diagrams.

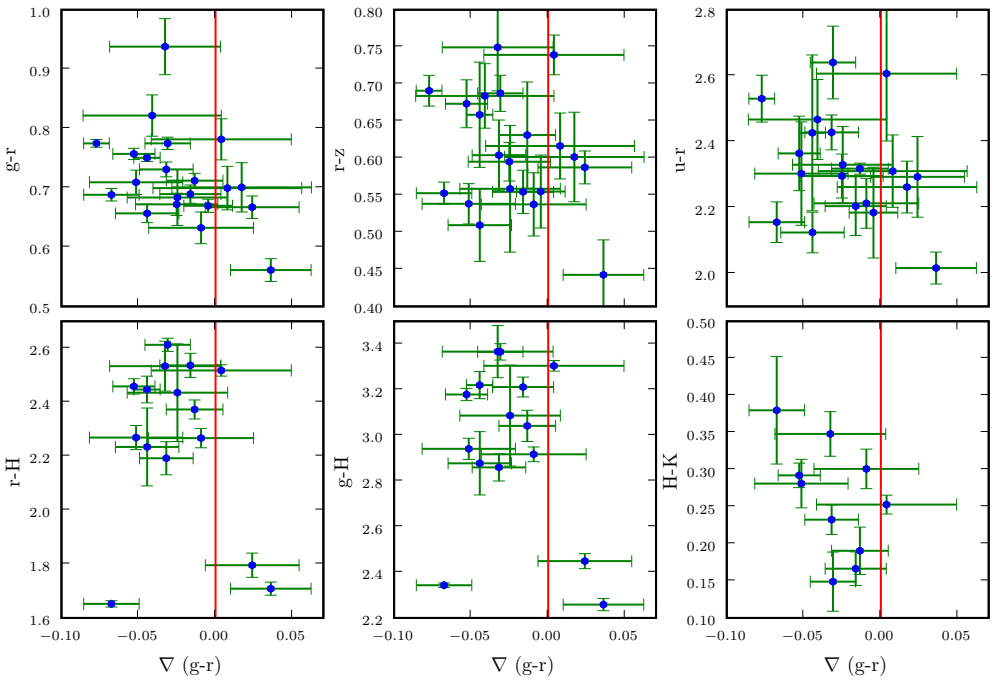

Figure 7.1. ∇ (g-r) vs all colours diagram.

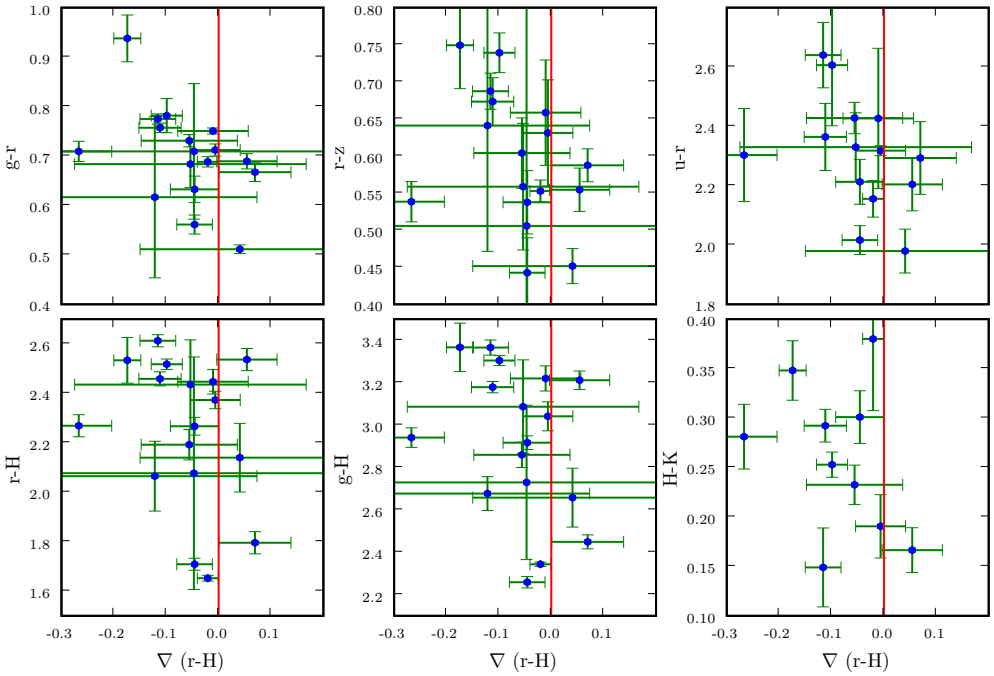

Figure 7.2. ∇ (r-H) vs all colours diagram.

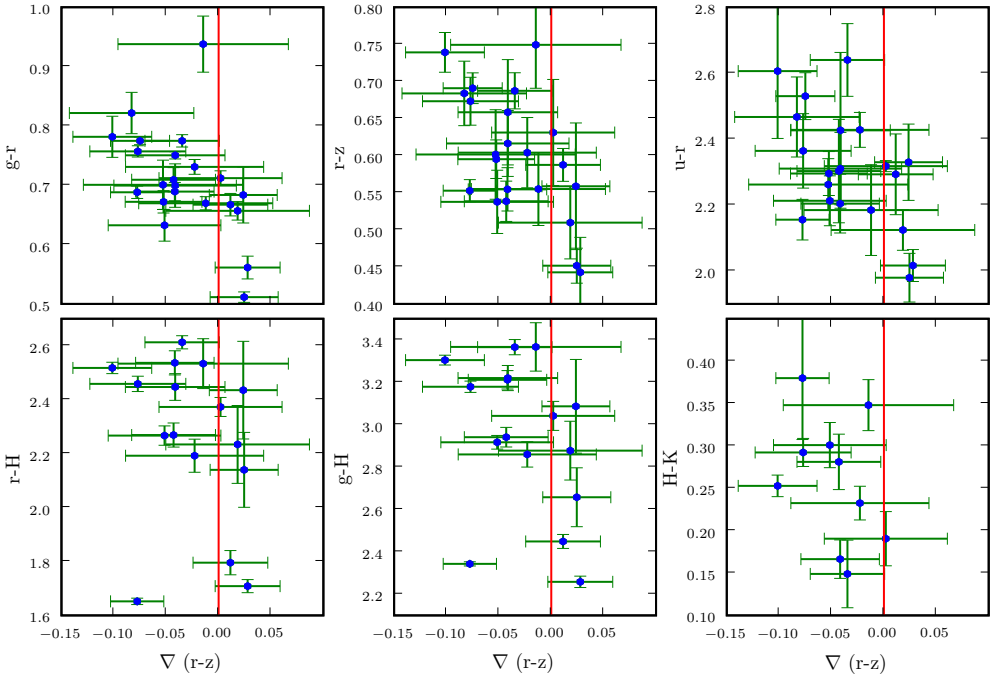

Figure 7.3. ∇ (r-z) vs all colours diagram.

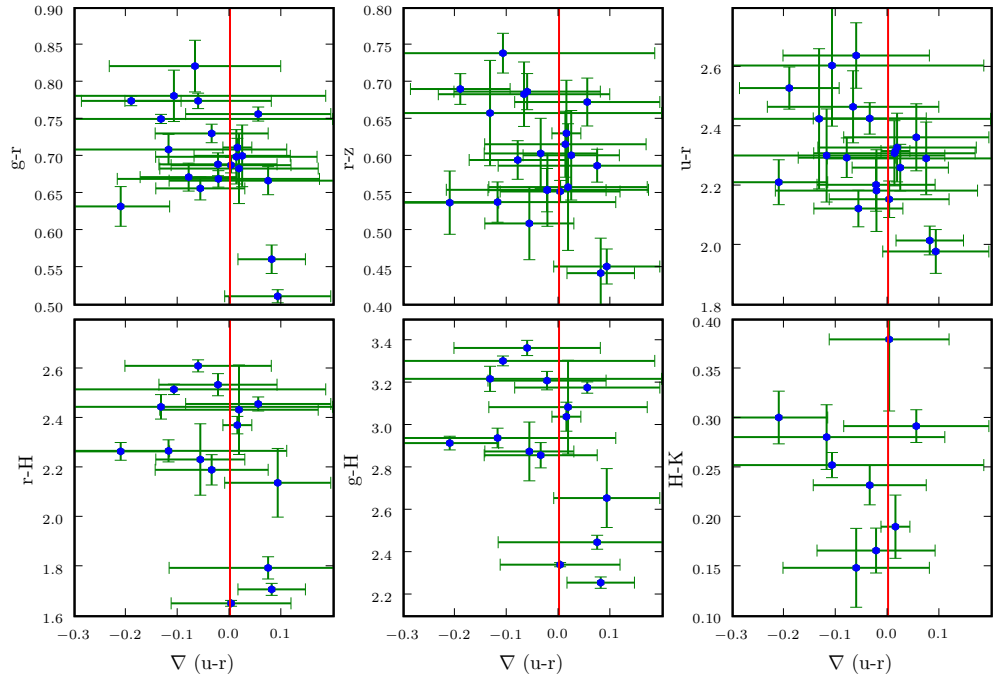

Figure 7.4. ∇ (u-r) vs all colours diagram.

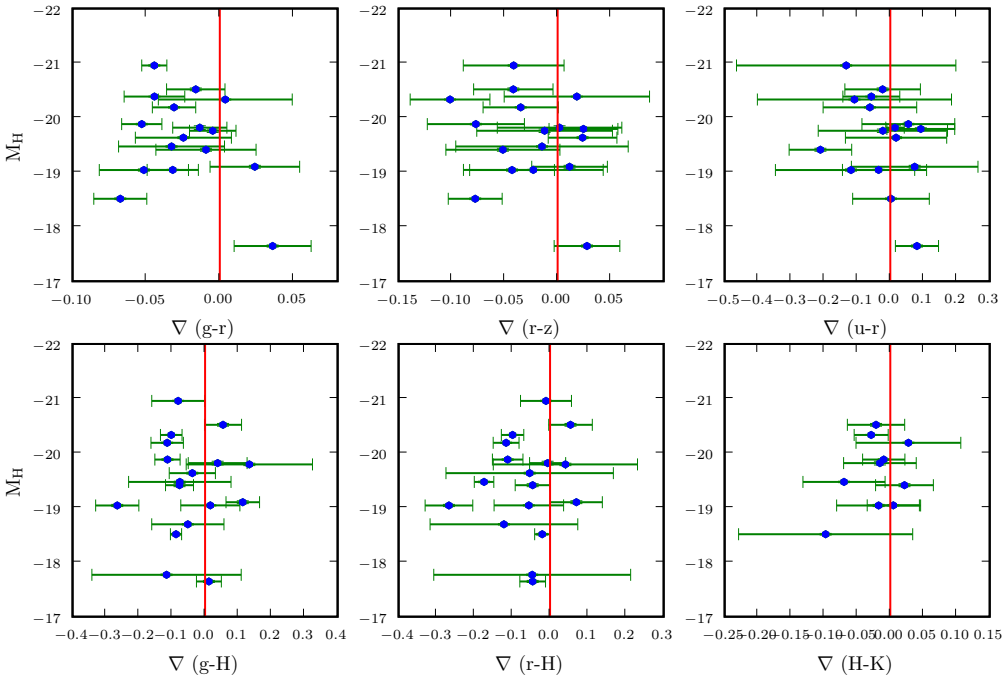

Figure 7.5. Gradients vs M_H diagram.

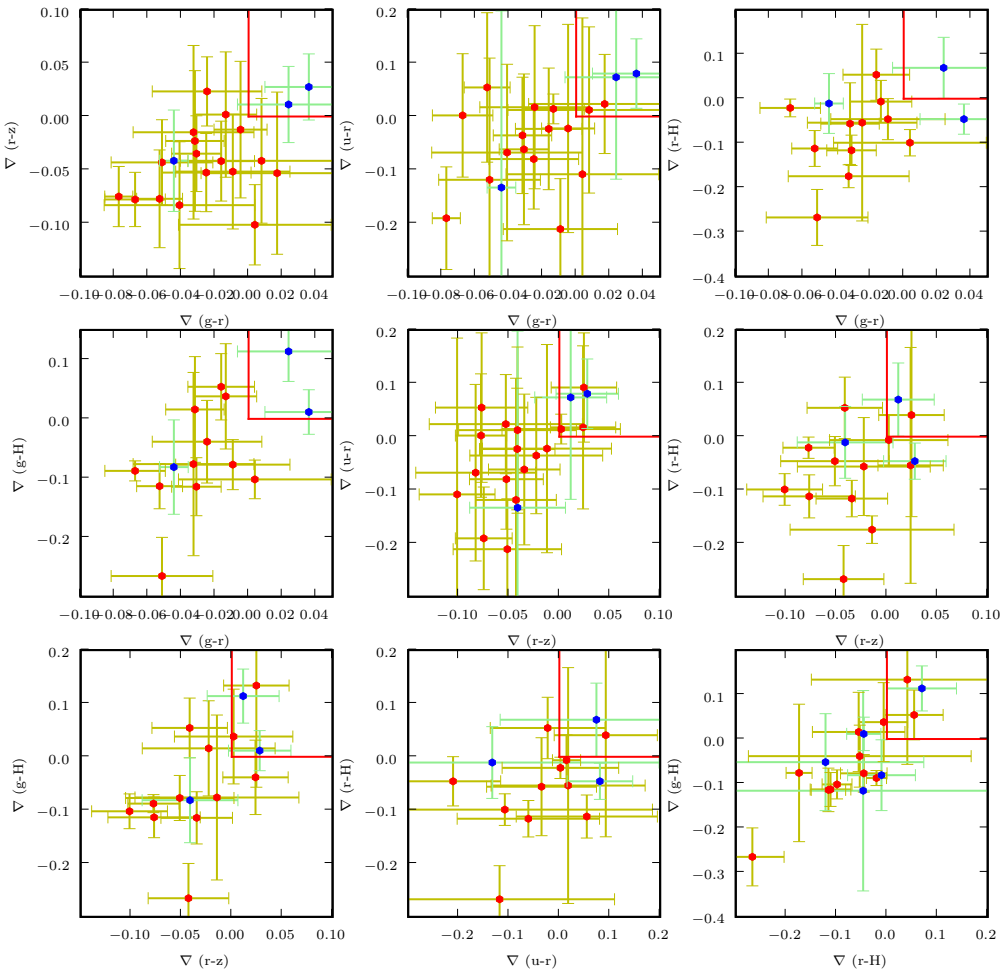

Figure 7.6. Gradients vs gradients diagram. Red dots are dwarfs from Virgo Cluster and green dots are from field.

CHAPTER 8

Discussion and Conclusions

In this research we have presented surface photometry of near-IR and optical images of 33 dwarf elliptical galaxies in the Virgo Cluster and in the field. The Magpop-ITP research is the first study of dwarf ellipticals which includes a detailed investigation of field systems. It is difficult to find low-mass non-star-forming dwarfs in the field. Except for ID0872, which is quite a faint dE, the field sample has similar blue magnitudes as the Virgo dEs thus we study similar mass ranges. Out of 33 dwarf ellipticals 11 are field and 22 are Virgo Cluster members. Besides we also have the observation of star-forming dwarfs, out of 20 star-forming dwarf 10 are field and 10 are from Virgo Cluster members.

The major results of these observations are as follows;

1) Star forming and quiescent dwarfs can be very well separated in the colour-magnitude and colour-colour diagrams. So the selection in FUV-NUV colour is quite good in separating these two types.

2) There appear no differences between field and cluster, both in the colour-colour and colour-magnitude diagrams. They show the same properties whether they are in a cluster system or in the field. It should be noted that using a more detailed investigation maybe a relation can be found between the properties of dwarf ellipticals and e.g., distance from the Cluster centre, etc.

One should note, however, that Michielsen et al. [2008] found that the field dwarf ellipticals are either more concentrated or less concentrated than the Virgo dwarf ellipticals. This is likely a result of the difficulty in finding dwarf ellipticals in the field. They used a statistical comparison of a one-dimensional Kolmogorov-Smirnov (KS) test which gives the probability ($P_{\rm KS}$) that the difference between two distributions would be as large as observed if they had been drawn from the same population. The importance of this test is that it even works for small samples. The structural parameters of concentration C, large scale asymmetry A and clumpiness S are three model-independent parameteres that can be used to quantify a galaxy's structural appearance [Conselice, 2003]. After the KS test, the probability that C follows the same distribution for field and Virgo dwarf ellipticals is only 1% ($P_{\rm KS}$=0.01), therefore the field and Virgo dwarf ellipticals have a significantly different distribution in concentration. Besides, the other parameters for A, $P_{\rm KS}$=0.52 and for S, $P_{\rm KS}$=0.13 shows that it is not possible to conclude that they are drawn from different distribution. As a conclusion, Michielsen et al. [2008] indicates that, for field dwarf ellipticals, there is no statistical evidence that the distribution in age, metallicity or

abundance ratio is different from the Virgo sample which also agrees with our result.

3) The global optical colours found are;

(g-r) = 0.693 ± 0.032, (r-z) = 0.582 ± 0.058,
(u-r) = 2.315 ± 0.105, (g-H) = 2.903 ± 0.086,
(r-H) = 2.221 ± 0.086, (H-K) = 0.273 ± 0.032

for comparison van Zee et al. [2004] presented their colours as

(U-B) = 0.24 ± 0.03, (B-V) = 0.77 ± 0.02, (B-R) = 1.26 ± 0.05,
(V-R) = 0.48 ± 0.01, (V-I) = 1.02 ± 0.03

when we do the conversion of Smith et al. [2002] from (V-R) to (g-r), we found 0.627 ± 0.017 which is comparable with our result. They only have optical colours though, so we can only compare at these bands.

According to all our colour-colour, colour-magnitude, colour-spectroscopic indices diagrams overlayed with Bruzual and Charlot [2003] Simple Stellar Population Models, we found that dwarf elliptical galaxies have around solar and sub-solar metallicity with an age range of 4-10 Gyrs.

4) The average gradients found are;
$\nabla(g-r) = -0.011 \pm 0.016$, $\nabla(r-z) = -0.032 \pm 0.047$,
$\nabla(u-r) = -0.030 \pm 0.249$, $\nabla(g-H) = -0.031 \pm 0.066$,
$\nabla(r-H) = -0.050 \pm 0.079$, $\nabla(H-K) = -0.031 \pm 0.085$
As a final result, we can deduce from the average gradients that dwarf ellipticals have negative gradients in all colours. From that we can infer that most of the dwarf ellipticals are redder at the inner part and slightly bluer to the edges. The most likely explanation, consistent with giant ellipticals, is that they generally have a small metallicity gradient.

APPENDICES

APPENDIX A

A.1 Surface Photometry Results

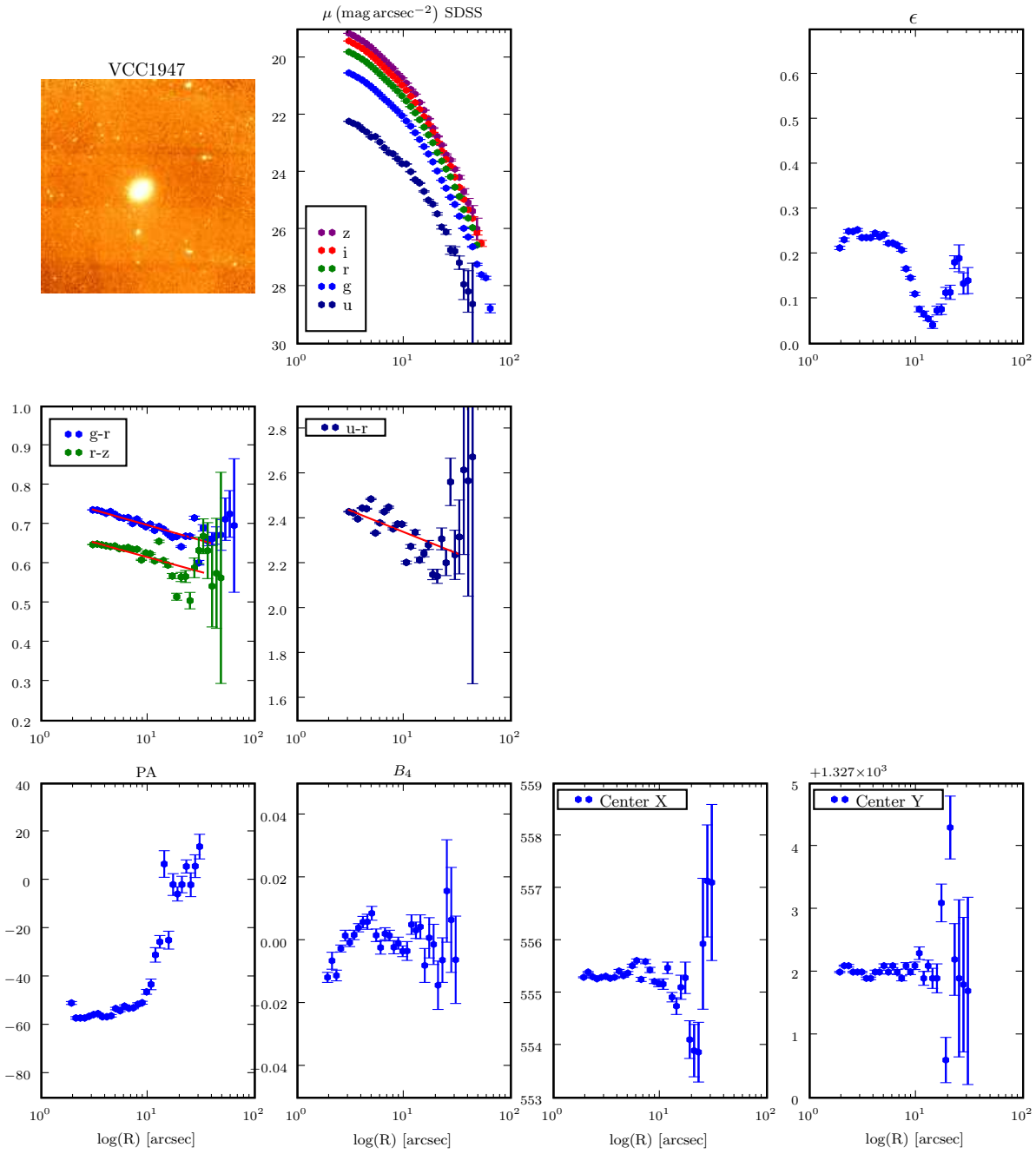

Figure A.1. VCC1947 Surface Photometry Results

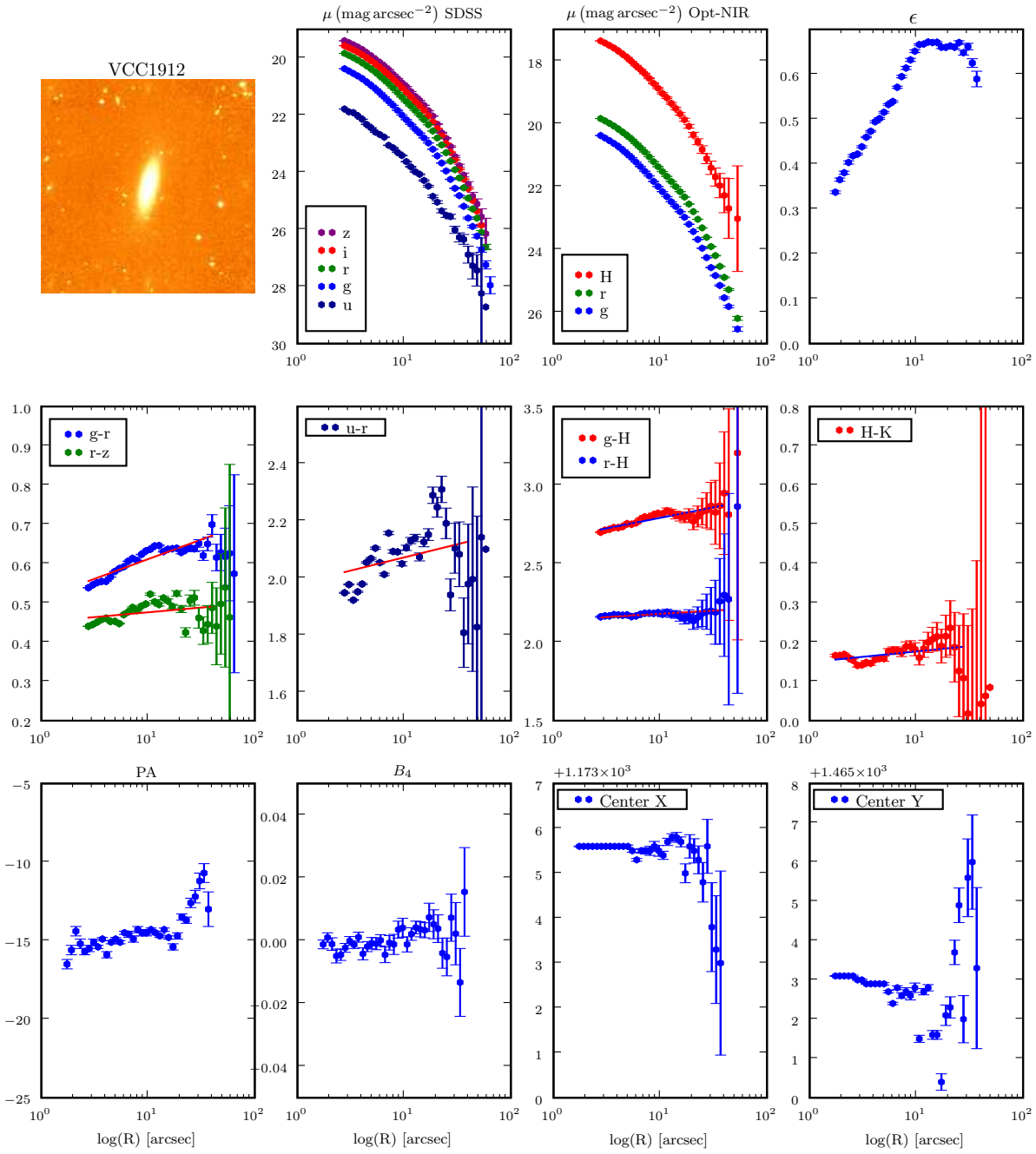

Figure A.2. VCC1912 Surface Photometry Results

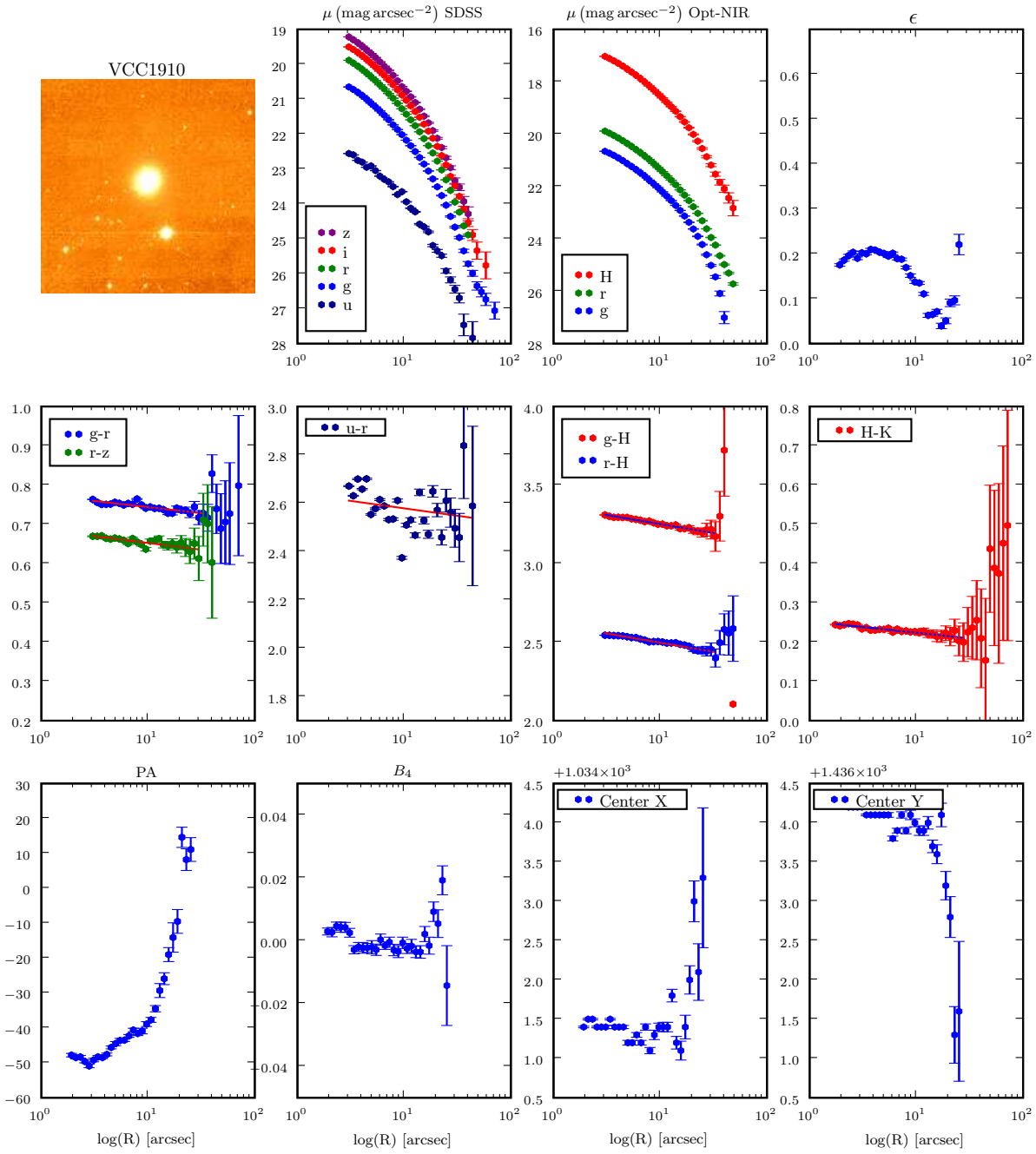

Figure A.3. VCC1910 Surface Photometry Results

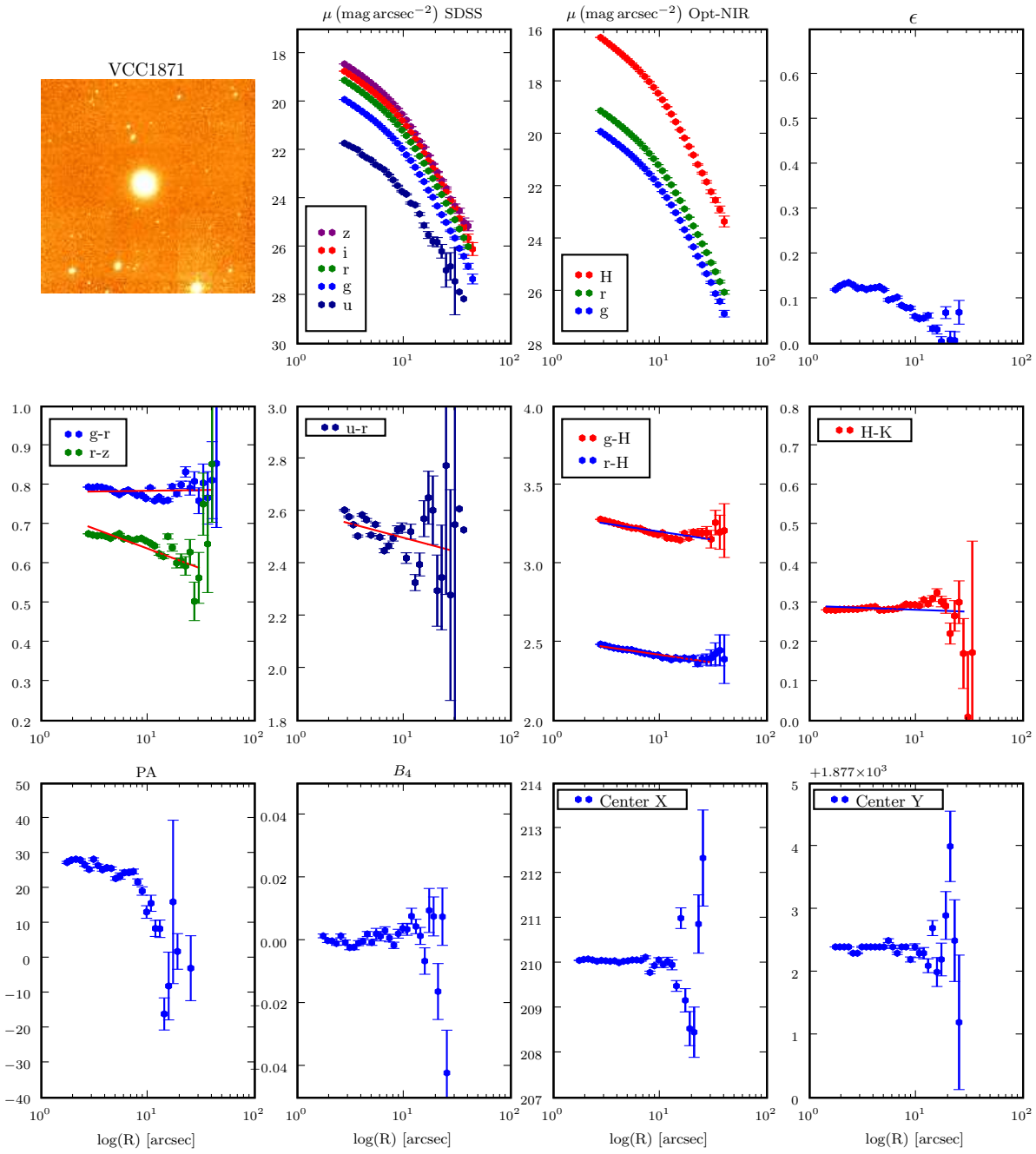

Figure A.4. VCC1871 Surface Photometry Results

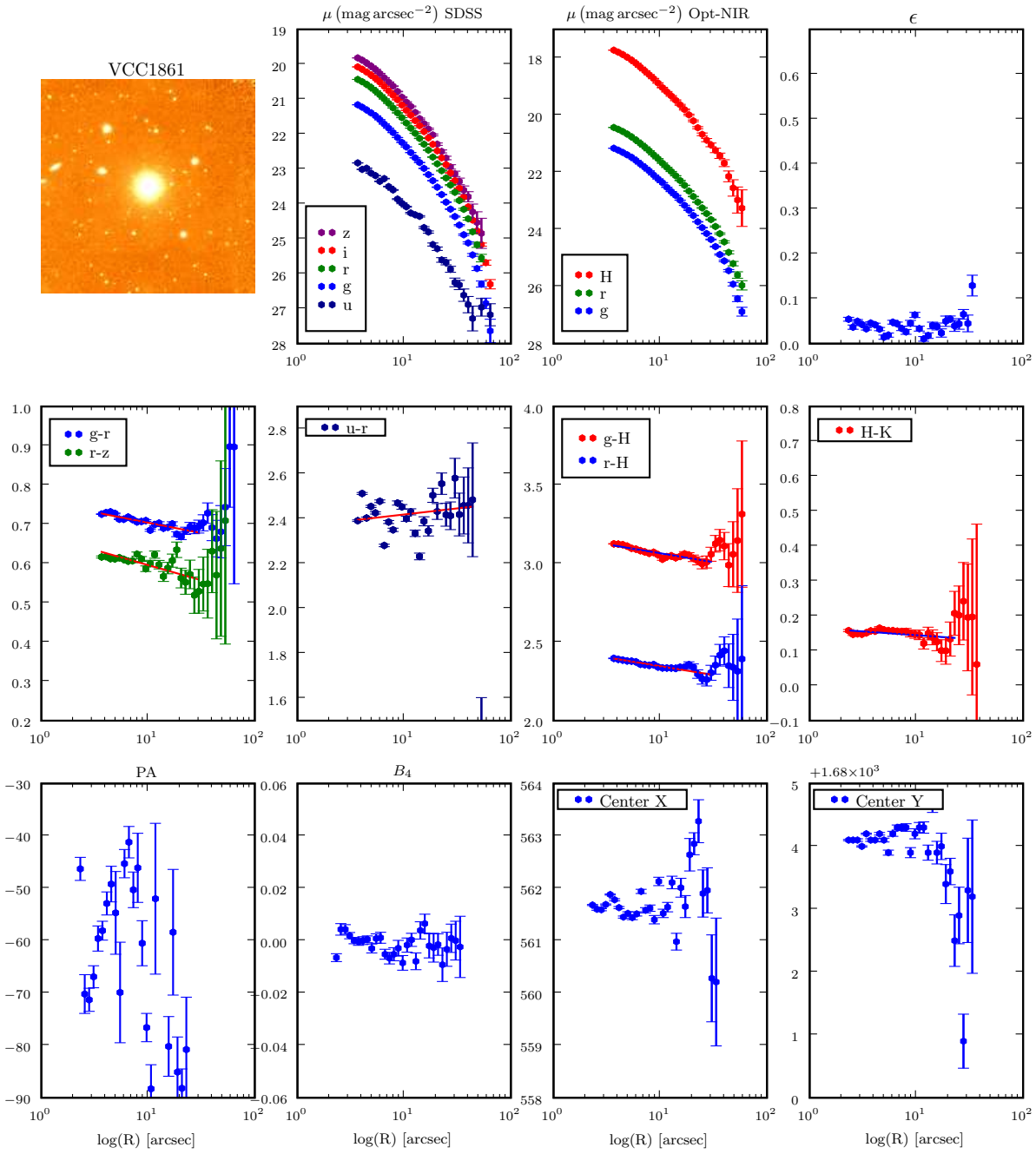

Figure A.5. VCC1861 Surface Photometry Results

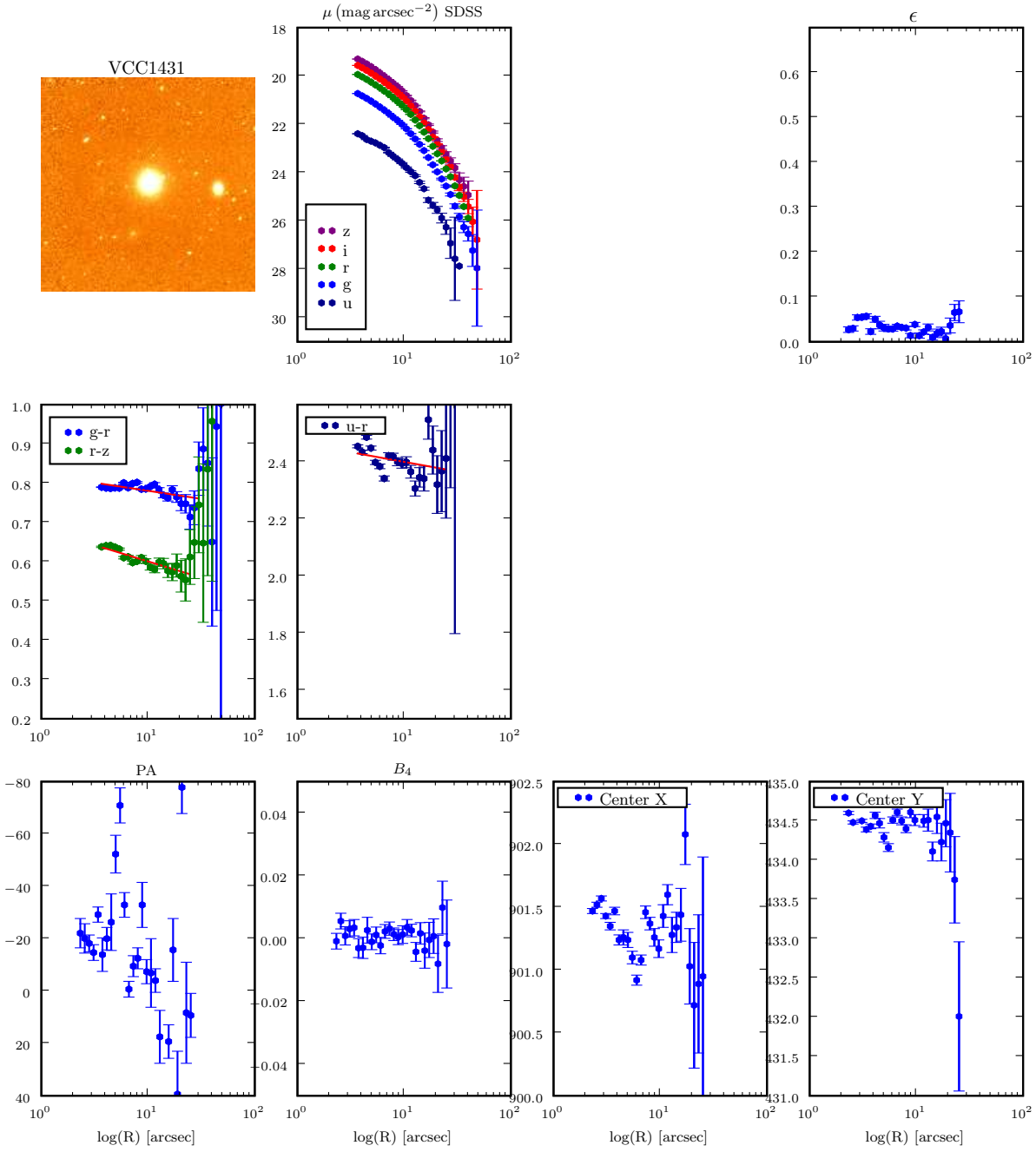

Figure A.6. VCC1431 Surface Photometry Results

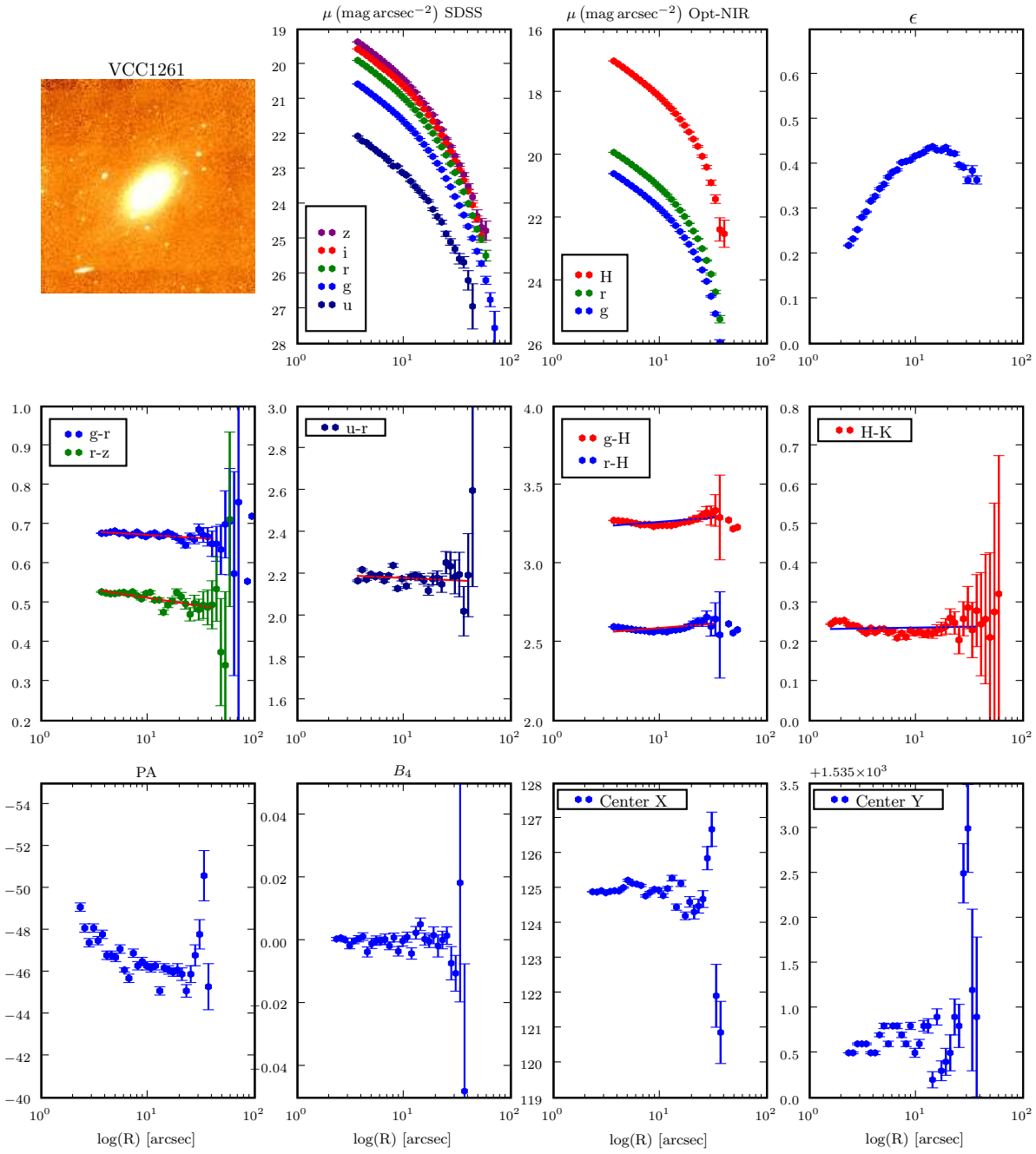

Figure A.7. VCC1261 Surface Photometry Results

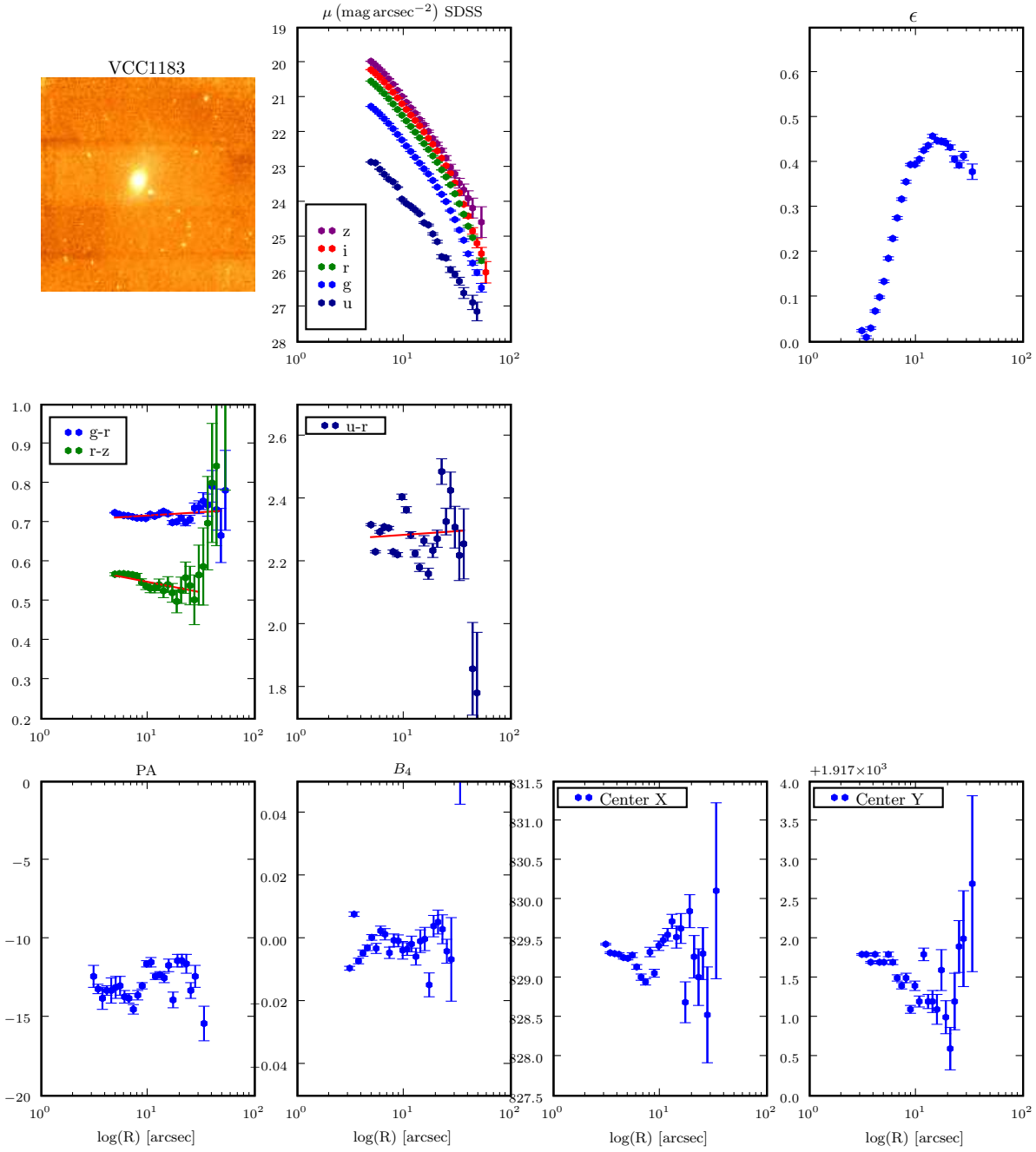

Figure A.8. VCC1183 Surface Photometry Results

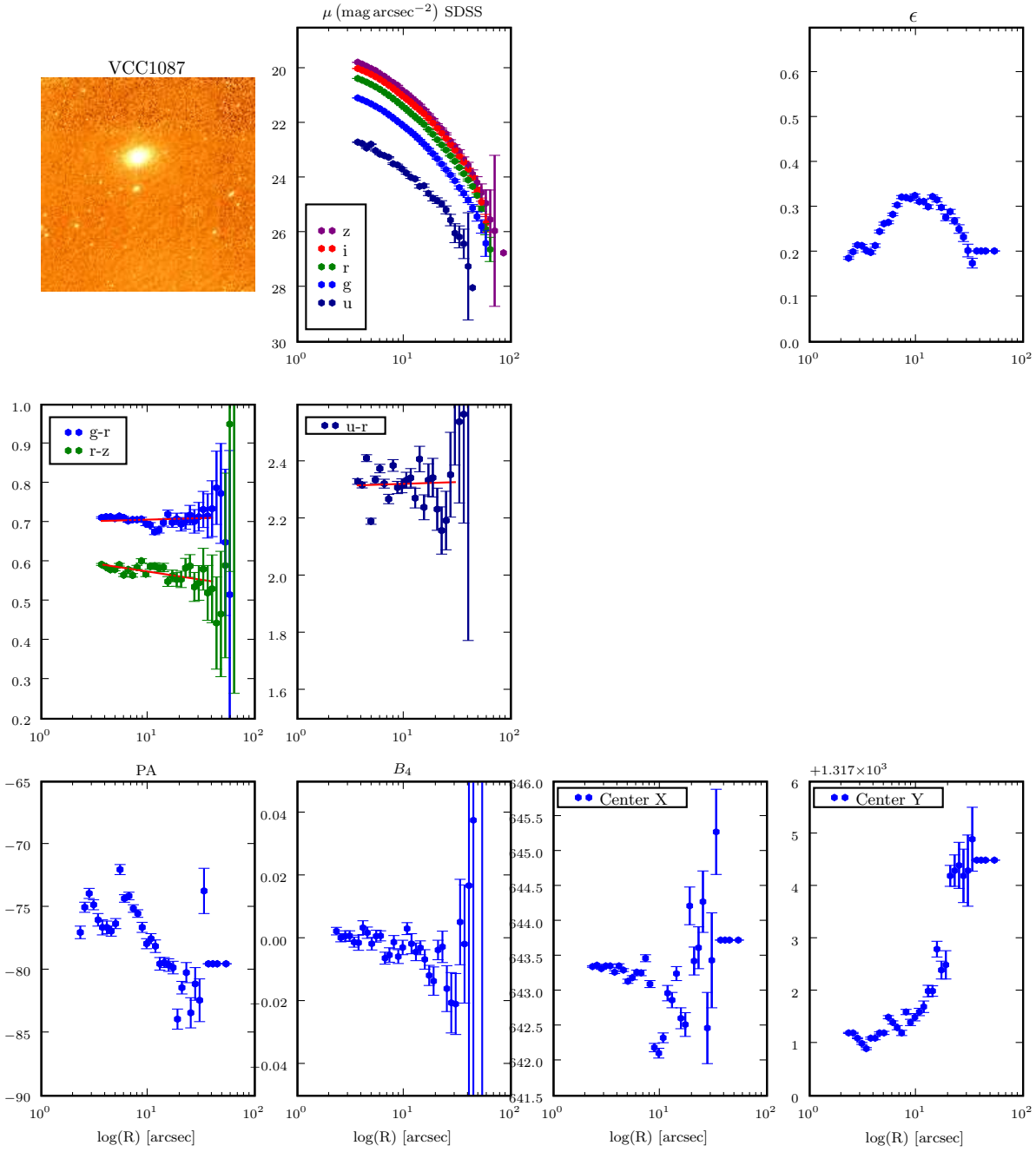

Figure A.9. VCC1087 Surface Photometry Results

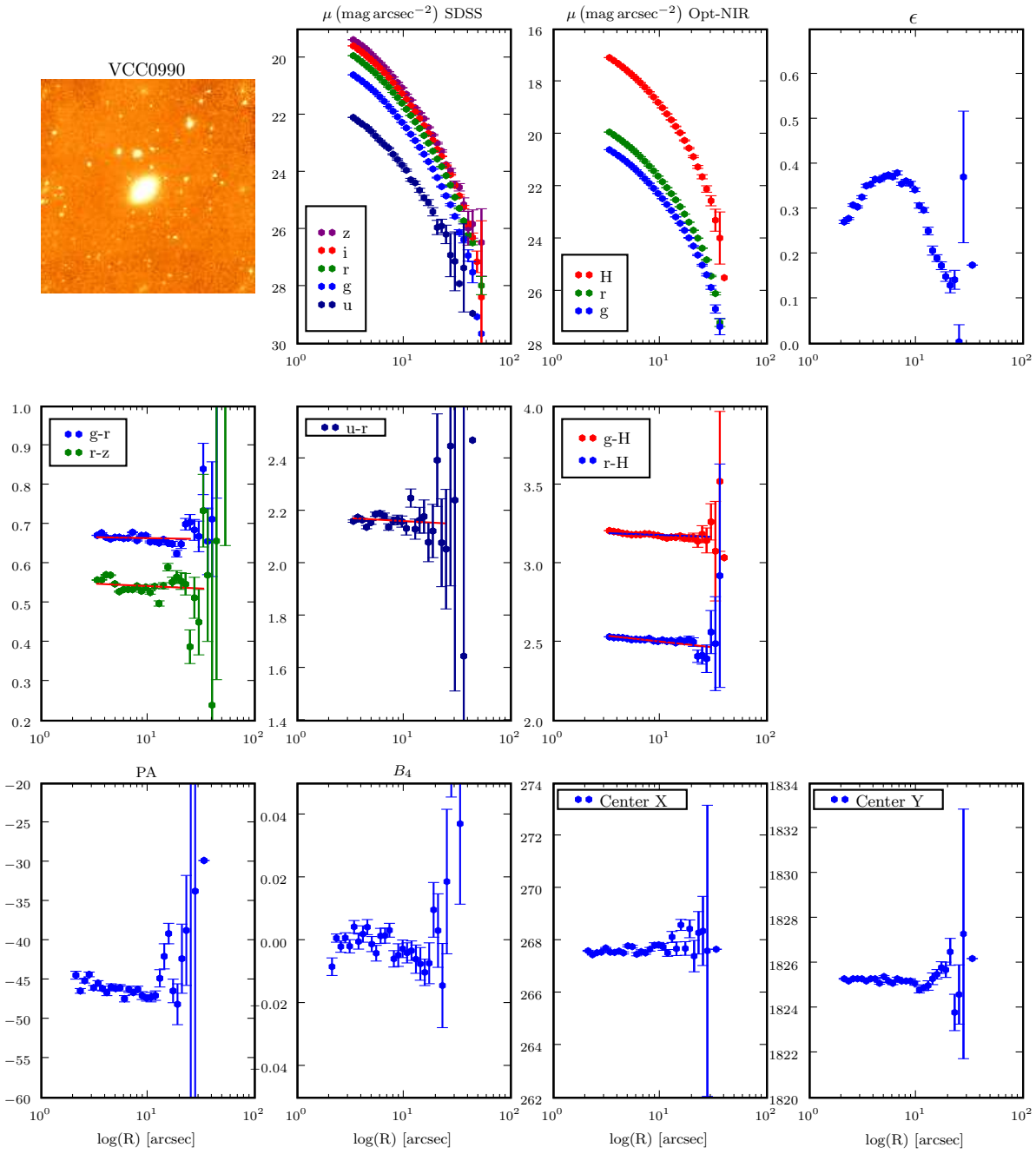

Figure A.10. VCC0990 Surface Photometry Results

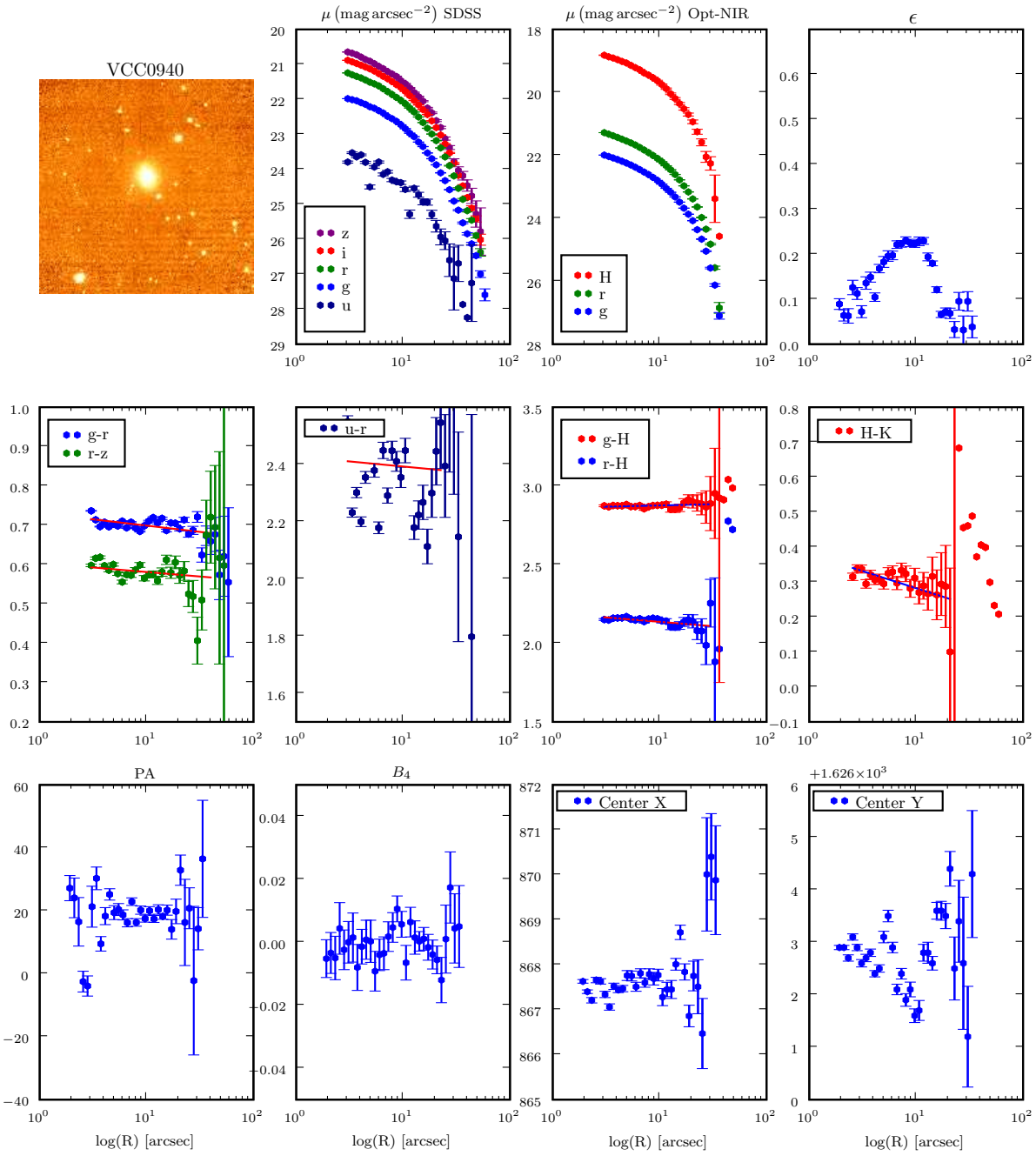

Figure A.11. VCC0940 Surface Photometry Results

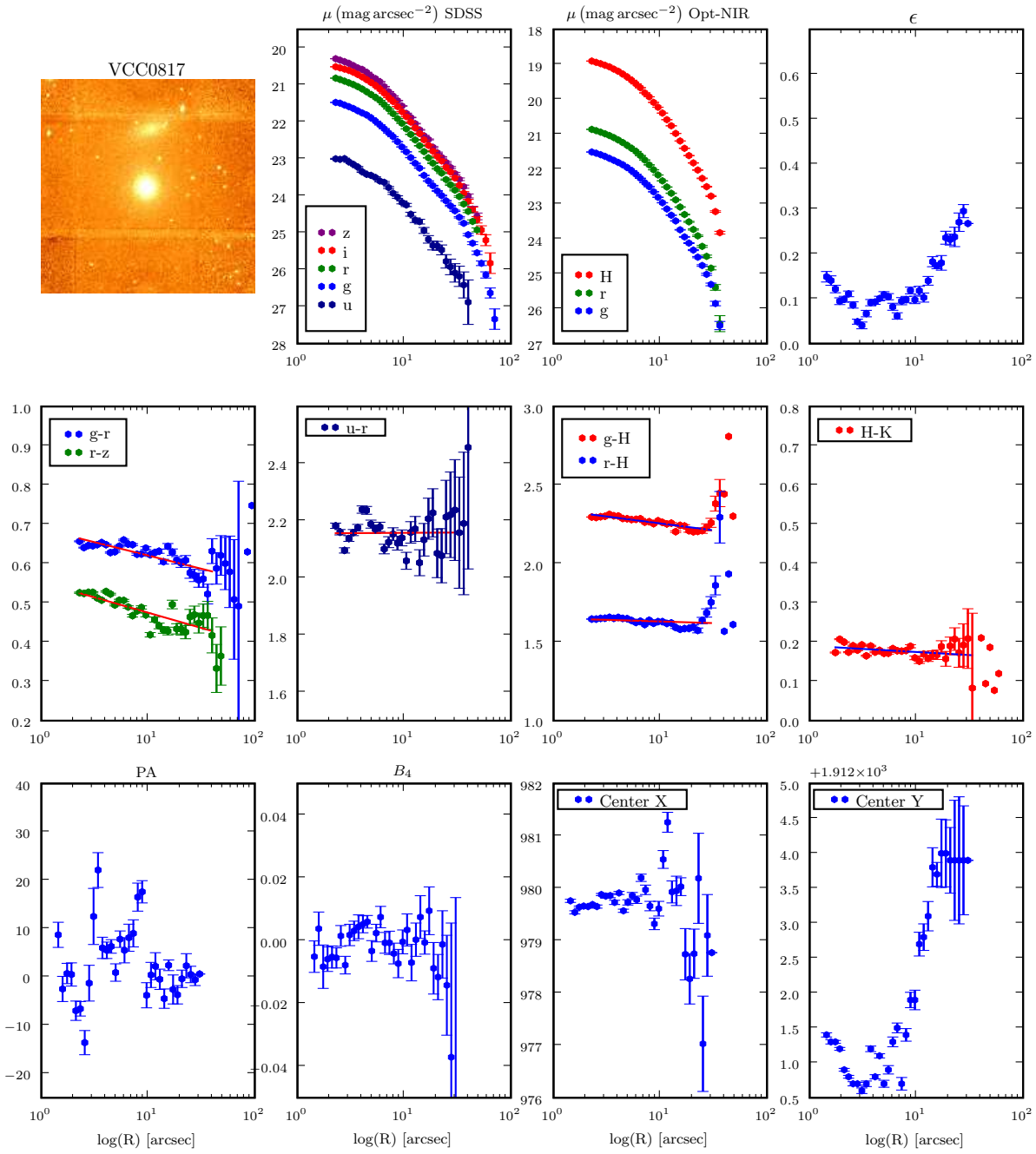

Figure A.12. VCC0817 Surface Photometry Results

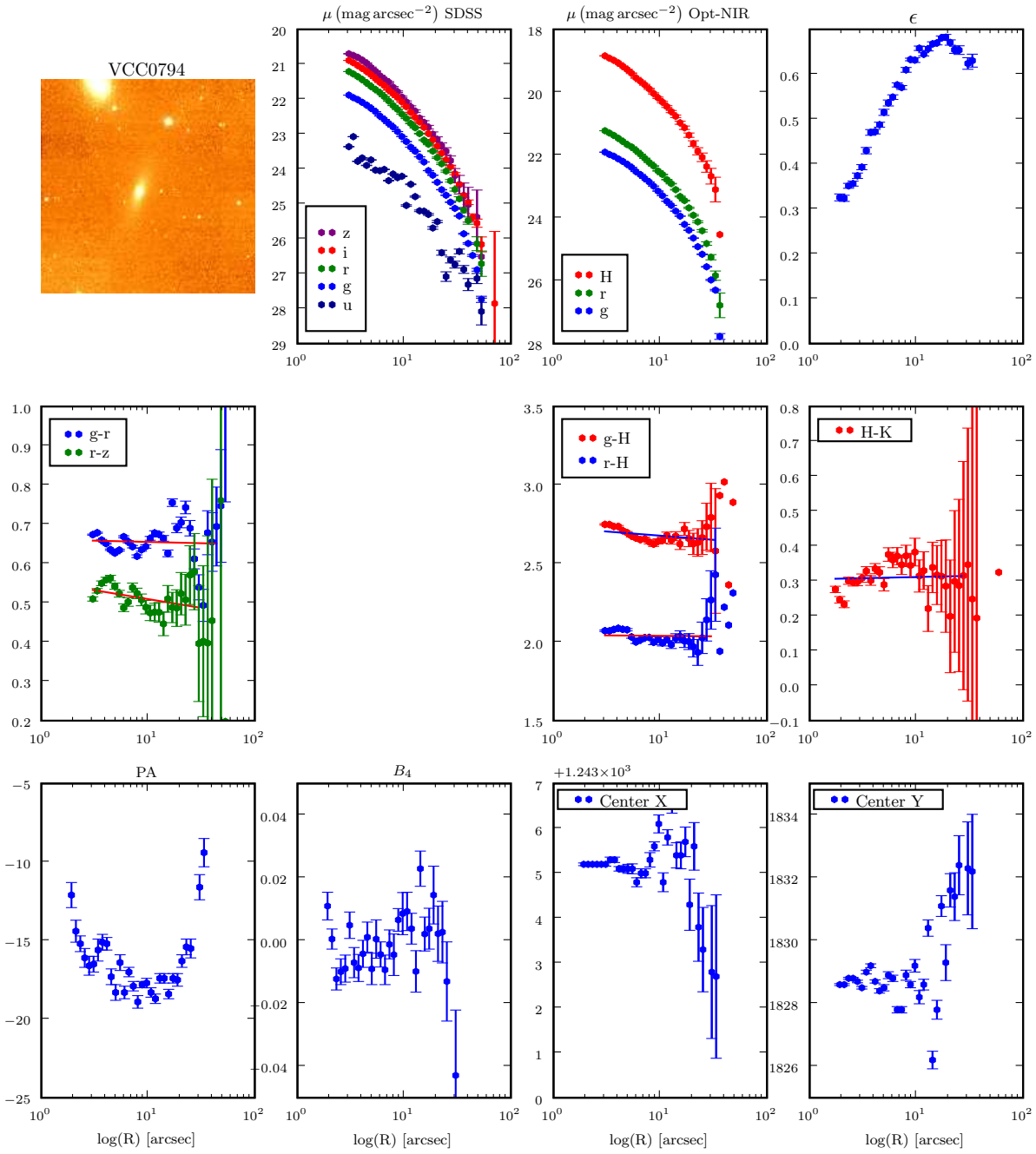

Figure A.13. VCC0794 Surface Photometry Results

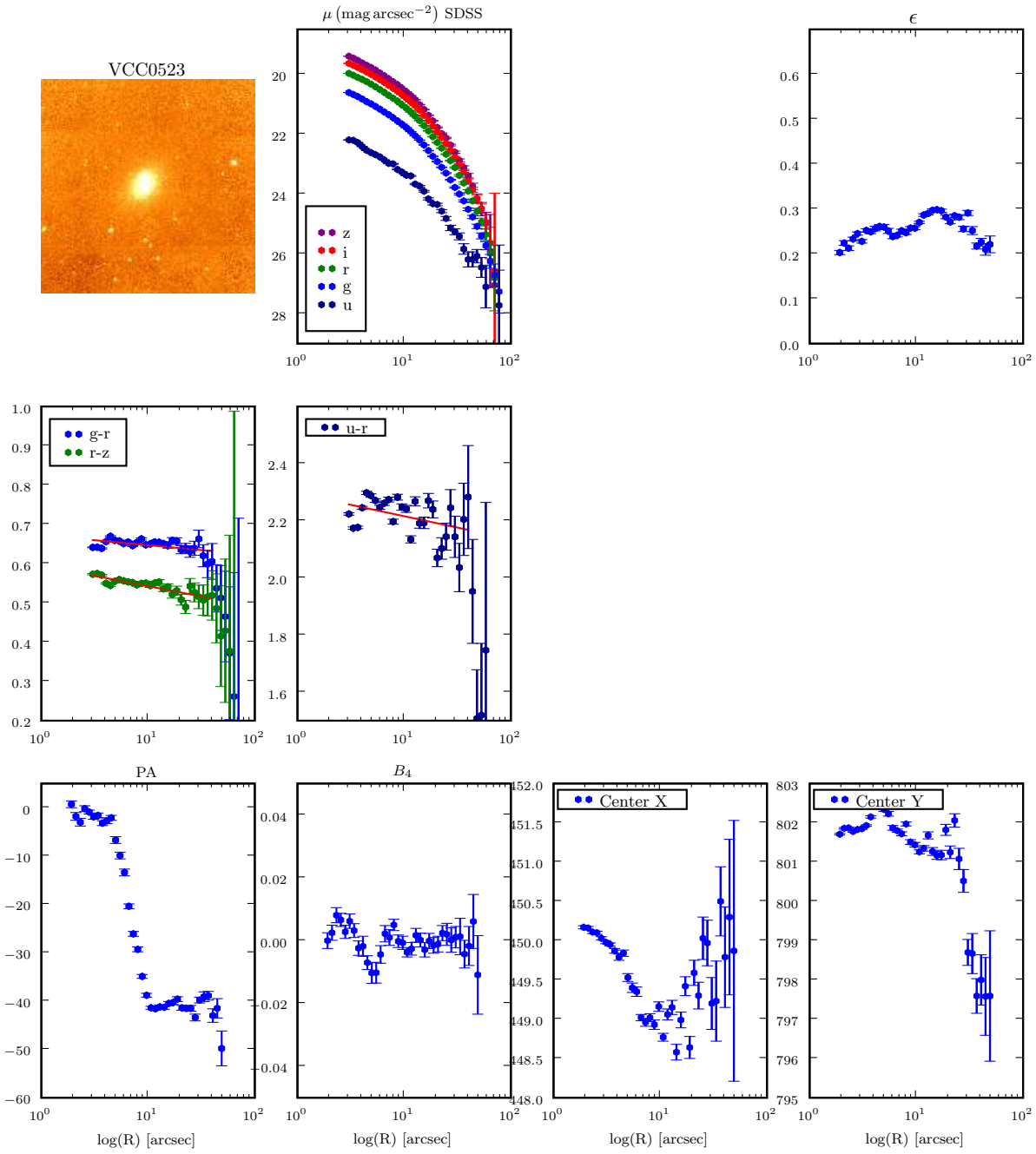

Figure A.14. VCC0523 Surface Photometry Results

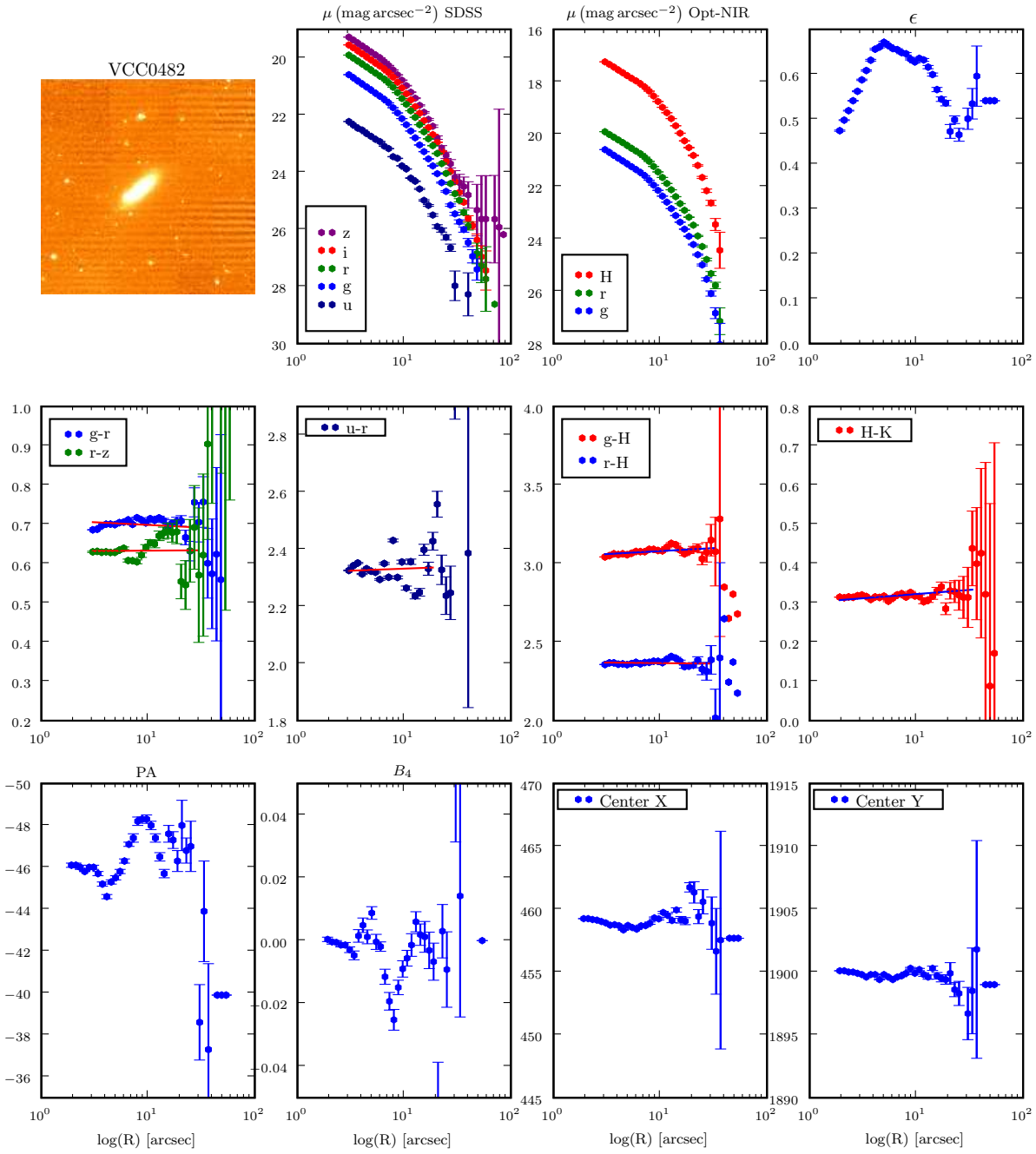

Figure A.15. VCC0482 Surface Photometry Results

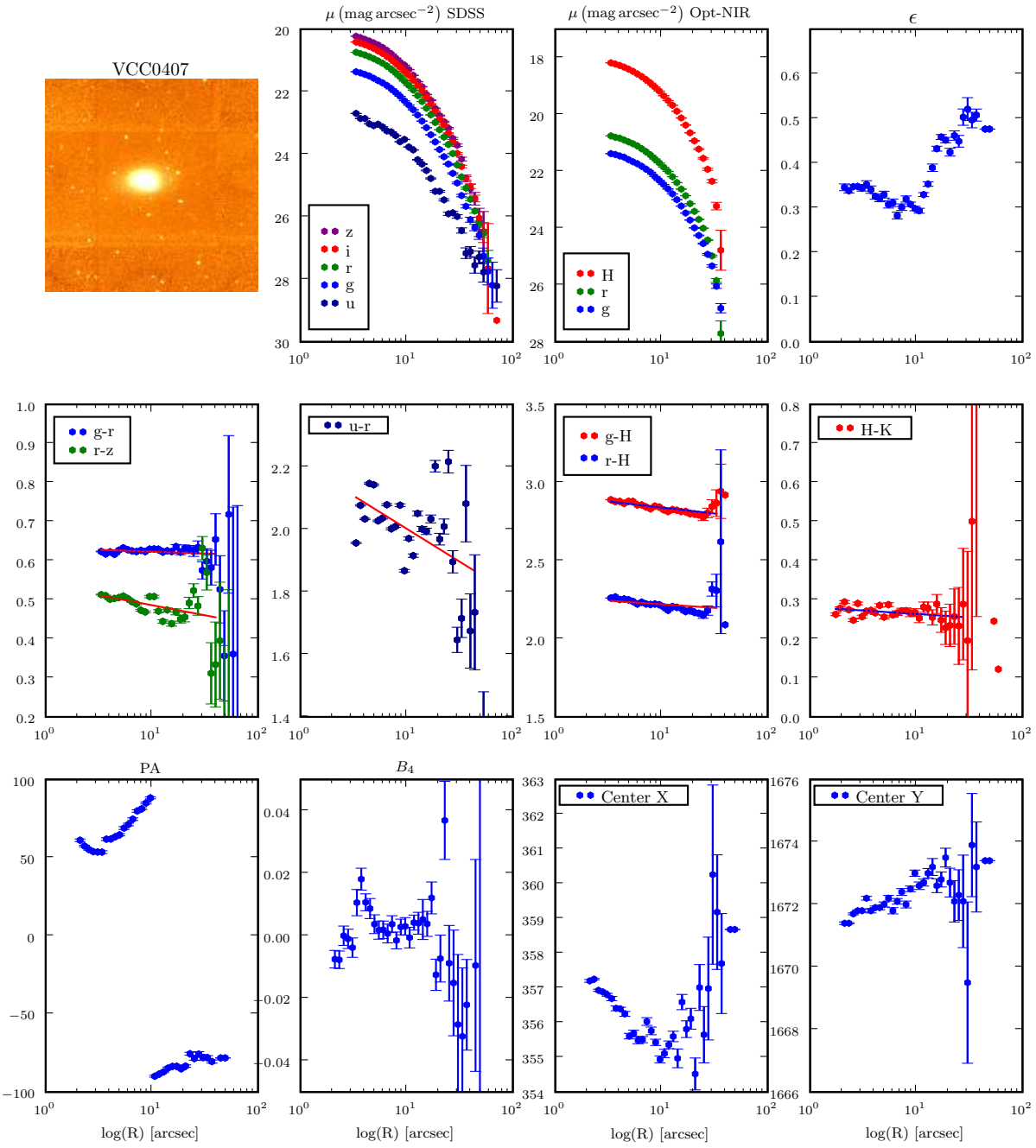

Figure A.16. VCC0407 Surface Photometry Results

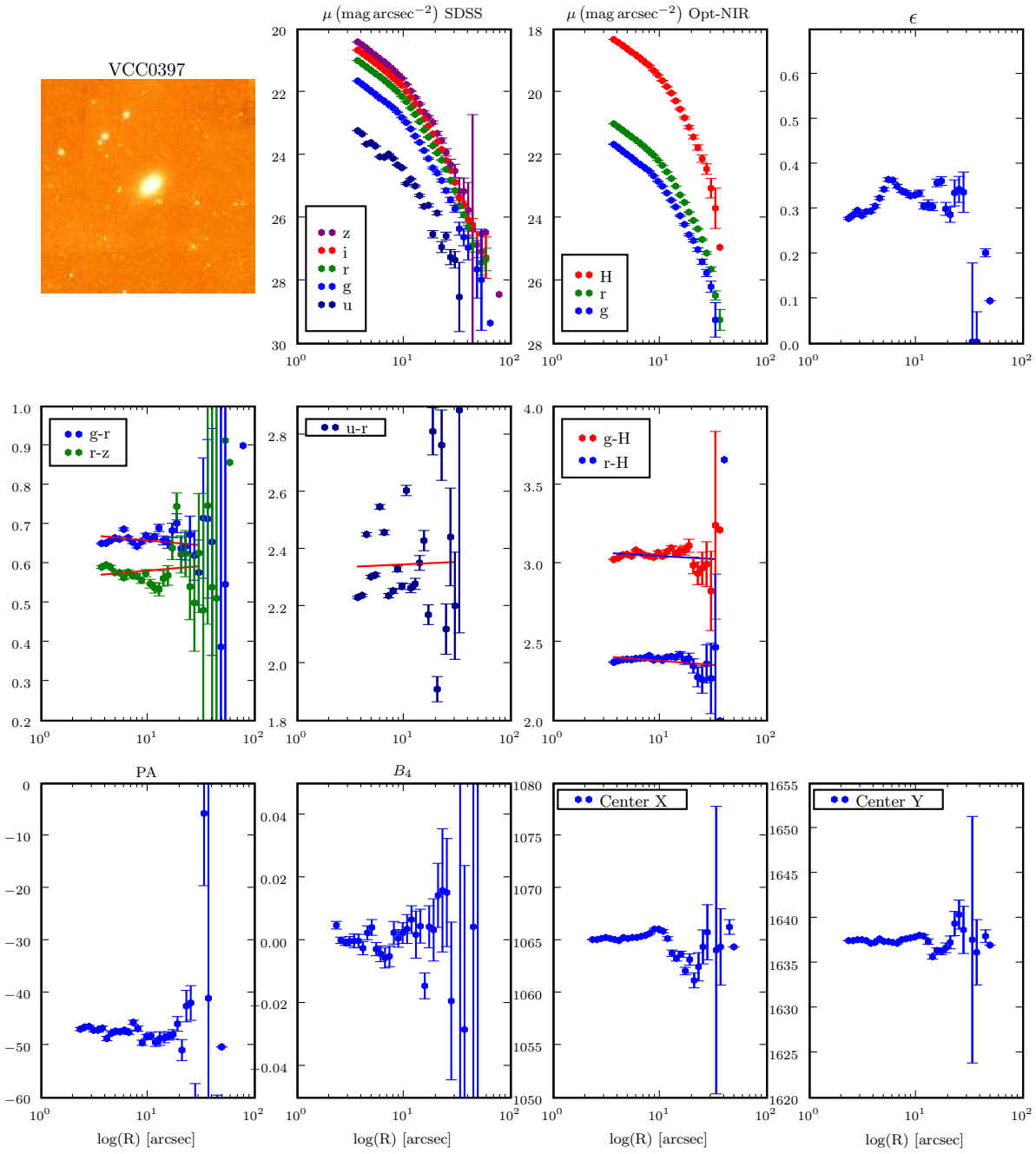

Figure A.17. VCC0397 Surface Photometry Results

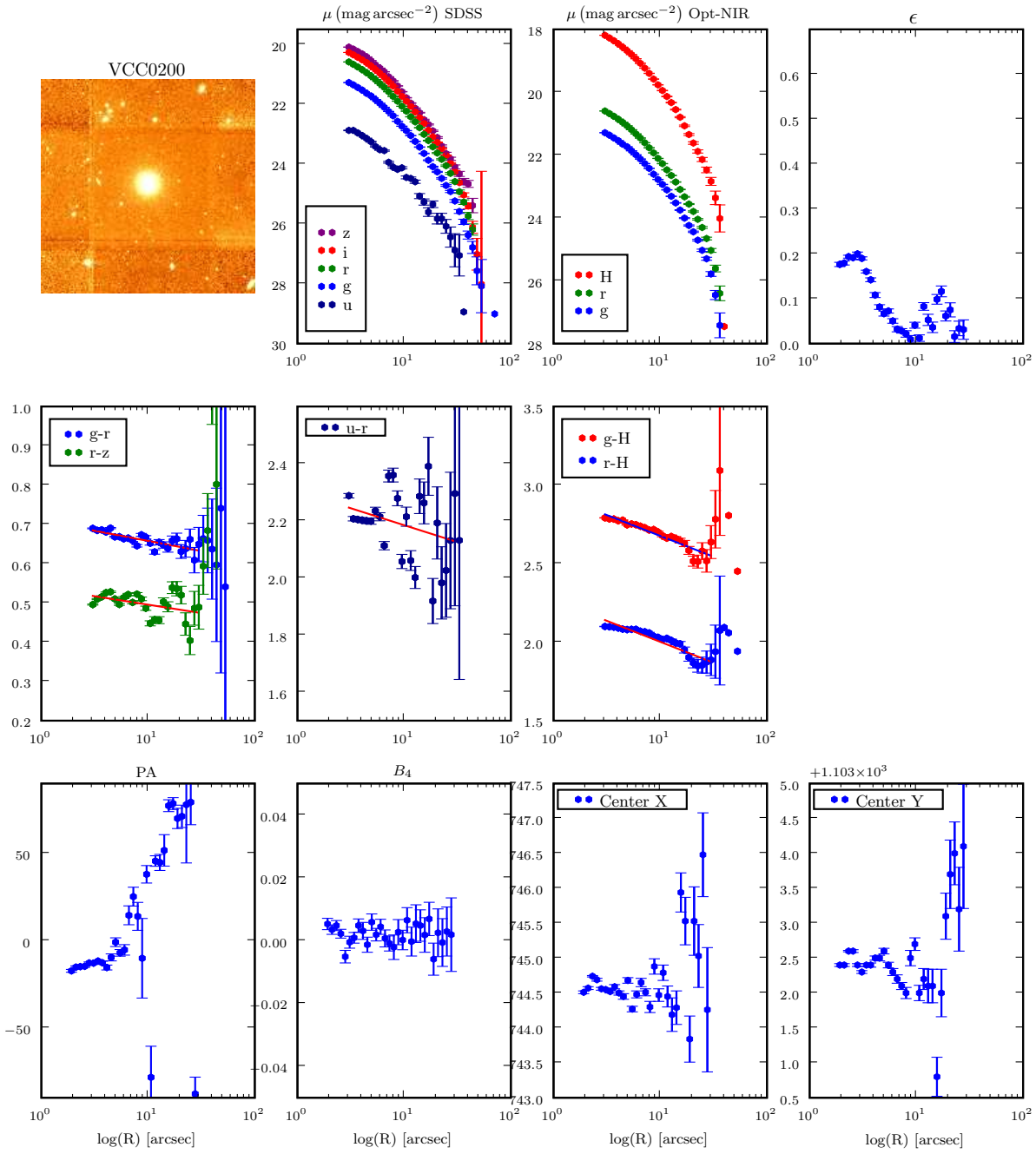

Figure A.18. VCC0200 Surface Photometry Results

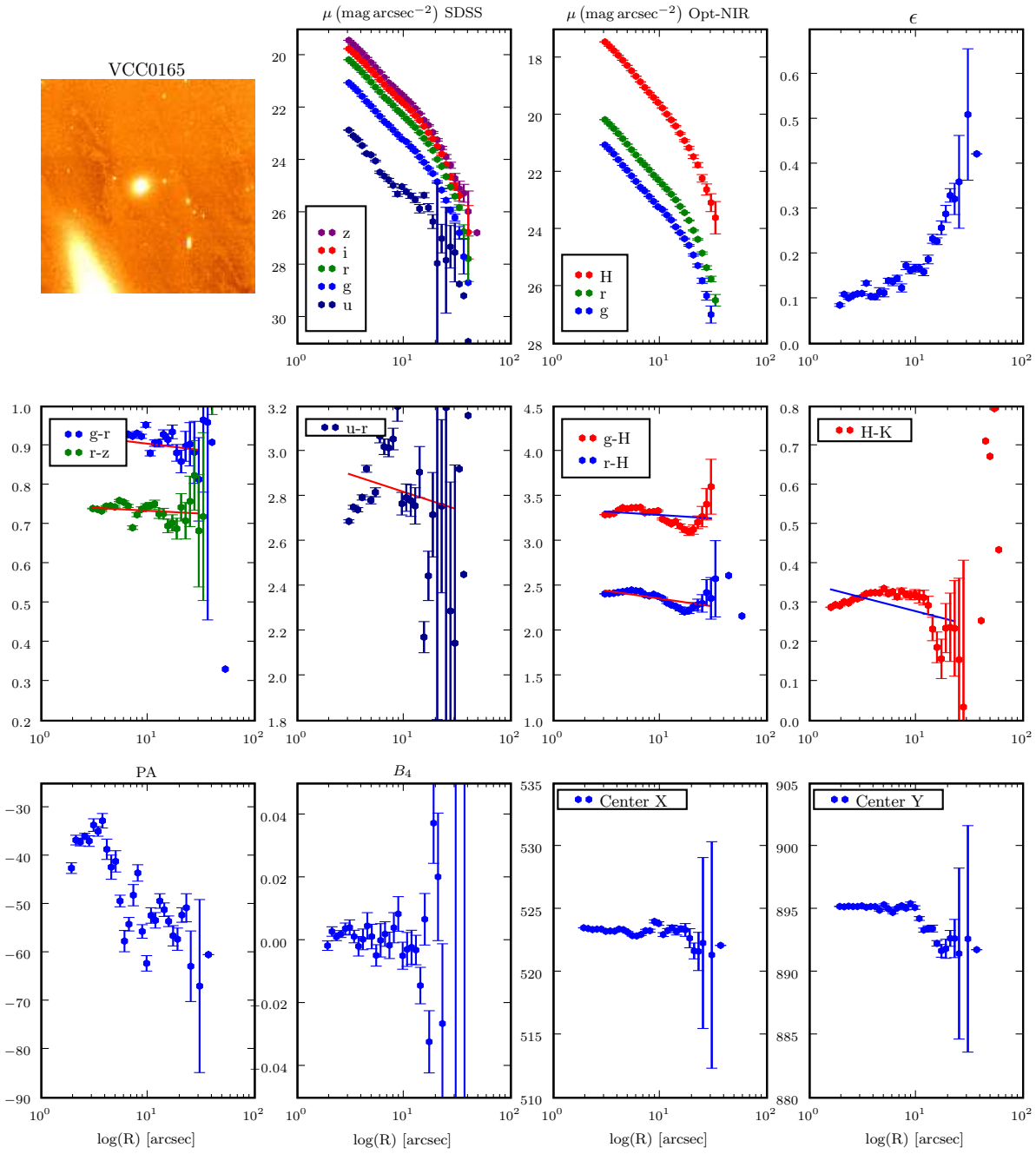

Figure A.19. VCC0165 Surface Photometry Results

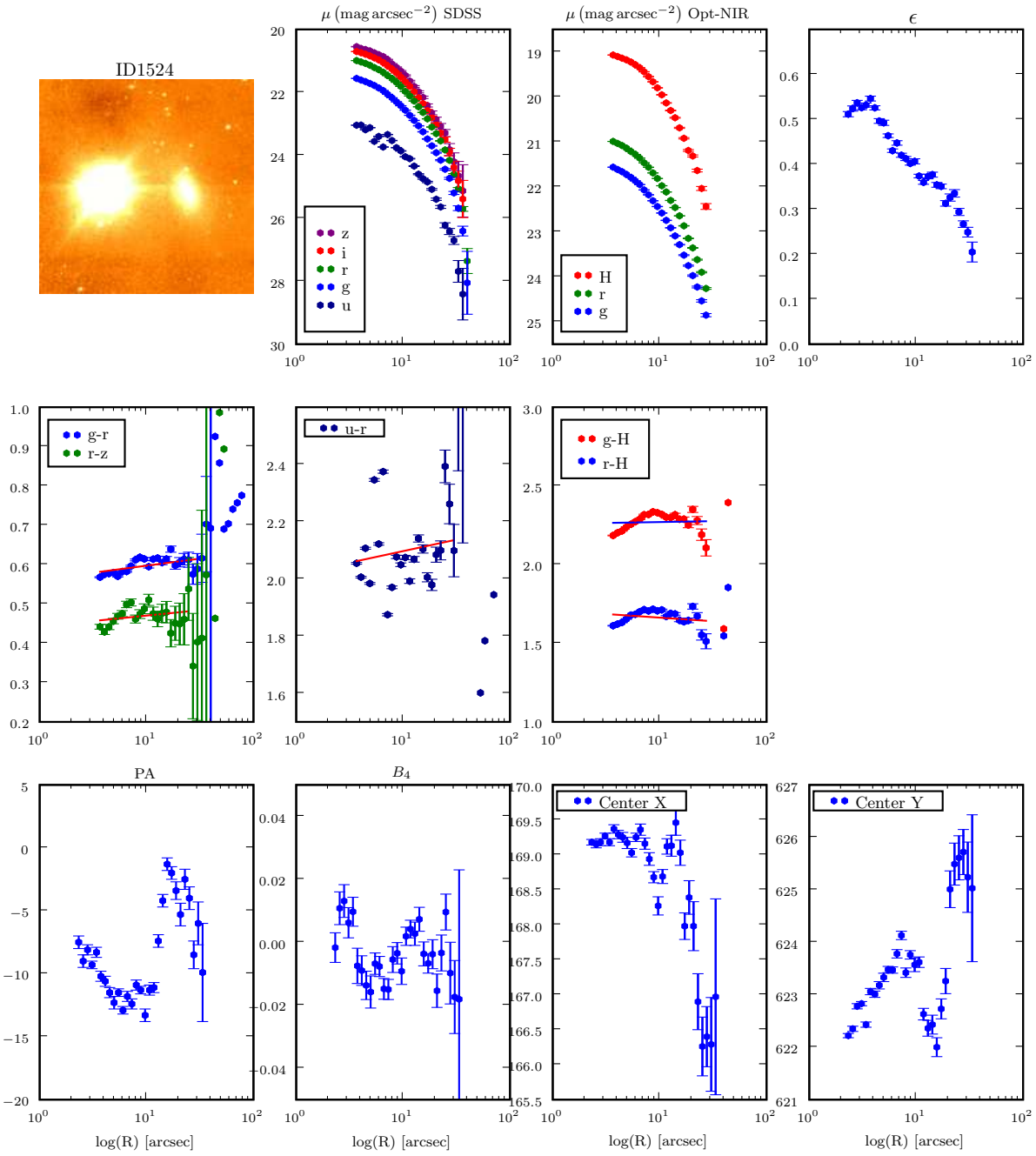

Figure A.20. ID1524 Surface Photometry Results

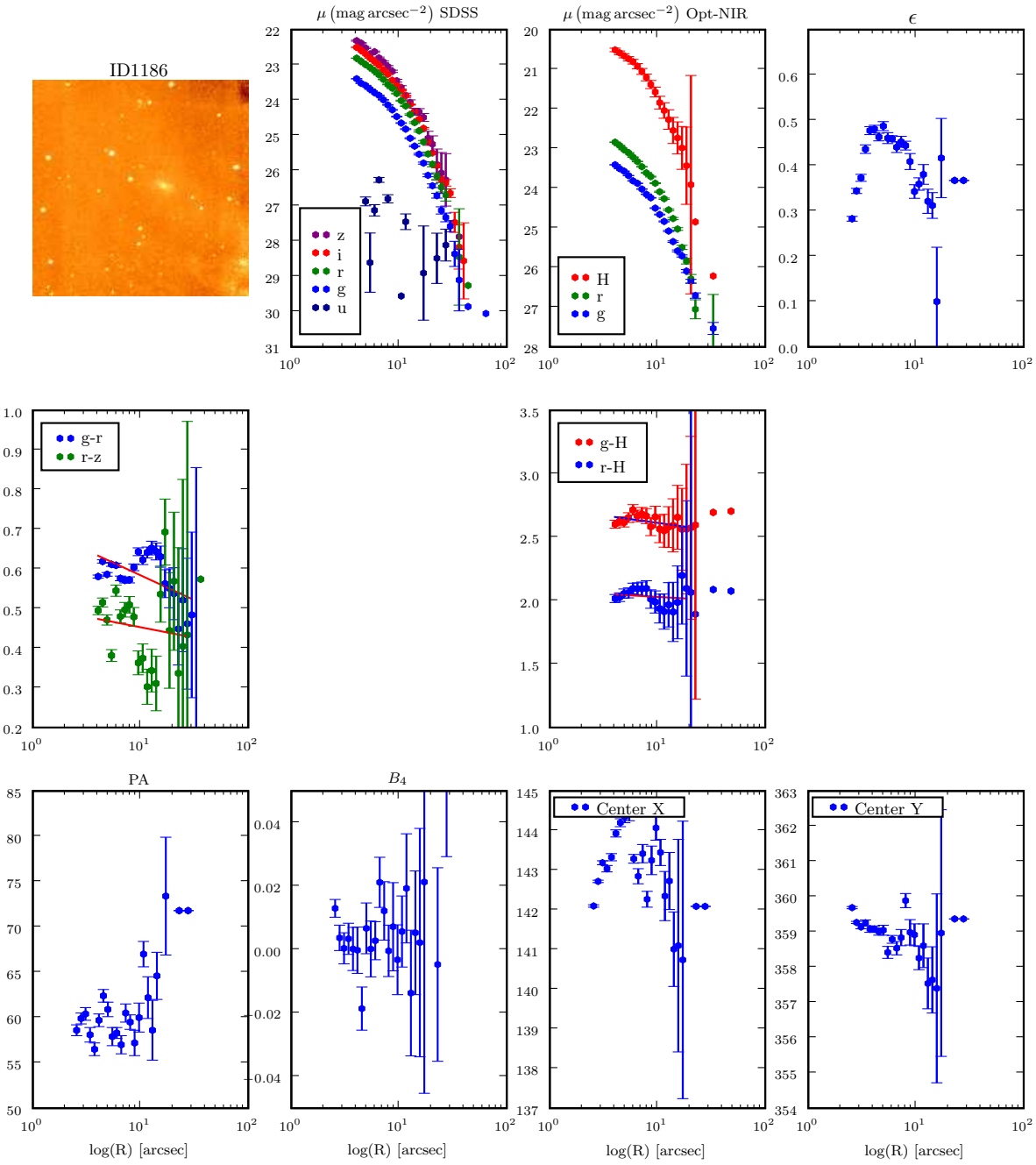

Figure A.21. ID1186 Surface Photometry Results

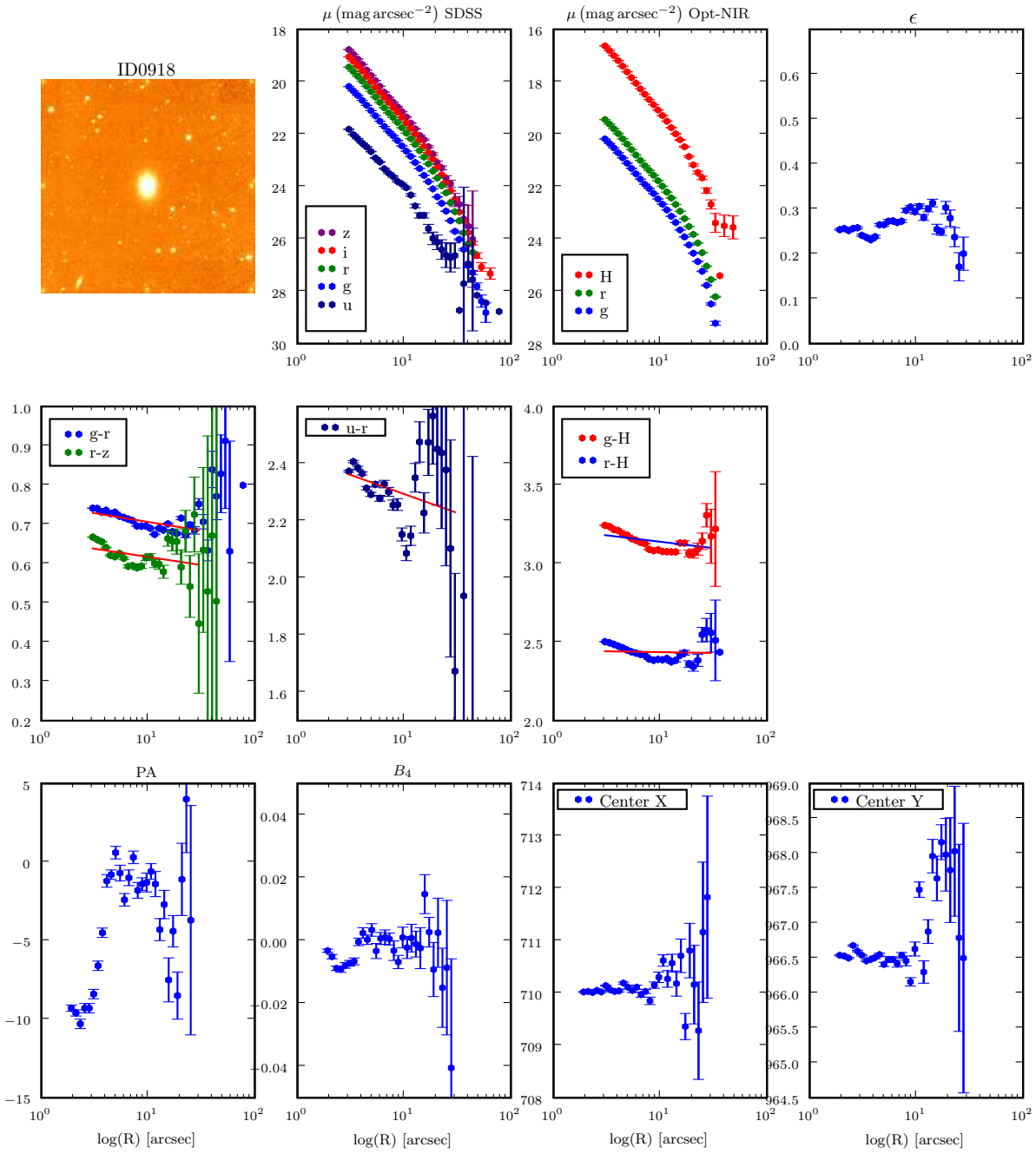

Figure A.22. ID0918 Surface Photometry Results

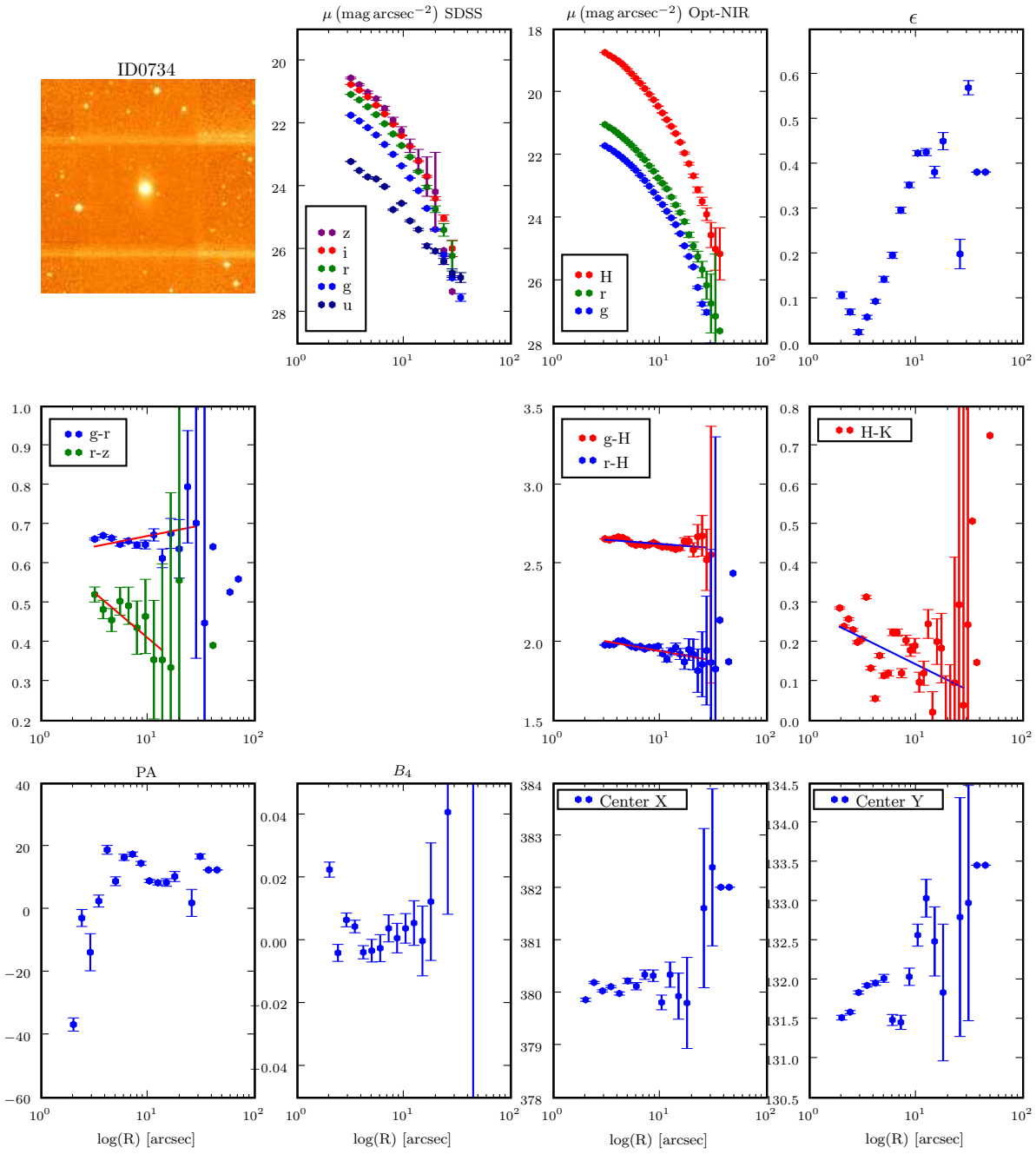

Figure A.23. ID0734 Surface Photometry Results

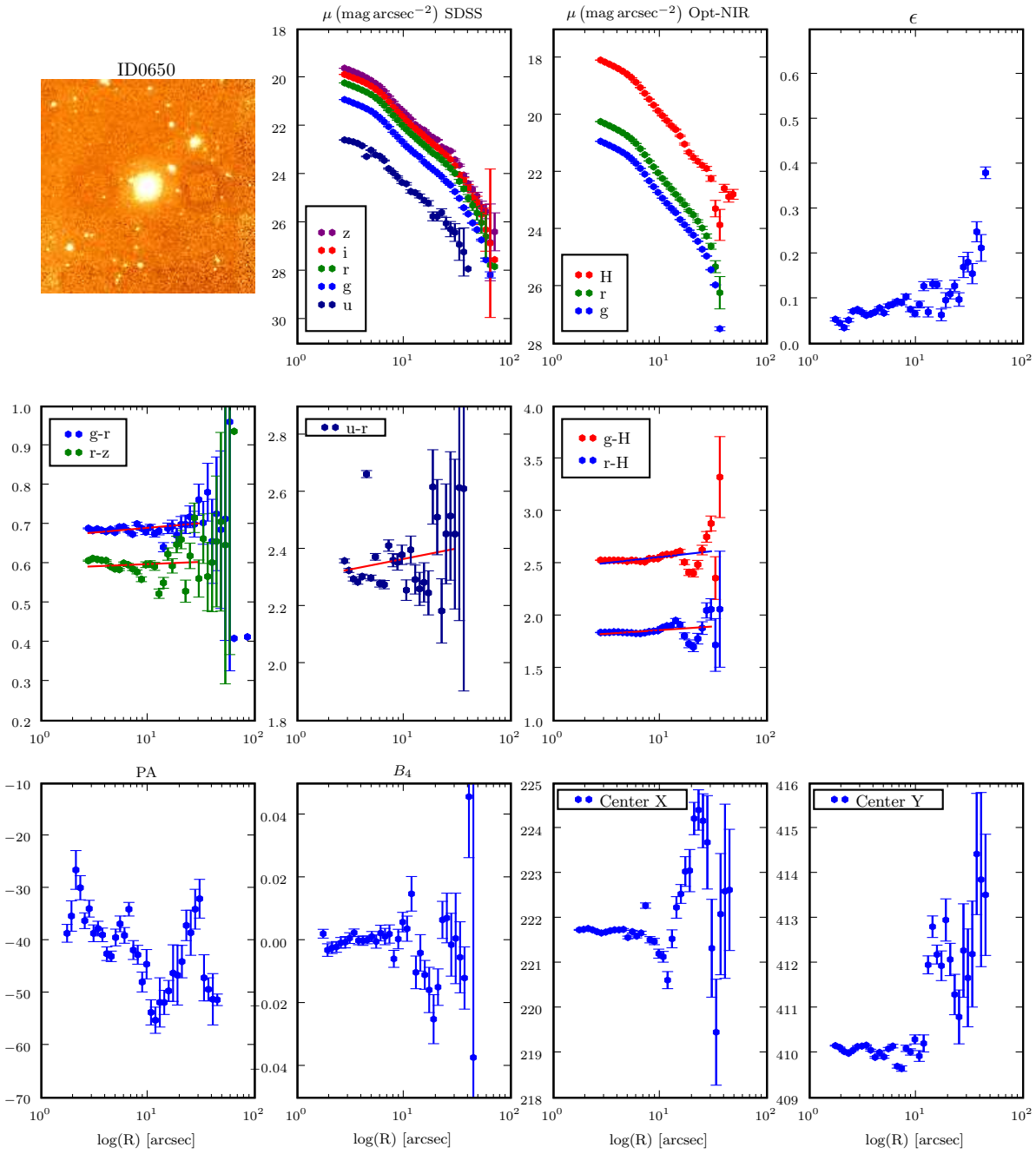

Figure A.24. ID0650 Surface Photometry Results

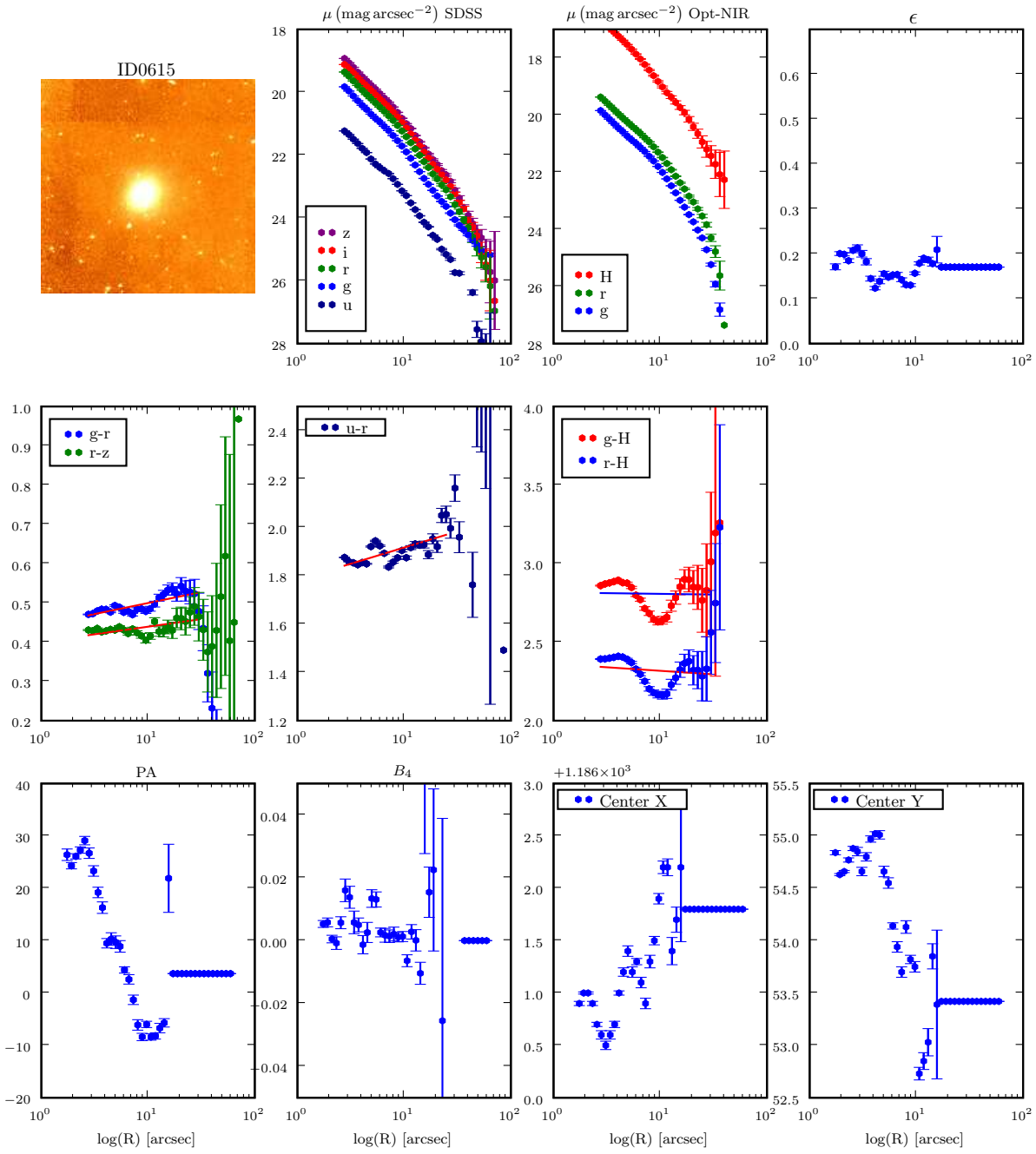

Figure A.25. ID0615 Surface Photometry Results

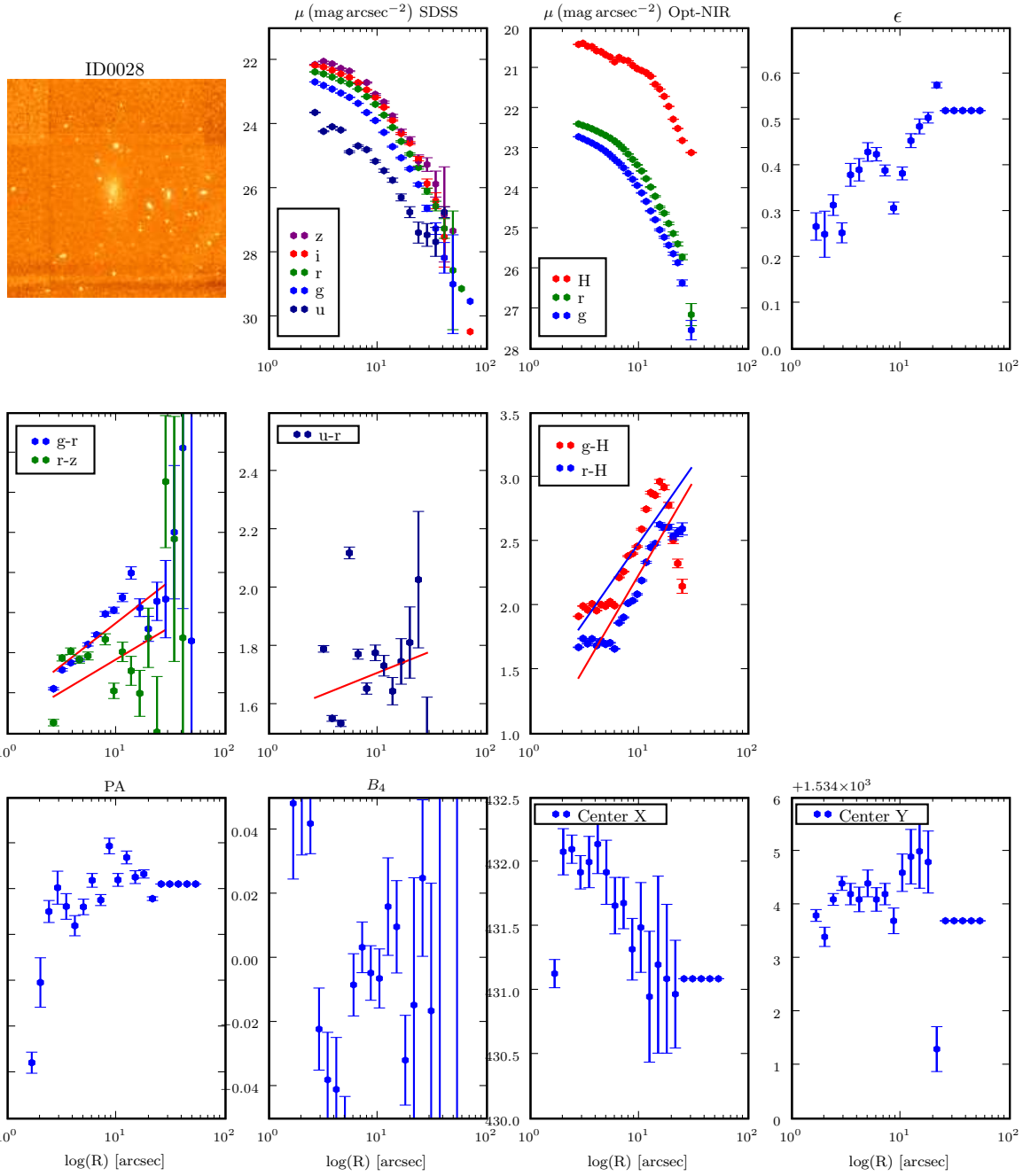

Figure A.26. ID0028 Surface Photometry Results

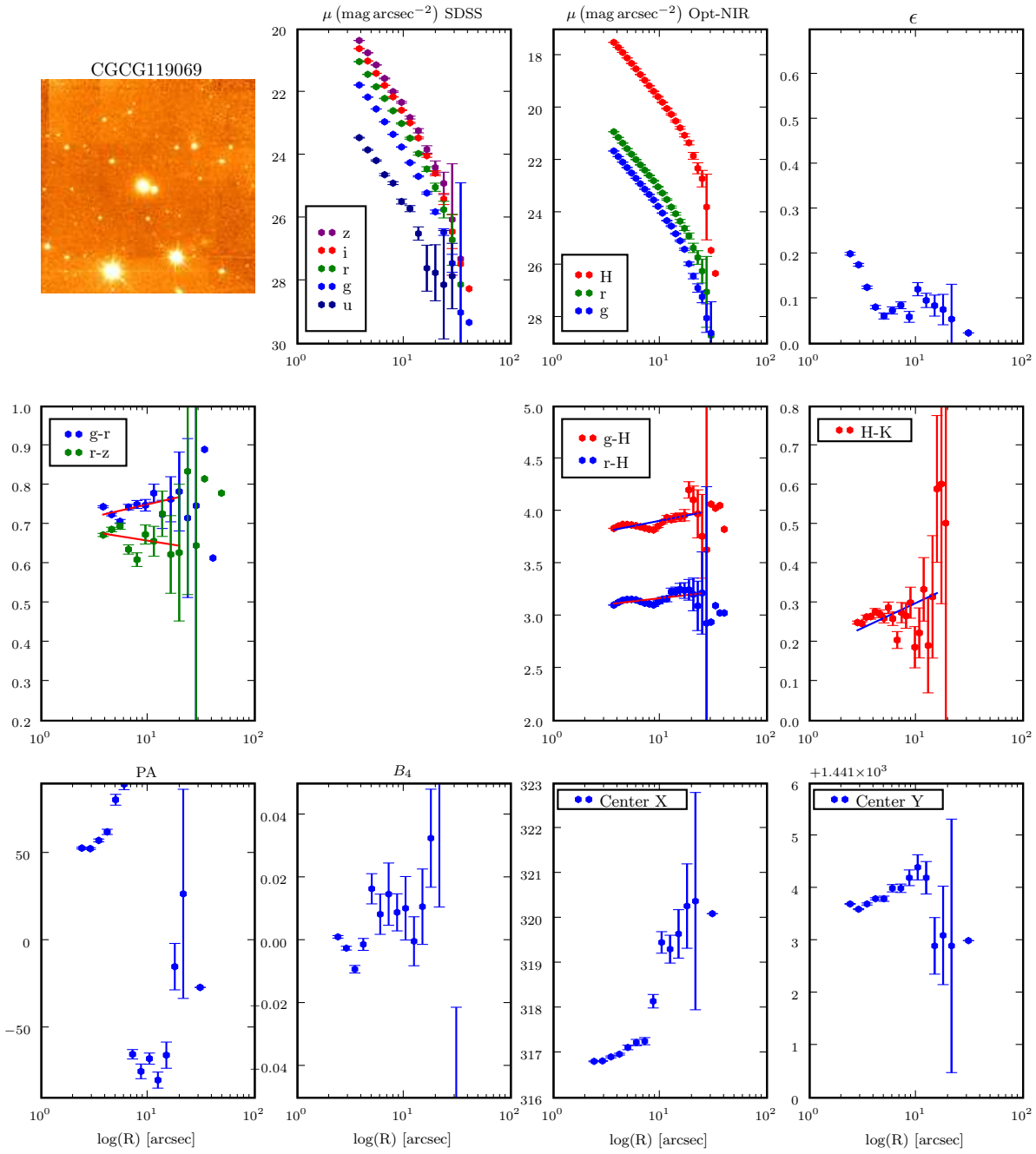

Figure A.27. CGCG119069 Surface Photometry Results

APPENDIX B

B.1 Surface Photometry Results; Colours, Colour Gradients, Spectroscopic Indices

Galaxy	**g-r**	err_{g-r}	∇ **(g-r)**	$\mathrm{err}_{\nabla(g-r)}$
CGCG119069	0.6886	0.0789	0.0624	0.1121
ID0615	0.4435	0.0214	0.0559	0.0333
ID0650	0.6672	0.0189	0.0237	0.0304
ID0734	0.6166	0.1630	-	-
ID0918	0.7504	0.0061	-0.0444	0.0085
ID1186	0.7092	0.1370	-	-
ID1524	0.5613	0.0191	0.0358	0.0261
VCC0165	0.9378	0.0472	-0.0327	0.0359
VCC0200	0.7092	0.0204	-0.0515	0.0302
VCC0397	0.6835	0.0472	-0.0247	0.0326
VCC0407	0.6325	0.0267	-0.0093	0.0340
VCC0482	0.7119	0.0123	-0.0135	0.0183
VCC0523	0.6720	0.0188	-0.0252	0.0266
VCC0817	0.6881	0.0104	-0.0675	0.0179
VCC0940	0.7309	0.0124	-0.0319	0.0173
VCC0990	0.6696	0.0110	-0.0047	0.0157
VCC1087	0.6994	0.0366	0.0076	0.0483
VCC1183	0.7007	0.0415	0.0169	0.0452
VCC1261	0.6893	0.0154	-0.0163	0.0198
VCC1431	0.8217	0.0348	-0.0411	0.0448
VCC1861	0.7570	0.0094	-0.0529	0.0136
VCC1871	0.7816	0.0346	0.0037	0.0454
VCC1910	0.7748	0.0104	-0.0310	0.0147
VCC1912	0.5114	0.0088	-	-
VCC1947	0.7748	0.0064	-0.0772	0.0083

Table B.1. g-r Colours and Gradients

Galaxy	**r-z**	$\mathrm{err}_{\mathrm{r-z}}$	∇ **(r-z)**	$\mathrm{err}_{\nabla(\mathrm{r-z})}$
CGCG119069	0.7015	0.1362	-0.0433	0.1925
ID0615	0.4006	0.0283	0.0386	0.0442
ID0650	0.5874	0.0221	0.0112	0.0356
ID0734	0.6409	0.1695	-	-
ID0918	0.6584	0.0709	-0.0414	0.0475
ID1186	0.5057	0.3489	-	-
ID1524	0.4425	0.0471	0.0276	0.0309
VCC0165	0.7493	0.0585	-0.0147	0.0813
VCC0200	0.5383	0.0271	-0.0429	0.0399
VCC0397	0.5586	0.0853	0.0235	0.0324
VCC0407	0.5376	0.0426	-0.0516	0.0537
VCC0482	0.6310	0.0715	0.0018	0.0587
VCC0523	0.5951	0.0260	-0.0525	0.0366
VCC0817	0.5526	0.0149	-0.0777	0.0254
VCC0940	0.6039	0.0473	-0.0229	0.0659
VCC0990	0.5549	0.0491	-0.0122	0.0639
VCC1087	0.6163	0.0444	-0.0415	0.0584
VCC1183	0.6014	0.0603	-0.0530	0.0759
VCC1261	0.5544	0.0292	-0.0417	0.0374
VCC1431	0.6838	0.0434	-0.0830	0.0594
VCC1861	0.6732	0.0322	-0.0771	0.0457
VCC1871	0.7391	0.0267	-0.1014	0.0376
VCC1910	0.6873	0.0243	-0.0348	0.0354
VCC1912	0.4515	0.0235	0.0243	0.0324
VCC1947	0.6908	0.0207	-0.0750	0.0281

Table B.2. r-z Colours and Gradients

Galaxy	**u-r**	$\mathrm{err}_{\mathrm{u-r}}$	∇ **(u-r)**	$\mathrm{err}_{\nabla(\mathrm{u-r})}$
CGCG119069	-	-	-	-
ID0615	1.6337	0.1093	0.3128	0.1398
ID0650	2.2931	0.1224	0.0735	0.1910
ID0734	-	-	-	-
ID0918	2.4265	0.2363	-0.1331	0.3310
ID1186	-	-	-	-
ID1524	2.0164	0.0484	0.0804	0.0651
VCC0165	-	-	-	-
VCC0200	2.3029	0.1568	-0.1186	0.2281
VCC0397	2.3298	0.1157	0.0173	0.1528
VCC0407	2.2128	0.0756	-0.2109	0.0944
VCC0482	2.3179	0.0167	0.0142	0.0279
VCC0523	2.2955	0.0666	-0.0797	0.0936
VCC0817	2.1555	0.0615	0.0020	0.1156
VCC0940	2.4279	0.0529	-0.0353	0.1090
VCC0990	2.1846	0.1376	-0.0224	0.1951
VCC1087	2.3104	0.1098	0.0122	0.1557
VCC1183	2.2621	0.0785	0.0234	0.0928
VCC1261	2.2042	0.0890	-0.0231	0.1139
VCC1431	2.4670	0.1214	-0.0675	0.1654
VCC1861	2.3642	0.1129	0.0544	0.1400
VCC1871	2.6062	0.2043	-0.1082	0.2929
VCC1910	2.6400	0.1102	-0.0615	0.1412
VCC1912	1.9795	0.0738	0.0921	0.1023
VCC1947	2.5303	0.0710	-0.1905	0.0961

Table B.3. u-r Colours and Gradients

Galaxy	**g-H**	$\text{err}_{\text{g}-\text{H}}$	∇ **(g-H)**	$\text{err}_{\nabla(\text{g}-\text{H})}$
CGCG119069	3.7095	0.2013	0.2002	0.2585
ID0615	2.8163	0.1679	-0.0090	0.2405
ID0650	2.4490	0.0329	0.1137	0.0506
ID0734	2.6769	0.0798	-0.0520	0.1089
ID0918	3.2201	0.0592	-0.0813	0.0796
ID1186	2.7295	0.3642	-0.1163	0.2253
ID1524	2.2584	0.0268	0.0115	0.0375
VCC0165	3.3670	0.1142	-0.0762	0.1545
VCC0200	2.9410	0.0462	-0.2650	0.0651
VCC0397	3.0867	0.2211	-0.0385	0.0696
VCC0407	2.9170	0.0322	-0.0771	0.0422
VCC0482	3.0415	0.0684	0.0379	0.0887
VCC0523	-	-	-	-
VCC0817	2.3432	0.0098	-0.0877	0.0168
VCC0940	2.8597	0.0596	0.0158	0.0891
VCC0990	-	-	-	-
VCC1087	-	-	-	-
VCC1183	-	-	-	-
VCC1261	3.2118	0.0435	0.0541	0.0559
VCC1431	-	-	-	-
VCC1861	3.1790	0.0266	-0.1134	0.0381
VCC1871	3.3048	0.0231	-0.1021	0.0325
VCC1910	3.3659	0.0358	-0.1144	0.0489
VCC1912	2.6576	0.1389	0.1335	0.1905
VCC1947	-	-	-	-

Table B.4. g-H Colours and Gradients

Galaxy	**r-H**	$\text{err}_{\text{r}-\text{H}}$	∇ **(r-H)**	$\text{err}_{\nabla(\text{r}-\text{H})}$
CGCG119069	3.0506	0.2116	0.1191	0.2761
ID0615	2.3623	0.1162	-0.0449	0.1722
ID0650	1.7955	0.0449	0.0694	0.0686
ID0734	2.0648	0.1412	-0.1218	0.1950
ID0918	2.4469	0.0495	-0.0107	0.0672
ID1186	2.0768	0.4701	-0.0471	0.2599
ID1524	1.7085	0.0242	-0.0459	0.0339
VCC0165	2.5335	0.0924	-0.1743	0.0257
VCC0200	2.2688	0.0446	-0.2670	0.0629
VCC0397	2.4352	0.1810	-0.0538	0.2210
VCC0407	2.2667	0.0358	-0.0459	0.0461
VCC0482	2.3729	0.0352	-0.0064	0.0476
VCC0523	-	-	-	-
VCC0817	1.6521	0.0118	-0.0207	0.0199
VCC0940	2.1921	0.0613	-0.0560	0.0918
VCC0990	-	-	-	-
VCC1087	-	-	-	-
VCC1183	-	-	-	-
VCC1261	2.5364	0.0447	0.0540	0.0575
VCC1431	-	-	-	-
VCC1861	2.4585	0.0283	-0.1119	0.0403
VCC1871	2.5176	0.0210	-0.0989	0.0296
VCC1910	2.6126	0.0244	-0.1160	0.0341
VCC1912	2.1397	0.1388	0.0404	0.1904
VCC1947	-	-	-	-

Table B.5. r-H Colours and Gradients

Galaxy	**H-K**	$\text{err}_{\text{H}-\text{K}}$	∇ **(H-K)**	$\text{err}_{\nabla(\text{H}-\text{K})}$
CGCG119069	-	-	-	-
ID0615	-	-	-	-
ID0650	-	-	-	-
ID0734	-	-	-	-
ID0918	-	-	-	-
ID1186	-	-	-	-
ID1524	-	-	-	-
VCC0165	0.3480	0.0300	-0.0698	0.0619
VCC0200	0.2811	0.0326	-0.0176	0.0633
VCC0397	-	-	-	-
VCC0407	0.3009	0.0266	0.0213	0.0436
VCC0482	0.1905	0.0319	-0.0156	0.0547
VCC0523	-	-	-	-
VCC0817	0.3799	0.0724	-0.0975	0.1313
VCC0940	0.2325	0.0198	0.0045	0.0393
VCC0990	-	-	-	-
VCC1087	-	-	-	-
VCC1183	-	-	-	-
VCC1261	0.1664	0.0226	-0.0215	0.0432
VCC1431	-	-	-	-
VCC1861	0.2922	0.0165	-0.0098	0.0319
VCC1871	0.2528	0.0127	-0.0288	0.0256
VCC1910	0.1489	0.0398	0.0273	0.0790
VCC1912	-	-	-	-
VCC1947	-	-	-	-

Table B.6. H-K Colours and Gradients

Galaxy	**HγA**	$\text{err}_{\text{H}\gamma\text{A}}$	**HγF**	$\text{err}_{\text{H}\gamma\text{F}}$	**HδA**	$\text{err}_{\text{H}\delta\text{A}}$	**HδF**	$\text{err}_{\text{H}\delta\text{F}}$	**Hβ**	$\text{err}_{\text{H}\beta}$
CGCG119069	0.000	0.000	0.000	0.000	0.000	0.000	0.000	0.000	0.000	0.000
ID0615	0.000	0.000	0.000	0.000	0.000	0.000	0.000	0.000	0.000	0.000
ID0650	2.639	0.716	0.270	0.436	0.588	0.765	0.921	0.521	1.992	0.418
ID0734	0.248	1.297	1.664	0.814	0.387	1.369	1.985	0.936	2.205	0.751
ID0918	3.537	0.446	0.416	0.266	1.534	0.470	0.721	0.315	2.121	0.249
ID1186	0.000	0.000	0.000	0.000	0.000	0.000	0.000	0.000	0.000	0.000
ID1524	2.586	1.017	3.228	0.613	2.938	1.016	2.660	0.726	2.838	0.714
VCC0165	0.000	0.000	0.000	0.000	0.000	0.000	0.000	0.000	0.000	0.000
VCC0200	0.000	0.000	0.000	0.000	0.000	0.000	0.000	0.000	0.000	0.000
VCC0397	0.062	0.898	1.762	0.536	1.383	0.966	2.120	0.672	2.850	0.529
VCC0407	0.000	0.000	0.000	0.000	0.000	0.000	0.000	0.000	0.000	0.000
VCC0482	0.000	0.000	0.000	0.000	0.000	0.000	0.000	0.000	0.000	0.000
VCC0523	1.369	0.925	0.689	0.570	1.045	0.960	1.316	0.689	2.423	0.552
VCC0817	0.000	0.000	0.000	0.000	0.000	0.000	0.000	0.000	0.000	0.000
VCC0940	0.000	0.000	0.000	0.000	0.000	0.000	0.000	0.000	0.000	0.000
VCC0990	0.065	0.468	0.782	0.298	0.094	0.500	1.269	0.345	1.834	0.316
VCC1087	1.335	0.820	0.968	0.493	0.540	0.894	0.838	0.613	2.093	0.469
VCC1183	1.458	0.581	0.753	0.356	0.367	0.649	1.200	0.442	2.416	0.333
VCC1261	1.177	0.534	0.982	0.326	0.440	0.546	1.572	0.380	2.416	0.328
VCC1431	2.219	0.548	0.185	0.342	0.695	0.586	0.786	0.403	1.599	0.320
VCC1861	2.554	1.364	0.365	0.824	1.173	1.505	1.354	1.012	1.931	0.742
VCC1871	0.000	0.000	0.000	0.000	0.000	0.000	0.000	0.000	0.000	0.000
VCC1910	2.977	0.591	0.392	0.362	1.741	0.656	0.373	0.449	1.886	0.335
VCC1912	3.535	0.326	3.222	0.201	3.720	0.327	3.212	0.232	3.705	0.238
VCC1947	4.070	0.535	0.879	0.322	1.352	0.579	0.621	0.399	2.141	0.289

Table B.7. Spectroscopic Indexes from Michielsen et al. [2008]

BIBLIOGRAPHY

T. M. Abbott, C. Aspin, A. N. Sorensen, P. Norregaard, J. Andersen, M. I. Andersen, N. S. van der Bliek, J. W. Clasen, G. C. Cox, J. Klougart, H. H. Larsen, N. Michaelsen, B. Noel, G. Olofsson, C. Perez, and H. E. Schwarz. SWIR at the Nordic Optical Telescope: NOTCam. In M. Iye and A. F. Moorwood, editors, *Proc. SPIE Vol. 4008, p. 714-719, Optical and IR Telescope Instrumentation and Detectors, Masanori Iye; Alan F. Moorwood; Eds.*, volume 4008 of *Presented at the Society of Photo-Optical Instrumentation Engineers (SPIE) Conference*, pages 714–719, August 2000.

C. Baffa, G. Comoretto, S. Gennari, F. Lisi, E. Oliva, V. Biliotti, A. Checcucci, V. Gavrioussev, E. Giani, F. Ghinassi, L. K. Hunt, R. Maiolino, F. Mannucci, G. Marcucci, M. Sozzi, P. Stefanini, and L. Testi. NICS: The TNG Near Infrared Camera Spectrometer. *A&A*, 378:722–728, November 2001. doi: 10.1051/0004-6361:20011194.

M. E. Bailey and W. B. Sparks. The quick convolution of galaxy profiles, with application to power-law intensity distributions. *MNRAS*, 204:53P–58P, August 1983.

F. D. Barazza, B. Binggeli, and H. Jerjen. VLT surface photometry and isophotal analysis of early-type dwarf galaxies in the Virgo cluster. *A&A*, 407:121–135, August 2003. doi: 10.1051/0004-6361:20030872.

R. Bender, P. Surma, S. Doebereiner, C. Moellenhoff, and R. Madejsky. Isophote shapes of elliptical galaxies. II - Correlations with global optical, radio and X-ray properties. *A&A*, 217:35–43, June 1989.

E. Bertin and S. Arnouts. SExtractor: Software for source extraction. *A&AS*, 117: 393–404, June 1996.

B. Binggeli, A. Sandage, and G. A. Tammann. Studies of the Virgo Cluster. II - A catalog of 2096 galaxies in the Virgo Cluster area. *AJ*, 90:1681–1759, September 1985. doi: 10.1086/113874.

A. Boselli, L. Cortese, J. M. Deharveng, G. Gavazzi, K. S. Yi, A. Gil de Paz, M. Seibert, S. Boissier, J. Donas, Y.-W. Lee, B. F. Madore, D. C. Martin, R. M. Rich, and Y.-J. Sohn. UV Properties of Early-Type Galaxies in the Virgo Cluster. *ApJ*, 629:L29–L32, August 2005. doi: 10.1086/444534.

G. Bruzual and S. Charlot. Stellar population synthesis at the resolution of 2003. *MNRAS*, 344:1000–1028, October 2003. doi: 10.1046/j.1365-8711.2003.06897.x.

G. Bruzual A. and S. Charlot. Spectral evolution of stellar populations using isochrone synthesis. *ApJ*, 405:538–553, March 1993. doi: 10.1086/172385.

N. Caldwell. Structure and stellar content of dwarf elliptical galaxies. *AJ*, 88: 804–812, June 1983. doi: 10.1086/113367.

D. Carter. Weak disks in rapidly rotating elliptical galaxies. *ApJ*, 312:514–517, January 1987. doi: 10.1086/164897.

C. J. Conselice. The Relationship between Stellar Light Distributions of Galaxies and Their Formation Histories. *ApJS*, 147:1–28, July 2003. doi: 10.1086/375001.

L.E. Davis. *A User's Guide to the IRAF Apphot Package, iraf.noao.edu/iraf/ftp/iraf/docs/apuser.ps.Z*. 1989.

R. A. E. Fosbury, M. Villar-Martín, A. Humphrey, M. Lombardi, P. Rosati, D. Stern, R. N. Hook, B. P. Holden, S. A. Stanford, G. K. Squires, M. Rauch, and W. L. W. Sargent. Massive Star Formation in a Gravitationally Lensed H II Galaxy at z = 3.357. *ApJ*, 596:797–809, October 2003. doi: 10.1086/378228.

M. Franx, G. Illingworth, and T. Heckman. Multicolor surface photometry of 17 ellipticals. *AJ*, 98:538–576, August 1989. doi: 10.1086/115157.

M. Fukugita, T. Ichikawa, J. E. Gunn, M. Doi, K. Shimasaku, and D. P. Schneider. The Sloan Digital Sky Survey Photometric System. *AJ*, 111:1748–+, April 1996. doi: 10.1086/117915.

G. Gavazzi, A. Boselli, A. Donati, P. Franzetti, and M. Scodeggio. Introducing GOLDMine: A new galaxy database on the WEB. *A&A*, 400:451–455, March 2003. doi: 10.1051/0004-6361:20030026.

E. Grebel, K. S. de Boer, R.-J. Dettmar, and U. Klein, editors. *Dwarf galaxies and their environment*, 2001.

E. K. Grebel, J. S. Gallagher, III, and D. Harbeck. The Progenitors of Dwarf Spheroidal Galaxies. *AJ*, 125:1926–1939, April 2003. doi: 10.1086/368363.

J. E. Gunn, M. Carr, C. Rockosi, M. Sekiguchi, K. Berry, B. Elms, E. de Haas, Ž. Ivezić, G. Knapp, R. Lupton, G. Pauls, R. Simcoe, R. Hirsch, D. Sanford, S. Wang, D. York, F. Harris, J. Annis, L. Bartozek, W. Boroski, J. Bakken, M. Haldeman, S. Kent, S. Holm, D. Holmgren, D. Petravick, A. Prosapio, R. Rechenmacher, M. Doi, M. Fukugita, K. Shimasaku, N. Okada, C. Hull, W. Siegmund, E. Mannery, M. Blouke, D. Heidtman, D. Schneider, R. Lucinio, and J. Brinkman. The Sloan Digital Sky Survey Photometric Camera. *AJ*, 116: 3040–3081, December 1998. doi: 10.1086/300645.

G. Hinshaw, J. L. Weiland, R. S. Hill, N. Odegard, D. Larson, C. L. Bennett, J. Dunkley, B. Gold, M. R. Greason, N. Jarosik, E. Komatsu, M. R. Nolta, L. Page, D. N. Spergel, E. Wollack, M. Halpern, A. Kogut, M. Limon, S. S. Meyer, G. S. Tucker, and E. L. Wright. Five-Year Wilkinson Microwave Anisotropy Probe (WMAP) Observations: Data Processing, Sky Maps, and Basic Results. *ArXiv e-prints*, 803, March 2008.

S. B. Howell. Two-dimensional aperture photometry - Signal-to-noise ratio of point-source observations and optimal data-extraction techniques. *PASP*, 101:616–622, June 1989.

I. R. King. The Profile of a Star Image. *PASP*, 83:199–+, April 1971.

J. Kormendy. Families of ellipsoidal stellar systems and the formation of dwarf elliptical galaxies. *ApJ*, 295:73–79, August 1985. doi: 10.1086/163350.

C. Lacey and S. Cole. Merger rates in hierarchical models of galaxy formation. *MNRAS*, 262:627–649, June 1993.

A. Manchado, F. J. Fuentes, F. Prada, E. Ballesteros, M. Barreto, J. M. Carranza, I. Escudero, A. B. Fragoso-Lopez, E. Joven-Alvarez, A. Manescau, M. Pi, L. F. Rodriguez-Ramos, and N. A. Sosa. LIRIS: a long-slit intermediate-resolution infrared spectrograph for the WHT. In A. M. Fowler, editor, *Proc. SPIE Vol. 3354, p. 448-455, Infrared Astronomical Instrumentation, Albert M. Fowler; Ed.*, volume 3354 of *Presented at the Society of Photo-Optical Instrumentation Engineers (SPIE) Conference*, pages 448–455, August 1998.

F. Mannucci. *SNAP: Sppedy Near-Infrared data Automatic Pipeline, www.arcetri.astro.it/∼filippo/snap/.* 2002.

A. T. Marlowe, G. R. Meurer, and T. M. Heckman. The Taxonomy of Blue Amorphous Galaxies. II. Structure and Evolution. *ApJ*, 522:183–198, September 1999. doi: 10.1086/307603.

M. L. Mateo. Dwarf Galaxies of the Local Group. *ARA&A*, 36:435–506, 1998. doi: 10.1146/annurev.astro.36.1.435.

D. Michielsen. *Observations and N-body/SPH simulations of the interstellar medium in dwarf elliptical galaxies.* PhD thesis, Universiteit Gent (Belgium), Belgium, 2005.

D. Michielsen, A. Boselli, C. J. Conselice, E. Toloba, I. M. Whiley, A. Aragón-Salamanca, M. Balcells, N. Cardiel, A. J. Cenarro, J. Gorgas, R. F. Peletier, and A. Vazdekis. The relation between stellar populations, structure and environment for dwarf elliptical galaxies from the MAGPOP-ITP. *MNRAS*, pages 340–+, March 2008. doi: 10.1111/j.1365-2966.2008.12846.x.

B. Milvang-Jensen. Properties of E and S0 Galaxies in the Clusters HydraI and Coma. *Masters Thesis*, July 1997.

B. Moore, S. Ghigna, F. Governato, G. Lake, T. Quinn, J. Stadel, and P. Tozzi. Dark Matter Substructure within Galactic Halos. *ApJL*, 524:L19–L22, October 1999. doi: 10.1086/312287.

J. F. Navarro, C. S. Frenk, and S. D. M. White. The assembly of galaxies in a hierarchically clustering universe. *MNRAS*, 275:56–66, July 1995.

E. Oliva. NICS, the Near Infrared Camera-Spectrometer of the TNG. *Memorie della Societa Astronomica Italiana*, 74:118–+, 2003.

R. F. Peletier, R. L. Davies, G. D. Illingworth, L. E. Davis, and M. Cawson. CCD surface photometry of galaxies with dynamical data. II - UBR photometry of 39 elliptical galaxies. *AJ*, 100:1091–1142, October 1990. doi: 10.1086/115582.

N.R. Pogson. Magnitudes of Thirty-six of the Minor Planets for the first day of each month of the year 1857. *MNRAS*, 17:12–+, November 1856.

M. Pohlen and I. Trujillo. The structure of galactic disks. Studying late-type spiral galaxies using SDSS. *A&A*, 454:759–772, August 2006. doi: 10.1051/0004-6361:20064883.

P. Prugniel, E. Bica, A. Klotz, and D. Alloin. Low-luminosity early-type galaxies. I - Photometry and morphology. *A&AS*, 98:229–243, April 1993.

A. Sandage and B. Binggeli. Studies of the Virgo cluster. III - A classification system and an illustrated atlas of Virgo cluster dwarf galaxies. *AJ*, 89:919–931, July 1984. doi: 10.1086/113588.

A. Sandage, B. Binggeli, and G. A. Tammann. Studies of the Virgo Cluster - Part Five - Luminosity Functions of Virgo Cluster Galaxies. *AJ*, 90:1759–1771, September 1985. doi: 10.1086/113875.

F. Schweizer. Effects of seeing on the light distribution in the cores of elliptical galaxies. *ApJ*, 233:23–34, October 1979. doi: 10.1086/157362.

F. Schweizer. Further estimates of the effects of seeing on the light distribution in the cores of elliptical galaxies. *AJ*, 86:662–666, May 1981. doi: 10.1086/112931.

M. F. Skrutskie, R. M. Cutri, R. Stiening, M. D. Weinberg, S. Schneider, J. M. Carpenter, C. Beichman, R. Capps, T. Chester, J. Elias, J. Huchra, J. Liebert, C. Lonsdale, D. G. Monet, S. Price, P. Seitzer, T. Jarrett, J. D. Kirkpatrick, J. E. Gizis, E. Howard, T. Evans, J. Fowler, L. Fullmer, R. Hurt, R. Light, E. L. Kopan, K. A. Marsh, H. L. McCallon, R. Tam, S. Van Dyk, and S. Wheelock. The Two Micron All Sky Survey (2MASS). *AJ*, 131:1163–1183, February 2006. doi: 10.1086/498708.

J. A. Smith, D. L. Tucker, S. Kent, M. W. Richmond, M. Fukugita, T. Ichikawa, S.-i. Ichikawa, A. M. Jorgensen, A. Uomoto, J. E. Gunn, M. Hamabe, M. Watanabe, A. Tolea, A. Henden, J. Annis, J. R. Pier, T. A. McKay, J. Brinkmann, B. Chen, J. Holtzman, K. Shimasaku, and D. G. York. The u'g'r'i'z' Standard-Star System. *AJ*, 123:2121–2144, April 2002. doi: 10.1086/339311.

C. Stoughton, R. H. Lupton, M. Bernardi, M. R. Blanton, S. Burles, F. J. Castander, A. J. Connolly, D. J. Eisenstein, J. A. Frieman, Hennessy, and 182 coauthors. Sloan Digital Sky Survey: Early Data Release. *AJ*, 123:485–548, January 2002. doi: 10.1086/324741.

D. Thomas, C. Maraston, and R. Bender. Stellar population models of Lick indices with variable element abundance ratios. *MNRAS*, 339:897–911, March 2003. doi: 10.1046/j.1365-8711.2003.06248.x.

L. van Zee, E. J. Barton, and E. D. Skillman. Stellar Populations of Dwarf Elliptical Galaxies: UBVRI Photometry of Dwarf Elliptical Galaxies in the Virgo Cluster. *AJ*, 128:2797–2814, December 2004. doi: 10.1086/425530.

Websource1. `http://ircamera.as.arizona.edu`.

Websource2. `http://cass.ucsd.edu/public/tutorial/Galaxies.html`.

L.A. Wells. *Photometry using IRAF*. 1994.

S. D. M. White and C. S. Frenk. Galaxy formation through hierarchical clustering. *ApJ*, 379:52–79, September 1991. doi: 10.1086/170483.

S. D. M. White and M. J. Rees. Core condensation in heavy halos - A two-stage theory for galaxy formation and clustering. *MNRAS*, 183:341–358, May 1978.

S. K. Yi. Uncertainties of Synthetic Integrated Colors as Age Indicators. *ApJ*, 582: 202–214, January 2003. doi: 10.1086/344640.

D. G. York, J. Adelman, J. E. Anderson, Jr., S. F. Anderson, J. Annis, N. A. Bahcall, J. A. Bakken, R. Barkhouser, S. Bastian, E. Berman, W. N. Boroski, S. Bracker, C. Briegel, J. W. Briggs, J. Brinkmann, R. Brunner, S. Burles, L. Carey, M. A. Carr, F. J. Castander, B. Chen, P. L. Colestock, A. J. Connolly, J. H. Crocker, I. Csabai, P. C. Czarapata, J. E. Davis, M. Doi, T. Dombeck, D. Eisenstein, N. Ellman, B. R. Elms, M. L. Evans, X. Fan, G. R. Federwitz, L. Fiscelli, S. Friedman, J. A. Frieman, M. Fukugita, and more authors. The Sloan Digital Sky Survey: Technical Summary. *AJ*, 120:1579–1587, September 2000. doi: 10.1086/301513.